Characterizing Cosmic Neutrino Sources

A Measurement of the Energy Spectrum and Flavor Composition of the Cosmic Neutrino Flux Observed with the IceCube Neutrino Observatory

DISSERTATION

zur Erlangung des akademischen Grades
doctor rerum naturalium
(Dr. rer. nat.)
im Fach Physik

eingereicht an der
Mathematisch-Naturwissenschaftlichen Fakultät
der Humboldt-Universität zu Berlin

von

Lars Bastian Mohrmann

Präsident der Humboldt-Universität zu Berlin:
Prof. Dr. Jan-Hendrik Olbertz

Dekan der Mathematisch-Naturwissenschaftlichen Fakultät:
Prof. Dr. Elmar Kulke

Gutachter:
1. Prof. Dr. Marek Kowalski
2. Prof. Dr. Klas Hultqvist
3. Priv.-Doz. Dr. Alexander Kappes

Tag der mündlichen Prüfung: 11.11.2015

Abstract

The IceCube Neutrino Observatory is a km^3-sized neutrino telescope located at the geographical South Pole. The telescope consists of an array of more than 5,000 photosensors, embedded deep in the glacial ice, that record the Cherenkov radiation emitted by secondary particles created in neutrino interactions. Its primary purpose is the detection of high-energy cosmic neutrinos. Such neutrinos are expected to be produced in interactions of high-energy cosmic rays with ambient matter or photons close to their acceleration sites. With their unique properties, neutrinos may help to identify these sites, and probe the acceleration process.

In 2013, the IceCube Collaboration has reported the first evidence for a flux of high-energy cosmic neutrinos. While the origin of the flux remains unknown so far, the properties of its sources can be constrained by measuring its energy spectrum and its composition of electron, muon, and tau neutrinos (designated as "flavor composition"). The present work constitutes the first comprehensive analysis of IceCube data with respect to these principal characteristics of the flux.

Several data sets that were originally collected for separate studies were assembled and simultaneously studied in a combined analysis. Experimentally observed distributions of reconstructed energy, zenith angle and particle signature were fitted with model distributions for the background of atmospheric muons and neutrinos and for the cosmic neutrino flux. The combination of models that describes the data best was determined with a maximum-likelihood estimator.

Assuming the cosmic neutrino flux to be isotropic and to consist of equal flavors at Earth, the all-flavor spectrum is well described by a power law with normalization $(6.7^{+1.1}_{-1.2}) \times 10^{-18}\,\mathrm{GeV}^{-1}\,\mathrm{s}^{-1}\,\mathrm{sr}^{-1}\,\mathrm{cm}^{-2}$ at $100\,\mathrm{TeV}$ and spectral index -2.50 ± 0.09 for neutrino energies between $25\,\mathrm{TeV}$ and $2.8\,\mathrm{PeV}$. A spectral index of -2, an often-quoted benchmark value, is disfavored with a significance of 3.8 standard deviations.

The flavor composition is compatible with that expected for standard neutrino production processes at the sources. However, a scenario in which only electron neutrinos are produced, *e.g.* in the decay of high-energy neutrons, is disfavored with a significance of 3.6 standard deviations. Assuming that standard neutrino oscillations transform the neutrino flavors during propagation from the sources to the Earth, the measured fraction of electron neutrinos at Earth is $(18 \pm 11)\%$.

These results constitute the most precise characterization of the cosmic neutrino flux observed with the IceCube Neutrino Observatory obtained so far.

Keywords:
Astroparticle physics, Neutrino, IceCube, Spectrum, Flavor

Zusammenfassung

Das IceCube Neutrino Observatorium ist ein km^3-großes Neutrinoteleskop und befindet sich am geographischen Südpol. Das Teleskop besteht aus mehr als 5.000 Photosensoren, die tief in das Gletschereis eingelassen sind und Cherenkov-Strahlung messen, welche von in Neutrinowechselwirkungen erzeugten Sekundärteilchen abgestrahlt wird. Das Hauptziel des Experiments ist es, hochenergetische kosmische Neutrinos nachzuweisen. Es wird erwartet, dass solche Neutrinos in Wechselwirkungen von hochenergetischer kosmischer Strahlung mit Materie oder Photonen in der Nähe ihrer Beschleunigungsumgebung entstehen. Durch ihre einzigartigen Eigenschaften können Neutrinos dazu beitragen, diese Umgebungen zu identifizieren und den Beschleunigungsprozess zu untersuchen.

Der erste Nachweis für einen Fluss von hochenergetischen kosmischen Neutrinos wurde 2013 von der IceCube-Kollaboration erbracht. Der Ursprung des Flusses ist noch nicht bekannt, dennoch können die Eigenschaften der Quellen durch eine Messung des Energiespektrums und der Zusammensetzung aus Elektron-, Muon-, und Tau-Neutrinos (der "Flavor-Zusammensetzung") des Flusses eingeschränkt werden. Die vorliegende Arbeit stellt die erste umfassende Analyse von Daten des IceCube-Experiments im Hinblick auf diese wesentlichen Eigenschaften des Flusses dar.

Mehrere Datensätze, welche ursprünglich für separate Studien ausgewählt wurden, wurden kombiniert und gemeinsam analysiert. Dabei wurden experimentell beobachtete Verteilungen von rekonstruierter Energie, Zenithwinkel und Teilchen-Signatur mit Modellverteilungen für den Untergrund von atmosphärischen Muonen und Neutrinos und für den kosmischen Neutrinofluss angepasst. Die Kombination aus Modellen, welche die Daten am besten beschreibt, wurde mit einem Maximum-Likelihood-Schätzer bestimmt.

Unter der Annahme, dass der Fluss isotrop ist und zu gleichen Teilen aus allen Neutrino-Flavors besteht, wird das Spektrum durch ein Potenzgesetz mit Normalisierung $(6.7^{+1.1}_{-1.2}) \times 10^{-18}\,\mathrm{GeV}^{-1}\,\mathrm{s}^{-1}\,\mathrm{sr}^{-1}\,\mathrm{cm}^{-2}$ bei 100 TeV und spektralem Index -2.50 ± 0.09 zwischen Neutrino-Energien von 25 TeV und 2.8 PeV gut beschrieben. Ein spektraler Index von -2, welcher einen vielzitierten Modellwert darstellt, kann mit einer Signifikanz von 3.8 Standardabweichungen ausgeschlossen werden.

Die Flavor-Zusammensetzung ist kompatibel mit Erwartungen für Standard-Prozesse der Neutrino-Produktion an den Quellen. Die ausschließliche Produktion von Elektron-Neutrinos, z.B. durch den Zerfall hochenergetischer Neutronen, kann hingegen mit einer Signifikanz von 3.6 Standardabweichungen ausgeschlossen werden. Unter der Annahme, dass die Neutrino-Flavor während der Propagation von den Quellen zur Erde durch Standard-Neutrino-Oszillationen transformiert werden, beträgt der gemessene Anteil an Elektron-Neutrinos an der Erde $(18 \pm 11)\%$.

Diese Ergebnisse stellen die bisher präziseste Charakterisierung des kosmischen Neutrinoflusses am IceCube Neutrino Observatorium dar.

Schlagwörter:
Astroteilchenphysik, Neutrino, IceCube, Spektrum, Flavor

Meinen Eltern, Sophia und Ralf.
Und für Pauline, die immer für mich da ist.

Contents

1 Introduction 1

2 The Neutrino as a Messenger Particle 5

2.1 Fundamental Properties of Neutrinos 8
  2.1.1 Neutrino Production Processes 10
  2.1.2 Neutrino Interactions at High Energies 11
  2.1.3 Neutrino Oscillations 13
2.2 Established Neutrino Sources 16
  2.2.1 Artificially Produced Neutrinos 16
  2.2.2 Neutrinos from the Supernova Explosion SN 1987a 18
  2.2.3 Solar Neutrinos 20
  2.2.4 Atmospheric Neutrinos 22
2.3 Predicted Neutrino Sources 23
  2.3.1 The Cosmic Neutrino Background 24
  2.3.2 The Diffuse Supernova Neutrino Background . . 24
  2.3.3 Neutrinos from Dark Matter Annihilation or Decay 24

3 Neutrinos from the Acceleration Sites of Cosmic Rays 27

3.1 General Considerations 29
  3.1.1 Production Mechanisms 29
  3.1.2 Energy Spectrum 31
  3.1.3 Flavor Composition 36
  3.1.4 Connection to Ultra-High-Energy Cosmic Rays . 39
  3.1.5 Connection to High-Energy Gamma Rays 41
3.2 Candidate Source Classes 41
  3.2.1 The Hillas Plot 42
  3.2.2 Sources of TeV Gamma Rays 44
  3.2.3 Galactic Source Candidates 44
  3.2.4 Extragalactic Source Candidates 47
  3.2.5 Flux Predictions 50

4 The IceCube Neutrino Observatory 53

4.1 A Neutrino Telescope at the South Pole 54

4.2 Detection Principle . . . 56
4.2.1 Neutrino Interactions in Ice . . . 57
4.2.2 Cherenkov Radiation . . . 58
4.3 Detector Components . . . 60
4.3.1 The Digital Optical Module . . . 62
4.3.2 The Deep Antarctic Ice . . . 63
4.3.3 Data Acquisition and Online Filtering . . . 64
4.4 Detector Simulation . . . 65
4.5 Event Signatures . . . 67
4.6 Event Reconstruction . . . 67
4.6.1 Track Reconstruction . . . 69
4.6.2 Shower Reconstruction . . . 72
4.6.3 Relation to Neutrino Properties . . . 72

5 Atmospheric Backgrounds in Neutrino Telescopes 75
5.1 Atmospheric Muons . . . 77
5.1.1 Flux Characteristics . . . 77
5.1.2 Estimating the Background with Simulations . . . 79
5.2 Atmospheric Neutrinos . . . 80
5.2.1 Flux Characteristics . . . 80
5.2.2 Modeling of the Background . . . 83
5.3 Rejection Techniques . . . 85
5.3.1 Selecting Upgoing Track Events . . . 85
5.3.2 Selecting Shower Events . . . 86
5.3.3 Vetoing Atmospheric Muons . . . 87
5.3.4 The Atmospheric Neutrino Self-Veto . . . 88

6 Searches for Cosmic Neutrinos with IceCube 91
6.1 Searches for a Diffuse Flux of Neutrinos . . . 93
6.1.1 Searches for Shower Events . . . 93
6.1.2 Searches for Track Events . . . 95
6.1.3 Hybrid Event Searches . . . 98
6.1.4 Effective Areas and Observable Distributions . . . 98
6.2 Compilation of a Combined Event Sample . . . 100

7 A Likelihood Analysis on Multiple Event Samples 109
7.1 Modeling . . . 110
7.1.1 Background Components . . . 111

7.1.2 Cosmic Neutrino Component 111
7.2 Likelihood Method 114
7.2.1 Test Statistic 114
7.2.2 Pseudo Experiments 115
7.2.3 Likelihood Ratio Tests 115
7.2.4 Construction of a Credible Energy Interval . . . 117
7.3 Systematic Uncertainties 117
7.3.1 Energy Calibration Scale 118
7.3.2 Spectral Index of the Primary Cosmic-Ray Flux 121
7.3.3 Normalization of the Muon Background 122
7.3.4 Atmospheric Pion-to-Kaon Ratio 122
7.4 Data Challenges 122
7.4.1 Energy Spectrum 123
7.4.2 Flavor Composition 124
7.4.3 *P*-Values 127

8 Results 131
8.1 Results on the Energy Spectrum 132
8.1.1 Power Law Model 132
8.1.2 Other Spectral Models 142
8.1.3 North-South Model 143
8.2 Results on the Flavor Composition 145
8.2.1 2-Flavor Model 145
8.2.2 3-Flavor Model 145

9 Discussion and Outlook 149
9.1 Comparison to Previous Measurements 150
9.1.1 Energy Spectrum 150
9.1.2 Flavor Composition 151
9.2 Implications of the Measurement Results 153
9.3 Outlook 154

10 Conclusion 159

A Time Consumption of Muon Background Simulation 164

B Extension of Event Sample S2 170

C Binning of Observables 172

D Comparison of Results with Restored Event Samples 174

Bibliography 177

List of Figures 209

List of Tables 213

Acknowledgements / Danksagung 215

Selbstständigkeitserklärung 217

Chapter 1

Introduction

> *"I have done a terrible thing,*
> *I have postulated a particle that cannot be detected."*
>
> — Wolfgang Pauli [1]

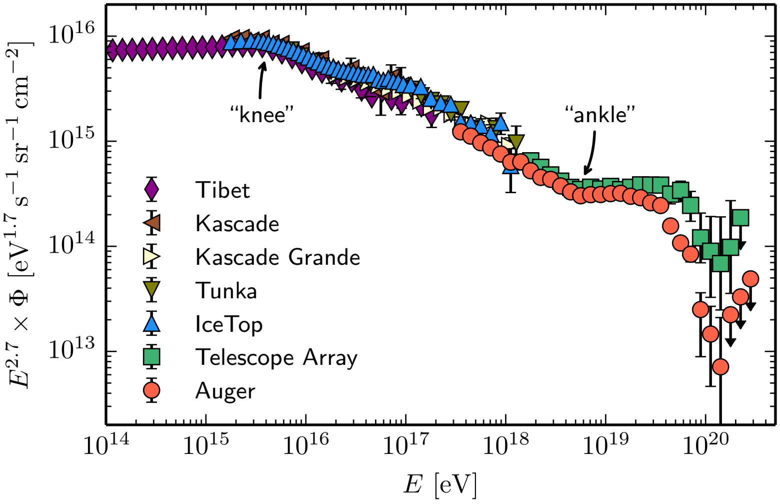

Figure 1.1 — *The Energy Spectrum of Cosmic Rays.* Shown are measurements of the all-particle cosmic-ray energy spectrum by the Tibet-III Air-Shower Array [2], the KASCADE experiment [3], the KASCADE-Grande experiment [4], the Tunka-133 EAS Cherenkov light array [5], IceTop [6], the Telescope Array [7] and the Pierre Auger Observatory [8]. Note that the vertical axis is scaled with $E^{2.7}$, to enhance the visibility of spectral features.

Eventually, Wolfgang Pauli was proven wrong. The neutrino, whose existence Pauli had postulated in a letter in 1930 [1], but of which he famously stated that it could not be detected, was in fact discovered in an experiment conducted by Frederick Reines and Clyde Cowan in 1953 [9]. It was not long after this that Kenneth Greisen and again Frederick Reines realized the neutrino's potential as a cosmic messenger: in 1960, both published articles in which they pointed out that neutrinos can be expected to be created in extraterrestrial environments, and that they propagate unaffected by cosmic magnetic fields or interstellar matter and hence carry unique information from their point of creation directly to the Earth [10, 11]. Because of the technological challenge that neutrino detection presents, however, neutrino astronomy remained wishful thinking for many decades.

In the meantime, great progress in understanding the high-energy Universe has been made through the observation of high-energy photons and high-energy charged particles. Both reaching us from the depths of the cosmos, these are commonly referred to as gamma rays and cosmic rays, respectively. As an example, the energy spectrum of cosmic rays (predominantly ionized nuclei) as measured by present-day experiments is displayed in fig. 1.1. While the exact transition point is still a matter of debate, it is generally acknowledged that cosmic rays with energies up to the "knee" are accelerated within the Milky Way, whereas cosmic rays with energies above the "ankle" are thought to be of extragalactic origin. This leads to the conclusion that both within and outside of our galaxy, cosmic rays are accelerated to remarkably high energies, certainly beyond the reach of any man-made accelerator. And yet, the acceleration sites of these particles have not been revealed until today.

It is well possible that the unambiguous identification of cosmic-ray acceleration sites is only achievable through the detection of high-energy neutrinos. These are inevitably produced when cosmic rays interact with ambient gas or photon fields, both of which are expected to be present at the acceleration sites. Unlike the cosmic rays, neutrinos are not magnetically deflected on their way to the Earth, and unlike gamma rays, they are not produced in processes that do not involve high-energy nuclei, such as inverse Compton scattering. These properties make the neutrino an ideal cosmic messenger. The expected flux of cosmic neutrinos is small however, together with the low interaction cross section of the neutrino this implies that very large detection volumes are needed to be able to record it.

Moisei Markov was the first to realize that natural detection media could be employed to accomplish this task. In 1960, he proposed "to install detectors deep in a lake or a sea and to determine the direction of charged particles with the help of Cherenkov radiation" [12] (as cited in [13]). The "charged particles" are created when neutrinos interact with nuclei in the water, and their directions are strongly correlated with those of the primary neutrinos. Several such "neutrino telescopes" have been conceived, some – like the DUMAND project off the coast of Hawaii [14] – were never put into effect, others – like the Baikal neutrino experiment in the lake Baikal in Siberia [15] or the ANTARES detector in the Mediterranean [16] – successfully take data to this day.

A new idea was published by Francis Halzen and John Learned in 1988: instead of deploying the detector under water, they proposed to utilize transparent, deep polar ice as a detection medium [17]. In 2000, a first detector of this concept, similar in size to the Baikal experiment and ANTARES, was finished near the Amundsen-Scott station at the geographical South Pole: AMANDA [18]. While all three detectors – the Baikal experiment, ANTARES and AMANDA – were successful in measuring atmospheric neutrinos, which constitute the most important background to searches for cosmic neutrinos, none of them was large enough to be able to detect a flux of cosmic neutrinos. However, they paved the way for larger successor experiments, one of which – the IceCube Neutrino Observatory – has already been put into operation.

The IceCube Neutrino Observatory is the successor experiment of AMANDA and has been installed at the same location over a period of 6 years from 2004 to 2010. With more than 5,000 optical sensors within a volume of roughly $1\,\mathrm{km}^3$ of deep Antarctic ice, it is by far the largest neutrino telescope that has ever been taken into operation, bringing the detection of cosmic neutrinos within reach for the first time. Indeed, only three years after the completion of the IceCube detector, and more than 50 years after the first proposals by Greisen, Reines and Markov, the IceCube Collaboration announced that it has found evidence for extraterrestrial neutrinos in 2013 [19]. The cosmic flux manifests itself as a deviation from the energy spectrum and zenith angle distribution expected of atmospheric neutrinos in the TeV–PeV energy range (1 TeV = 10^{12} eV; 1 PeV = 10^{15} eV), and has in this way been confirmed in several follow-up searches [20–22]. In retrospect, it becomes evident that indications for this flux had already been visible in earlier searches on data taken during the construction phase of IceCube [23–25]. The sources of the flux were searched for, but have escaped identification so far [20, 26–30]. This suggests that there are numerous sources, none of which is currently strong enough to be detected above the background of atmospheric neutrinos by itself. Nevertheless, it is possible to constrain the properties of these sources by analyzing the energy spectrum and the flavor composition of the neutrino flux they produce [31–35]. This is attempted in the present thesis.

To this effect, the energy spectrum and flavor composition of the cosmic neutrino flux in the TeV–PeV energy range are determined with a maximum-likelihood analysis in this work. Templates for background and signal components, obtained through simulation, are fitted to the distributions of reconstructed energy, zenith angle, and particle signature recorded with the IceCube detector. Similar measurements have already been done [20–22, 36], but were based on data sets much smaller than the one used here. The event samples used in this thesis were originally selected for individual studies [20–25] and were compiled by the author for the purpose of this measurement. The work thus constitutes the first comprehensive analysis of IceCube data with regard to the energy spectrum and flavor composition of the cosmic neutrino flux.

The thesis is organized as follows: In chapter 2, the neutrino as a messenger particle is introduced. General properties and possible sources of a cosmic neutrino flux are discussed in chapter 3, while chapter 4 gives an introduction to the IceCube Neutrino Observatory. Chapter 5 outlines the atmospheric backgrounds that are specific to searches for cosmic neutrinos with IceCube. An overview of the different searches that have previously been performed is given in chapter 6, along with a characterization of the event samples that are used in this work. The likelihood framework that is used to simultaneously analyze these samples is introduced in chapter 7, the results of the analysis are presented in chapter 8. Chapter 9 gives an interpretation of the results, as well as an outlook to results that can be expected to be obtained in the foreseeable future. Finally, chapter 10 concludes the thesis.

Chapter 2

The Neutrino as a Messenger Particle

> *"[...], which means that they propagate essentially unchanged in direction and energy from their point of origin [...] and so carry information which may be unique in character."*
>
> — Frederick Reines (1960) [11]

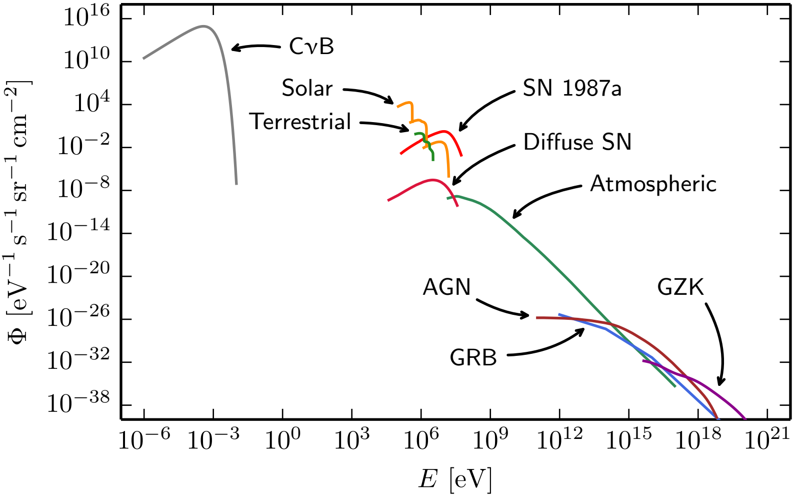

Figure 2.1 — *Neutrinos from Natural Sources.* Shown are predicted spectra of the cosmic neutrino background (CνB) [37], solar neutrinos [38], terrestrial neutrinos [39], the supernova 1987a and the diffuse supernova neutrino background [40], atmospheric neutrinos [41], neutrinos from active galactic nuclei (AGN) [42–44] and from gamma ray bursts (GRB) [45], and cosmogenic neutrinos (GZK) [46].

The first important characteristic of the neutrino as a messenger particle is its extremely feeble interaction with other particles. Because it does not carry electric charge, it is not subject to the electromagnetic force. The neutrino can interact with matter via the weak force, but does so only with very low cross sections. This means that it can escape all but the densest environments, including, for example, the interior of the Sun. It also implies that neutrinos can reach the Earth from the farthest edges of the Universe, even if they carry a large energy. This distinguishes them from photons, which, with increasing energy, are more and more likely to get absorbed in electron pair-production interactions with ambient radiation fields, such as the cosmic microwave background. This "gamma-ray horizon", from beyond which photons are unlikely to reach the Earth, is depicted in fig. 2.2. Furthermore, the neutrino shares the photon's property not to be affected by magnetic fields, thus traversing the cosmos without changing its direction. This is not the case for charged cosmic rays, which are deflected from their trajectories by the ever-present magnetic fields within and between galaxies.

The second feature that makes the neutrino an excellent messenger particle is its permanent emergence in a manifold of environments. Figure 2.1 shows the energy spectra of a selection of naturally occurring neutrino species, ranging from the cosmological neutrino background at milli-electronvolts to the so-called cosmogenic neutrinos at more than 10^{18} eV. Some of these neutrino species have successfully been observed, such as solar, terrestrial, and atmospheric neutrinos. In addition, measurements with neutrinos that were artificially produced in reactors and accelerators have been performed. All of these measurements have yielded rich knowledge both about the sources of the neutrinos as well as the properties of the neutrinos themselves, showing the rich potential of the neutrino as a messenger particle. Section 2.1 introduces the fundamental properties of the neutrino that we know today, focusing on those that are relevant for this work. Section 2.2 then gives a summary of the most important established neutrino sources and outlines the implications of essential measurements of neutrinos from these sources.

Other neutrino species have not been measured yet, but are theoretically well established; these are briefly outlined in section 2.3. Of particular relevance for this thesis is the conjecture that, just like in

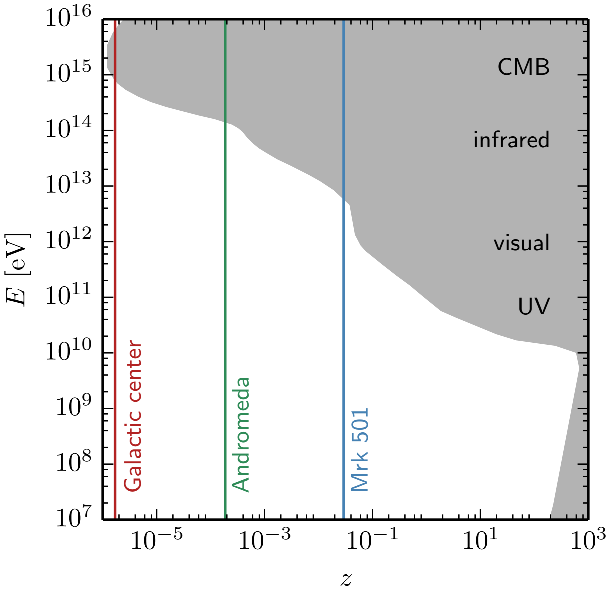

Figure 2.2 — *The Gamma-Ray Horizon.* The horizon is marked by the boundary of the gray area, as a function of the distance to the Earth, measured in cosmological redshift z. Gamma-ray photons of a particular energy E from beyond this horizon are likely to be absorbed by the radiation fields denoted by the labels in black font (CMB: cosmic microwave background; UV: ultra-violet radiation). Also indicated are the distances to the center of our Galaxy, the Andromeda galaxy, and the active galaxy Markarian 501. There is no corresponding horizon for neutrinos of the same energies. Reproduced from [47].

the Earth's atmosphere, cosmic rays create neutrinos nearby their acceleration sites, *i.e.* that the sources of high-energy cosmic rays are also sources of high-energy neutrinos. Detecting a flux of neutrinos from these as yet unidentified sources, and thus to learn about their nature, is the primary target of neutrino telescopes like the IceCube Neutrino Observatory. Theoretical expectations and candidate sources for such a cosmic neutrino flux are presented in more detail in chapter 3.

2.1 Fundamental Properties of Neutrinos

The neutrino was hypothesized in 1930 by Wolfgang Pauli as a means to rescue the law of energy conservation, which appeared to be violated in measurements of β-decay spectra in the late 1920's. The first theoretical framework that contained the neutrino and its interactions was then formulated in Enrico Fermi's famous paper "Versuch einer Theorie der β-Strahlen" in 1934 [48], only four years after Pauli's postulate, and long before it was first detected. Later, the neutrino became an integral component of the theory of the so-called Fermi (or weak) interaction, proposed by Sudarshan and Marshak [49] and Feynman and Gell-Mann [50] in 1958. Today, neutrinos and their interactions are described within the Standard Model of particle physics (for a general review, see [51]).

In the Standard Model, there are three generations of neutrinos: the electron neutrino (ν_e), the muon neutrino (ν_μ), and the tau neutrino (ν_τ), as well as their antiparticles ($\bar{\nu}_e, \bar{\nu}_\mu, \bar{\nu}_\tau$). The distinction between neutrinos and antineutrinos is unimportant for most of this work, the expression *neutrino* stands for both unless explicitly noted. Neutrinos are electrically neutral and subject only to weak interactions. Via the exchange of heavy gauge bosons ($W^\pm$ and Z^0), they can interact with the other fermions of the Standard Model, *i.e.* the charged leptons (the electron, muon, and tau) and the quarks. The basic Feynman diagrams for these interactions are shown in fig. 2.3. According to the electric charge of the mediator, the interactions are called charged-current ($W^\pm$) and neutral-current (Z^0) interactions. In charged-current interactions, due to charge conservation, neutrinos are transformed into the corresponding charged leptons: electron neutrinos into electrons, muon neutrinos into muons, and tau neutrinos into tau leptons. In contrast, no particle transformation takes place in neutral-current interactions.

While neutrinos are massless in the original formulation of the Standard Model, the observation of neutrino oscillations (for a summary see section 2.1.3) suggests that neutrinos do have mass. Experiments aiming at measuring the neutrino mass have been carried out, but have only provided upper limits so far. The currently most stringent, although model-dependent upper limits are obtained indirectly by cosmological and astrophysical measurements; these constrain the

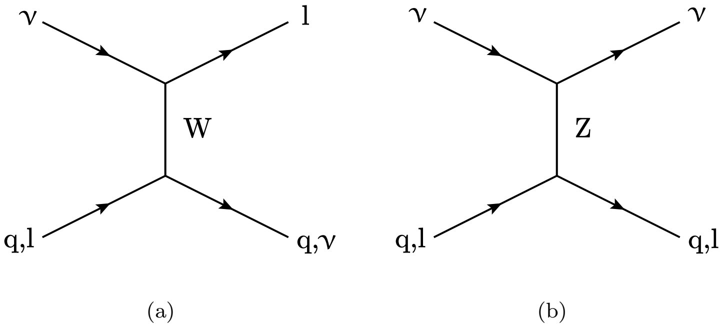

Figure 2.3 — *Feynman Diagrams for Neutrino Interactions.* (a) charged-current interaction; (b) neutral-current interaction. q denotes quarks, l charged leptons. Note that in charged-current interactions, initial and final state particles are not identical.

sum of all neutrino masses to be smaller than $0.2 - 1.3\,\mathrm{eV}$, depending on the measurement technique [52]. More directly, measurements of the endpoint of the β-decay spectrum have provided upper limits of $\sim 2\,\mathrm{eV}$ on the average electron neutrino mass [53]. Employing the same technique, the KATRIN experiment, currently under construction, is designed to be sensitive down to $0.2\,\mathrm{eV}$ [53].

Given these restrictive upper limits, neutrinos can be treated as massless for all practical purposes other than neutrino oscillations in excellent approximation. In this case, the neutrino's *helicity*

$$h = \frac{\vec{s} \cdot \vec{p}}{|\vec{p}|}\,, \tag{2.1}$$

i.e. the projection of its spin $\vec{s}$ onto its momentum $\vec{p}$, is a conserved quantity. Furthermore, the helicity coincides with the *chirality*, or *handedness*, of the neutrino, which governs its interaction with other particles. Experimentally, only neutrinos with helicity $h = -1$ and antineutrinos with helicity $h = 1$ have been observed so far; this was first found by Goldhaber *et al.* [54] and Palathingal [55], respectively. Therefore, in the Standard Model, neutrinos interact always as left-handed particles and antineutrinos always as right-handed particles.

2.1.1 Neutrino Production Processes

Neutrinos are produced in a variety of processes, very often in the decay of other particles. For instance, the muon and tau are both unstable and their decay products always include neutrinos. The muon virtually always decays into an electron, an electron antineutrino and a muon neutrino (or their antiparticles):

$$\begin{aligned} \mu^- &\rightarrow e^- + \bar{\nu}_e + \nu_\mu \, ; \\ \mu^+ &\rightarrow e^+ + \nu_e + \bar{\nu}_\mu \, . \end{aligned} \tag{2.2}$$

The tau has many decay modes, all containing at least one tau neutrino in the final state. Furthermore, electron and muon neutrinos are produced in the main decay modes, either directly or indirectly through the decay of secondary pions (see eq. 2.4) [51].

Neutrinos are also often produced in the weak decay of hadronic particles, *i.e.* particles consisting of quarks. The classic example is the beta decay of the neutron,

$$n \rightarrow p + e^- + \bar{\nu}_e \, , \tag{2.3}$$

in which electron antineutrinos are produced. Heavier atomic nuclei can also undergo beta decay, always leading to the production of electron antineutrinos. Decay modes of heavier baryons that include neutrinos often have very small branching fractions [51].

Another example of neutrino production by the decay of hadronic particles is meson decay. The lightest meson is the pion; charged pions almost exclusively decay into a muon and a muon neutrino:

$$\begin{aligned} \pi^- &\rightarrow \mu^- + \bar{\nu}_\mu \, ; \\ \pi^+ &\rightarrow \mu^+ + \nu_\mu \, . \end{aligned} \tag{2.4}$$

Heavier mesons often have multiple decay modes, many of which contain neutrinos in the final state [51].

Finally, it should be mentioned that neutrinos are also created in nuclear fusion processes, *e.g.* in the Sun. In contrast to neutrinos produced in particle decays, which are limited in energy only by the energy of the mother particle, neutrinos created in fusion processes carry energies not larger than $\sim 20\,\mathrm{MeV}$ [38], and are thus not important in the scope of this thesis.

2.1.2 Neutrino Interactions at High Energies

Of particular interest for this work is the interaction of high-energy neutrinos with nucleons. For a general overview on neutrino interactions, see *e.g.* [56].

In neutrino-nucleon interactions, neutrinos with energies $\gtrsim 10\,\mathrm{GeV}$ can resolve the constituents of the nucleon and scatter off individual quarks. This process is called deep inelastic scattering (DIS) and is by far the dominant interaction process for neutrinos in the energy range relevant to this work, $E_\nu \gtrsim 1\,\mathrm{TeV}$ [56] (with the partial exception of the Glashow resonance, see further below). Figure 2.4 shows Feynman diagrams of charged-current and neutral-current DIS processes. In both cases, the interacting nucleus is ripped apart, giving rise to a hadronic particle shower. In addition, the final state contains either a charged lepton or, in neutral-current interactions, a neutrino.

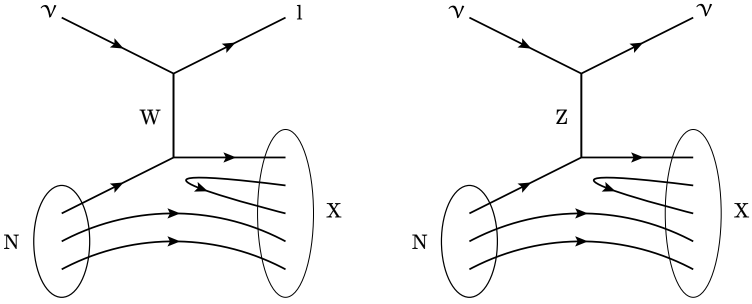

(a) (b)

Figure 2.4 — *Feynman Diagrams for Deep Inelastic Scattering.* (a) charged-current interaction; (b) neutral-current interaction. N denotes the interacting nucleon, X symbolizes a hadronic particle shower.

The cross sections for scattering of neutrinos with nucleons at high energies are shown in fig. 2.5. Up to energies of $\sim 10^{13}\,\mathrm{eV}$, the cross section grows linearly with the neutrino energy and is larger for neutrinos than for antineutrinos; the latter is a consequence of the opposite helicities of neutrinos and antineutrinos [56]. At higher energies, the energy transferred in the interaction by the intermediate boson can no longer be neglected with respect to its mass, this leads to a suppression of the cross section and disperses the difference between neutrinos and antineutrinos [56].

Figure 2.5 also shows the cross section for the scattering of electron antineutrinos with electrons. As first pointed out by Glashow, this process has a resonance when the center-of-mass energy of the system reaches the mass of the mediating boson [57]. For electrons at rest and the mass of the $W^{\pm}$ boson $m_W = 80.4\,\mathrm{GeV}$, the Glashow resonance occurs at a neutrino energy of $6.3 \times 10^{15}\,\mathrm{eV}$. As can be seen from the figure, the interaction probability for electron antineutrinos is dramatically enhanced at this energy.

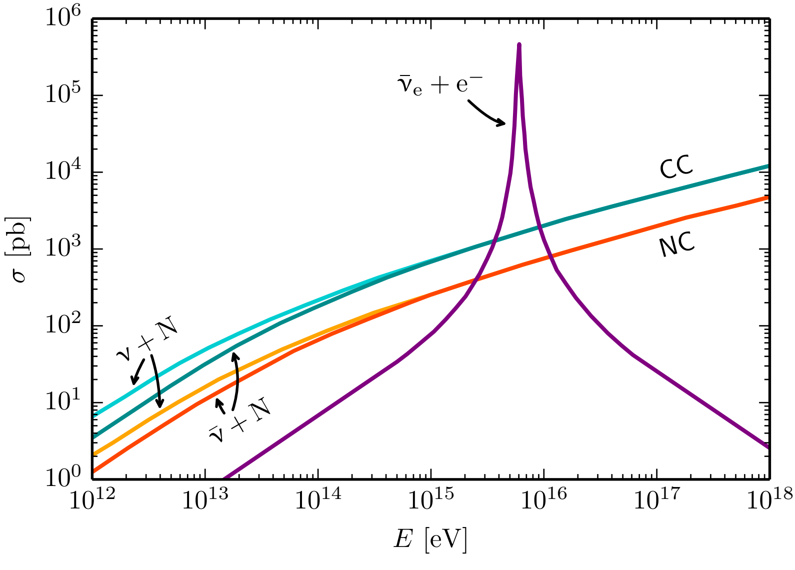

Figure 2.5 — *Neutrino Cross Sections at High Energies.* Cross section σ for charged-current (blue) and neutral-current (orange) neutrino-nucleon scattering of neutrinos with energy E. The cross section for the scattering of electron antineutrinos with electrons is shown in purple, this process is dominant around the so-called *Glashow resonance* at 6.3 PeV. Reproduced from [58].

2.1.3 Neutrino Oscillations

Neutrino oscillations refers to the phenomenon that neutrinos can change their type – or *flavor* – during propagation: there is a non-zero probability that a neutrino produced with a particular flavor is detected as another flavor. It was first pointed out by Pontecorvo that this possibility occurs if neutrinos have mass [59]. As neutrino oscillations have been observed, it is generally acknowledged today that this must be the case. The Standard Model, assuming massless neutrinos, is hence incomplete in this respect. It can however be extended to include massive neutrinos, where two general cases can be distinguished: (i) the neutrino could be a so-called Dirac fermion, acquiring mass in the same way as the other fermions, *i.e.* the charged leptons and quarks; (ii) the neutrino could be a Majorana fermion, acquiring mass by a different mechanism that is based on the conception that neutrinos and antineutrinos are identical. The latter is a possibility that exists because neutrinos are, in contrast to all other fermions, electrically neutral. For more details on the acquirement of neutrino masses, see *e.g.* [60]. In the following derivations, it is assumed that neutrinos are Dirac fermions; this choice has no impact on any conclusions drawn here.

The theory of neutrino oscillations in vacuum is briefly outlined in this section, following the review in [61]. Neutrino oscillations in matter are not relevant for the present work and are not covered here. In the following, natural units are used ($\hbar = c = 1$).

The basic conditions for neutrino oscillations to occur is that

- there are three neutrino *mass eigenstates* $|\nu_1\rangle, |\nu_2\rangle, |\nu_3\rangle$ with different masses;
- the mass eigenstates do not coincide with the *flavor eigenstates* $|\nu_\mathrm{e}\rangle, |\nu_\mu\rangle, |\nu_\tau\rangle$.

While the flavor eigenstates are defined by the neutrino production and interaction processes, the propagation of neutrinos is governed by the mass eigenstates. The flavor eigenstates and mass eigenstates are connected by the transformation

$$|\nu_\alpha\rangle = \sum_j U^*_{\alpha j} \, |\nu_j\rangle \ , \tag{2.5}$$

with $\alpha = \mathrm{e}, \mu, \tau$ and $j = 1, 2, 3$. The unitary rotation matrix U is called Pontecorvo-Maki-Nakagawa-Sakata (PMNS) matrix, named after pioneers of the theory. It is commonly parametrized as

$$U = \begin{pmatrix} c_{12}c_{13} & s_{12}c_{13} & s_{13}e^{-i\delta} \\ -s_{12}c_{23} - c_{12}s_{13}s_{23}e^{i\delta} & c_{12}c_{23} - s_{12}s_{13}s_{23}e^{i\delta} & c_{13}s_{23} \\ s_{12}s_{23} - c_{12}s_{13}c_{23}e^{i\delta} & -c_{12}s_{23} - s_{12}s_{13}c_{23}e^{i\delta} & c_{13}c_{23} \end{pmatrix}, \tag{2.6}$$

where $s_{jk} \equiv \sin\theta_{jk}$ and $c_{jk} \equiv \cos\theta_{jk}$. The matrix hence depends on four independent parameters, three mixing angles (θ_{12}, θ_{13}, and θ_{23}) and one phase parameter (δ).

The temporal evolution of the mass eigenstates is given by the Schrödinger equation, which, for particles propagating in vacuum, has the solution

$$|\nu_j(t)\rangle = e^{-iE_jt}\,|\nu_j(t=0)\rangle\ , \tag{2.7}$$

where t denotes the time and E_j the energy of the neutrino (using the so-called *plane wave approximation*, see *e.g.* [61] and references therein for more details).

The probability to detect a neutrino with initial state $|\nu_\alpha\rangle$ as state $|\nu_\beta\rangle$ is then

$$\begin{aligned} P_{\nu_\alpha\to\nu_\beta} = \left|\langle\nu_\beta|e^{-iE_jt}|\nu_\alpha\rangle\right|^2 &= \left|\sum_j U^*_{\alpha j}U_{\beta j}\ e^{-iE_jt}\right|^2 \\ &= \sum_{j,k} U^*_{\alpha j}U_{\beta j}U_{\alpha k}U^*_{\beta k}\ e^{-i(E_j-E_k)t}\,. \end{aligned} \tag{2.8}$$

Using the fact that neutrinos are ultra-relativistic for all cases considered here, we can now simplify

$$E_j \;=\; \sqrt{p_j^2 + m_j^2} \;\simeq\; p_j + \frac{m_j^2}{2p_j} \;\simeq\; E + \frac{m_j^2}{2E} \tag{2.9}$$

and $t \simeq L$, where L is the propagation distance of the neutrino. This leads to

$$-\,i(E_j - E_k)t \;\simeq\; -i\frac{\Delta m^2_{jk}L}{2E}\,, \tag{2.10}$$

with the squared mass differences $\Delta m^2_{jk} \equiv m^2_j - m^2_k$. Using this, eq. 2.8 can be written as

$$\begin{aligned} P_{\nu_\alpha \to \nu_\beta} = \delta_{\alpha\beta} &- 4 \sum_{j>k} \mathrm{Re}\left(U^*_{\alpha j} U_{\beta j} U_{\alpha k} U^*_{\beta k}\right) \sin^2\left(\frac{\Delta m^2_{jk} L}{4E}\right) \\ &+ 2 \sum_{j>k} \mathrm{Im}\left(U^*_{\alpha j} U_{\beta j} U_{\alpha k} U^*_{\beta k}\right) \sin\left(\frac{\Delta m^2_{jk} L}{2E}\right) , \end{aligned} \tag{2.11}$$

where $\delta_{\alpha\beta}$ is the Kronecker delta function. The oscillatory phase can conveniently be expressed as

$$\frac{\Delta m^2_{jk} L}{4E} \approx 1.267 \times \frac{\Delta m^2_{jk}}{\mathrm{eV}^2} \frac{L}{\mathrm{km}} \frac{\mathrm{GeV}}{E} . \tag{2.12}$$

From eq. 2.11 it may now be observed that the oscillation probability depends on the four parameters of the PMNS matrix U, the squared mass differences Δm^2_{jk}, and the ratio of the propagation distance to the neutrino energy, L/E. While the latter is determined by the experimental setup, the other parameters are fundamental and have to be determined experimentally. This has been achieved to reasonable precision for all parameters except the phase parameter δ, see table 2.1 for an overview.

A graphical illustration of the effect of neutrino oscillations may be obtained from fig. 2.6, which shows the oscillation probability (eq. 2.11) for the different neutrino flavors as a function of the L/E parameter.

If multiple neutrinos from a source are observed, coherence effects become important. Specifically, if the neutrinos are produced incoherently (*i.e.* out of phase) and travel sufficiently far, the probability to observe a particular neutrino flavor (eq. 2.11) must be averaged over L/E:

$$\langle P_{\nu_\alpha \to \nu_\beta} \rangle = \delta_{\alpha\beta} - 2 \sum_{j>k} \mathrm{Re}\left(U^*_{\alpha j} U_{\beta j} U_{\alpha k} U^*_{\beta k}\right) . \tag{2.13}$$

This probability is now independent of the squared mass differences Δm^2_{jk} as well as independent of the propagation distance L and the neutrino energy E. Hence, in an incoherently produced neutrino beam, the probability to observe a particular flavor is fully determined by the input energy spectrum and flavor composition of the neutrinos.

Table 2.1 — *Neutrino Oscillation Parameters.* Best-fit neutrino oscillation parameters as determined in [62]. Note that the sign of Δm^2_{32} is yet unknown, the table gives the best-fit values assuming so-called normal ordering ($\Delta m^2_{32} > 0$; $m_1 < m_2 < m_3$) and inverted ordering ($\Delta m^2_{32} < 0$; $m_3 < m_1 < m_2$) separately. The inverted ordering is slightly preferred in [62], although with very low significance.

Parameter / Unit	Normal ordering	Inverted ordering
$\theta_{12}\,/\,^\circ$	$33.48^{+0.78}_{-0.75}$	$33.48^{+0.78}_{-0.75}$
$\theta_{13}\,/\,^\circ$	$8.50^{+0.20}_{-0.21}$	$8.51^{+0.20}_{-0.21}$
$\theta_{23}\,/\,^\circ$	$42.3^{+3.0}_{-1.6}$	$49.5^{+1.5}_{-2.2}$
$\delta\,/\,^\circ$	306^{+39}_{-70}	254^{+63}_{-62}
$\Delta m^2_{21}\,/\,10^{-5}\,\mathrm{eV}^2$	$7.50^{+0.19}_{-0.17}$	$7.50^{+0.19}_{-0.17}$
$\Delta m^2_{32}\,/\,10^{-3}\,\mathrm{eV}^2$	$2.457^{+0.047}_{-0.047}$	$-2.449^{+0.048}_{-0.047}$

2.2 Established Neutrino Sources

This section gives a short overview of measurements of neutrinos from known sources, showing how neutrinos were employed as messenger particles in the past (and still are today). The existence of three generations of neutrinos and many of their fundamental properties have been determined in experiments with artificially produced neutrinos, see section 2.2.1. The only identified source of neutrinos from beyond the solar system is SN 1987a, a supernova explosion that took place in the Large Magellanic Cloud in 1987 (section 2.2.2). Finally, the fact that neutrinos can oscillate, *i.e.* change their flavor during propagation, was established in measurements of solar and atmospheric neutrinos, as summarized in section 2.2.3 and section 2.2.4.

2.2.1 Artificially Produced Neutrinos

The two most important classes of artificially produced neutrinos are reactor neutrinos and accelerator neutrinos, which are explained in this section. Significant numbers of neutrinos are also produced in the explosion of nuclear weapons, this is not discussed here.

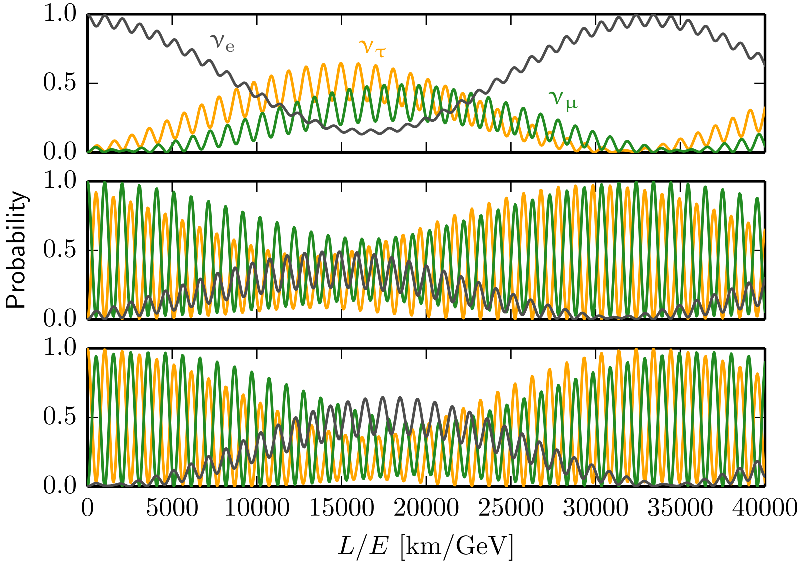

Figure 2.6 — *Neutrino Oscillation Probabilities.* Shown are the probabilities for an initial electron neutrino (top), muon neutrino (center), and tau neutrino (bottom) to be detected as an electron neutrino (gray), muon neutrino (green), or tau neutrino (yellow) as a function of the parameter L/E. Calculated with eq. 2.11, using the neutrino oscillations parameters in table 2.1 (inverted ordering).

Reactor Neutrinos

In nuclear reactors, energy is released by nuclear fission of heavy isotopes. The fission fragments undergo beta decay (see eq. 2.3), thus producing some 10^{20} electron antineutrinos per second in a typical reactor [63]. A fraction of these neutrinos can then be detected via the inverse beta decay reaction

$$\bar{\nu}_e + p \;\rightarrow\; e^+ + n\,. \tag{2.14}$$

In their pioneering experiment in 1953, Reines and Cowan used a detector filled with cadmium-loaded scintillator to identify reactions of this kind, where the coincident detection of a prompt scintillation signal from the positron and a delayed signal from neutron capture on cadmium provided a unique signature [9]. This experiment constituted the first detection of the neutrino, thus confirming Pauli's postulate.

Today, experiments with very similar techniques are still performed at different nuclear reactors around the world. Recently, these experiments have provided the first measurement of the neutrino mixing angle θ_{13} [64,65], one of the few remaining unknown parameters in the theory of neutrino oscillations.

Accelerator Neutrinos

Neutrinos can also be produced by colliding high-energy protons with a massive target. The secondary products of such collisions include charged pions, which decay into a muon and a muon neutrino (see eq. 2.4). In 1962, the muon neutrino was first detected in an experiment located at an accelerator at the Brookhaven National Laboratory [66]. The muons produced in the pion decay were stopped in a thick iron wall before they could decay; the neutrinos were detected in a spark chamber behind the wall. Unlike in the case of the electron neutrino, in which electrons are produced in the interaction, muons were found as interaction products. This lead to the important conclusion that there are more than one type of neutrinos.

Similarly, the tau neutrino was discovered in an accelerator experiment in 2000, this time originating from the decay of D_S mesons that were created in the collision of a proton beam with a tungsten target [67]. With this discovery three generations of neutrinos were established, matching the three generations of charged leptons and quarks that had been detected by this time.

Nowadays, accelerator neutrinos are being employed to perform precision measurements of neutrino oscillations. In particular, the first experiments that have measured neutrinos of a flavor different from the one produced (so-called *appearance* experiments) were recently carried out with accelerator neutrinos [68,69].

2.2.2 Neutrinos from the Supernova Explosion SN 1987a

On February 23, 1987, a burst of neutrino events was observed in three different underground neutrino detectors, located in Japan, the

United States, and the Soviet Union, within a time interval of less than a minute [70–72].[1] The sequence of the neutrino arrival times and energies is shown in fig. 2.7. Even though only 24 neutrinos were detected in total, the expected background within the detection time window was much lower, so that the detection was highly significant.

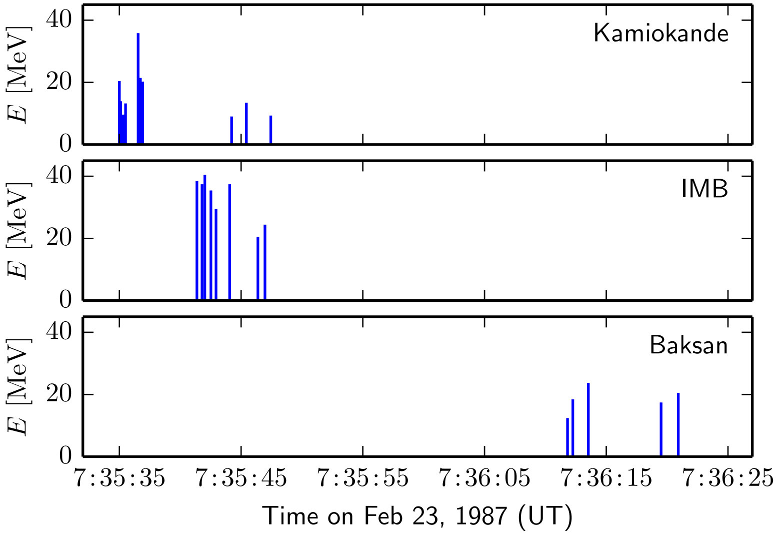

Figure 2.7 — *Neutrinos from SN 1987a.* Time sequence showing the arrival times and energies of the neutrino events detected in the Kamiokande detector in Japan [70], the IMB detector in the United States [71], and the Baksan detector in the Soviet Union [72]. Note that the times of the events in the Kamiokande detector are uncertain to ±1 minute and the times of the events in the Baksan detector have an uncertainty of $^{+2}_{-54}$ seconds [75].

One day later, on February 24, a core-collapse supernova explosion (named SN 1987a) was discovered in the Large Magellanic Cloud, a satellite galaxy of the Milky Way. Since core-collapse supernovae are expected to release about 99% of the available energy by emitting a short burst of $\sim 10^{58}$ neutrinos [76], it is very likely that the neutrinos detected on the previous day originated from the supernova explosion. This is remarkable because SN 1987a remains the only identified object outside the solar system from which neutrinos have been detected as of this writing. The observations of the neutrino burst are in accordance with basic models for core-collapse supernova explosions [74], showing that our theoretical understanding of these phenomena is solid.

---

[1] Another detector located at the French-Italian border also reported the detection of several neutrinos [73]. However, since these neutrinos were detected several hours prior to those in the other three experiments, their origin is questionable (see [74]).

2.2.3 Solar Neutrinos

In the Sun, neutrinos are a product of the nuclear fusion process. The majority of the neutrinos are produced in the pp-reaction

$$\mathrm{p} + \mathrm{p} \;\rightarrow\; \mathrm{d} + \mathrm{e}^{+} + \nu_{\mathrm{e}}\,, \tag{2.15}$$

with energies of up to 0.4 MeV. These neutrinos are produced so abundantly that ~ 60 billion pass through every square centimeter per second at Earth [38]. Fewer, yet still numerous neutrinos with energies of up to 15 MeV are created in the decay of boron-8 in the Sun,

$$^{8}\mathrm{B} \;\rightarrow\; ^{8}\mathrm{Be} + \mathrm{e}^{+} + \nu_{\mathrm{e}}\,. \tag{2.16}$$

Note that only electron neutrinos are produced in the Sun.

The first attempt to measure neutrinos from the Sun was made by Ray Davis at the end of the 1960's in an experiment located in the Homestake gold mine in South Dakota [77]. He employed a large tank filled with perchloroethylene, or C_2Cl_4, a common cleaning fluid. Upon interaction with electron neutrinos, chlorine atoms in the fluid converted into radioactive argon isotopes,

$$\nu_{\mathrm{e}} + {}^{37}\mathrm{Cl} \;\rightarrow\; {}^{37}\mathrm{Ar} + \mathrm{e}^{-}\,, \tag{2.17}$$

which were collected and counted. Because the expected count rates were very low, the experiment was conducted over a very long time until 1995. Famously, the rate of solar neutrinos measured by Davis was only about one third of that predicted by the standard solar model [78]. This discrepancy between the theoretical prediction and the measurement of solar neutrinos became known as the solar neutrino problem.

A different technique was employed by the Kamiokande experiment and its successor experiment Super-Kamiokande, which is still running today. The Super-Kamiokande detector consists of a large tank of ultra-pure water, viewed by more than 10,000 photomultiplier tubes [79]. Neutrinos of any type α can be detected via neutrino-electron scattering,

$$\nu_\alpha + \mathrm{e}^- \;\rightarrow\; \nu_\alpha + \mathrm{e}^- \tag{2.18}$$

where the sensitivity to electron neutrinos is larger because both neutral and charged-current interactions are possible. Because also the direction of the incident neutrinos can be determined, it was possible for the first time to demonstrate that the detected neutrinos were coming from the direction of the Sun. Nevertheless, the rate of solar neutrinos that was measured was only 36% of the predicted rate [80], enhancing the solar neutrino problem further.

The problem was finally solved in 2001 by the Sudbury Neutrino Observatory (SNO), an experiment installed in a mine in Sudbury, Canada. While similar in design to the Super-Kamiokande detector, instead of normal water, the target material of the SNO detector consisted of heavy water, $\mathrm{D_2O}$. In addition to the electron scattering reaction (eq. 2.18), neutrinos could be detected by charged-current and neutral-current interactions with deuterons,

$$\begin{aligned} \nu_\mathrm{e} + \mathrm{d} &\;\rightarrow\; \mathrm{e}^- + \mathrm{p} + \mathrm{p}\,; \\ \nu_\alpha + \mathrm{d} &\;\rightarrow\; \nu_\alpha + \mathrm{n} + \mathrm{p}\,, \end{aligned} \tag{2.19}$$

where α can again be any neutrino flavor. Thus, the SNO detector was able to measure the charged-current interaction rate of electron neutrinos and, independently, the combined neutral-current interaction rate of all three neutrino flavors [81]. While the SNO experiment, like the other experiments, measured a deficit of electron neutrinos compared to the predictions, the inferred flux of all neutrino flavors was compatible with the predicted electron neutrino flux [82]. This was convincing evidence that solar neutrinos oscillate, changing their flavor on the way to Earth from electron neutrinos to muon and tau neutrinos.

Thus, after many years of debate, the observation of solar neutrinos not only has shown that the common understanding of the fusion process in the Sun is correct, but also has revealed fundamental properties of the neutrino itself.

2.2.4 Atmospheric Neutrinos

The atmosphere of the Earth is constantly bombarded by cosmic rays, charged particles that can reach very high energies (*cf.* fig. 1.1). When such a cosmic ray hits an atom in the atmosphere, a cascade of secondary particles is created, called an *air shower*. These secondary particles include charged pions, which eventually produce electron and muon neutrinos in their decay (see eq. 2.2 and 2.4). These neutrinos, as well as those produced in the decay of other particles created in air showers, are referred to as atmospheric neutrinos. Because the primary cosmic rays may carry very large energies, atmospheric neutrinos can reach much higher energies than those produced artificially, in supernovas, or in the Sun [83] (*cf.* fig. 2.1).

Atmospheric neutrinos were first detected in 1965 in two experiments that were independently carried out by two different groups. Both groups used scintillation detectors deep underground, one in a gold mine in India [84], the other in a gold mine in South Africa [85]. The large material overburden suppressed the background of cosmic-ray induced muons to a very small level, so that in both experiments only a handful of neutrino events were sufficient to claim the detection of atmospheric neutrinos.

Since the spectrum of cosmic rays is well measured, the spectrum of atmospheric neutrinos can be inferred, too (see *e.g.* [83]). In 1998, the Super-Kamiokande experiment, already introduced in the previous section, measured a significant deviation from these predictions [86]. Specifically, a deficit of atmospheric muon neutrino events from certain directions was observed, while the measurement agreed with predictions in other directions. The deficit was consistent with the interpretation that the neutrinos change their flavor as a function of the propagation distance, the measurement therefore constituted the first solid evidence for neutrino oscillations (although measurements of solar neutrinos had indicated this since long before, as summarized in the previous section).

For neutrino telescopes such as the IceCube Neutrino Observatory, atmospheric neutrinos are of importance as they constitute a background to searches for cosmic neutrinos, but also because they can be used as a calibration signal. In fact, as displayed in fig. 2.8, measurements of the atmospheric neutrino flux were performed with the IceCube experiment, but also *e.g.* with the Fréjus experiment and the ANTARES neutrino telescope. Atmospheric neutrinos as a background in neutrino telescopes are discussed further in chapter 5.

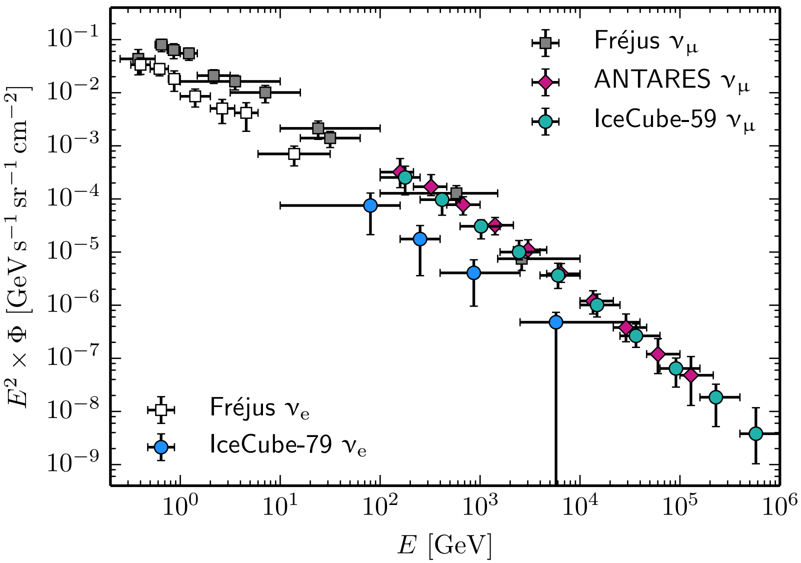

Figure 2.8 — *Measurements of the Atmospheric Neutrino Flux.* Shown are measurements of the atmospheric neutrinos flux from the Fréjus experiment [87], ANTARES [88], and IceCube [89, 90]. The vertical axis is scaled with E^2 for better readability.

2.3 Predicted Neutrino Sources

Several species of neutrino sources have been predicted but not yet (directly) detected. Some of these species are theoretically firmly established, others are more speculative. One species of particular interest for this work – neutrinos from the sources of high-energy cosmic rays – is discussed in the following chapter. This section gives a short overview over other undetected sources, where the interested reader is referred to the provided references.

2.3.1 The Cosmic Neutrino Background

Analogous to the cosmic microwave background (CMB), the Universe is also filled with relic neutrinos from the Big Bang, the cosmic neutrino background ($C\nu B$) [37]. These neutrinos have not been measured directly, however, their properties are well constrained by cosmological measurements, *e.g.* of the CMB [91]. The number density of the $C\nu B$ is expected to be $\sim 112\,\mathrm{cm}^{-3}$ and the average neutrino momentum is $\sim 5 \times 10^{-4}\,\mathrm{eV}$ [92] (*cf.* fig. 2.1). While several methods to directly detect the $C\nu B$ have been proposed (*e.g.* via the mechanical force induced by elastic scattering of relic neutrinos, via the capture of relic neutrinos on radioactive nuclei, or via absorption features in ultra-high-energy neutrino spectra), current experimental techniques still fall short several orders of magnitude of the required sensitivity (see [92] and references therein).

2.3.2 The Diffuse Supernova Neutrino Background

As already noted in section 2.2.2, supernova explosions of type II release a large fraction of their gravitational energy into a burst of $\sim 10^{58}$ neutrinos with energies of some tens of MeV [76]. Such events are observable in neutrino detectors on Earth if the explosion takes place within or close to the Milky Way galaxy, as in the case of SN 1987a. Supernova explosions of type II in other galaxies produce a cumulative flux of neutrinos that arrive isotropically at Earth, referred to as diffuse supernova neutrino background (DSNB). Based on models for core-collapse supernova, expectations for the magnitude of this flux have been derived [40]. The DSNB has not been measured experimentally yet, but it has been argued that its detection may be in reach for current-generation neutrino experiments [93].

2.3.3 Neutrinos from Dark Matter Annihilation or Decay

There is compelling indirect evidence that a large fraction of the matter in the Universe is “dark”, *i.e.* consists of particles beyond the Standard

Model of particle physics that do not participate in the electromagnetic interaction (for a review, see [94]). If these dark matter particles exist and have sufficient mass, they could annihilate or decay into known standard-model particles that would produce neutrinos in their subsequent decay chains, where the energy of the neutrinos is bounded by the dark matter particle mass. Many models predict masses in the GeV–TeV range, but models including much heavier particles have also been proposed [94].

Dark matter particles could accumulate in regions of large density, such as the Sun or the center of galaxies, leading to enhanced annihilation rates and hence to an enhanced flux of neutrinos from there [95–97]. While many other regions of high dark matter density can also be probed *e.g.* with photons, dark matter annihilation in the Sun can only be probed with neutrinos. The current best limit on the annihilation rate of dark matter particles in the Sun was obtained with the IceCube Neutrino Observatory [98].

High-energy neutrinos could also be produced in the decay of dark matter particles, if these are unstable. Such scenarios have been discussed for dark matter particles with masses up to 10 TeV [99] as well as for extremely heavy dark matter particles [100, 101].

Chapter 3

Neutrinos from the Acceleration Sites of Cosmic Rays

> *"Space is big.*
> *You just won't believe how vastly, hugely, mind-bogglingly big it is."*
>
> — Douglas Adams (1979) [102]

Figure 3.1 — *Composite Image of the Active Galaxy Centaurus A.* Submillimetre data ($\lambda = 870\,\mu\mathrm{m}$) are shown in orange, X-ray data in blue. Credit: ESO / WFI (Optical); MPIfR / ESO / APEX / A.Weiss *et al.* (Submillimetre); NASA / CXC / CfA / R.Kraft *et al.* (X-ray).

The paradigm of high-energy[1] neutrino astronomy rests upon one observational fact and two subsequent assumptions. The observational fact is that cosmic rays (*i.e.* ionized nuclei) of immensely high energies reach the Earth from the cosmos (*cf.* fig. 1.1). The two assumptions are

(i) that these cosmic rays obtain their high energies through acceleration in astrophysical environments; and

(ii) that they undergo interactions with other particles within or close to these environments.

If both assumptions hold, high-energy neutrinos are produced in conjunction with the cosmic rays and, being neutral particles, will propagate to the Earth in straight lines. In this case, their detection would offer a promising opportunity to uncover the acceleration sites of high-energy cosmic rays and to probe astrophysical acceleration processes.

Observations supportive of the first assumption include that the acceleration of charged particles has been observed at the Sun (up to energies of a few GeV, for a review see *e.g.* [103]), and that the signature of pion decay has been observed with gamma rays in two supernova remnants, which implies cosmic-ray acceleration up to TeV energies [104]. Furthermore, as already noted in 1934 by Walter Baade and Fritz Zwicky [105, 106], the observed intensity of cosmic rays can be sustained by supernova explosions in the Milky Way if these convert a few percent of their explosion energy into high-energy cosmic rays (see *e.g.* [107]).[2]

The second assumption is easily motivated when bearing in mind that the Universe is filled with gas clouds and radiation fields such as starlight or the cosmic microwave background radiation; in fact, it is hard to imagine an acceleration environment without ambient matter or photons. For these reasons, it is commonly expected that high-energy neutrinos reach us from the sources of high-energy cosmic rays (see *e.g.* [108]).

---

[1] In the context of this work, "high-energy" means energies larger than 1 TeV (10^{12} eV).

[2] Note that this argument does not apply to the highest-energy cosmic rays, which are believed to be of extragalactic origin.

Experiments like the IceCube Neutrino Observatory have been designed to detect this flux of high-energy neutrinos, and eventually to resolve its sources, the cosmic-ray acceleration sites. Before introducing the detector in the next chapter, it is instructive to review the expected general properties of a neutrino flux from cosmic sources (in section 3.1) and introduce some specific source candidates (in section 3.2).

3.1 General Considerations

3.1.1 Production Mechanisms

The vast majority of high-energy cosmic rays are either protons or heavier ionized nuclei. These particles can produce neutrinos when they interact with ambient target particles or radiation. The properties of the produced neutrino flux depend on the primary cosmic-ray flux as well as the properties of the target. There are two classes of targets generally considered, these are discussed in the following.

If the acceleration site is surrounded by interstellar gas clouds, the accelerated cosmic rays will collide with gas nuclei, producing neutral and charged pions in inelastic scattering processes. In the simplest case, both interacting nuclei are protons; hence this neutrino production mechanism is referred to as pp scenario (or, more general, *hadronuclear* scenario). While the neutral pions give rise to high-energy gamma rays,

$$\pi^0 \;\rightarrow\; \gamma + \gamma\,, \tag{3.1}$$

the charged pions produce neutrinos in their decay (*cf.* eq. 2.2 and 2.4),

$$\begin{aligned} \pi^+ \;&\rightarrow\; \mu^+ + \nu_\mu \;\rightarrow\; e^+ + \nu_e + \bar{\nu}_\mu + \nu_\mu\,; \\ \pi^- \;&\rightarrow\; \mu^- + \bar{\nu}_\mu \;\rightarrow\; e^- + \bar{\nu}_e + \nu_\mu + \bar{\nu}_\mu\,. \end{aligned} \tag{3.2}$$

The simultaneous production of gamma rays and neutrinos implies a very tight connection between these two messenger particles in the pp scenario.

The other possibility is the so-called pγ or *photohadronic* scenario. In this case, the target for the high-energy cosmic rays are photons from radiation fields that are present at the acceleration sites (*e.g.* ambient starlight or the cosmic microwave background radiation). For cosmic-ray protons, the dominating interaction process is the Δ^+ resonance,

$$\mathrm{p} + \gamma \;\rightarrow\; \Delta^+ \;\rightarrow \begin{cases} \mathrm{p} + \pi^0 \\ \mathrm{n} + \pi^+ \end{cases} , \tag{3.3}$$

where the pions subsequently decay as described above for the pp scenario. Because this is a resonant process, the energy of the cosmic rays and of the target photons have to match so that in the center-of-mass system, the Δ^+ can be produced. Additionally, pions can be produced in inelastic collisions if the center-of-mass energy exceeds the rest mass of the pion, this is called *multipion production*.

There are several peculiarities in the $\mathrm{p}\gamma$ scenario: (i) Since negatively charged pions arise only from multipion production, fewer electron antineutrinos are produced compared to the hadronuclear scenario. (ii) Fewer neutrinos are produced if the cosmic rays are predominantly heavy nuclei. The dominant interaction process in this case is photodisintegration, in which the nucleus is broken into smaller nuclei and no neutrinos are produced [109]. (iii) The connection between gamma rays and neutrinos is less tight than in the hadronuclear scenario, because the gamma rays will often interact with the photon field themselves, losing energy in the process.

In both scenarios, each neutrino carries on average $\sim 1/20$ of the initial cosmic-ray energy if the cosmic rays are protons and all secondary particles decay without interacting or losing energy [108].

One possibility to distinguish between the pp and the $\mathrm{p}\gamma$ scenario is a measurement of the flux at the Glashow resonance. As illustrated in fig. 2.5, the interaction cross section for electron antineutrinos ($\bar{\nu}_\mathrm{e}$) is greatly enhanced at the resonance around 6.3 PeV. Hence, if $\bar{\nu}_\mathrm{e}$ are present in the cosmic neutrino flux, an increased rate of events is expected at this energy. In pp sources, $\bar{\nu}_\mathrm{e}$ are directly produced in the decay of the π^-. In contrast, fewer $\bar{\nu}_\mathrm{e}$ are produced in $\mathrm{p}\gamma$ sources. While the neutrino flux arriving at Earth from such sources will also contain $\bar{\nu}_\mathrm{e}$ in the form of oscillated $\bar{\nu}_\mu$, their fraction is still lower with respect to the total flux than for pp sources. Hence, a precise measurement of the rate of cosmic neutrinos at the Glashow resonance with respect to the overall flux is sensitive to the production mechanism of the neutrinos [110].

3.1.2 Energy Spectrum

To first order, the energy spectrum of cosmic neutrinos follows the energy spectrum of the primary cosmic rays that produce them.[3] As the acceleration sites of cosmic rays are unknown, so are their acceleration mechanisms and initial energy spectrum. The energy spectrum of cosmic rays at the Earth on the other hand has been measured over many orders of magnitude in energy (see fig. 1.1). It follows a power law of $\sim E^{-2.7}$ up to $\sim 4 \times 10^{15}\,\mathrm{eV}$ (the *knee*), then steepens to $\sim E^{-3.1}$, before a spectral hardening occurs again at the *ankle* ($\sim 6 \times 10^{18}\,\mathrm{eV}$). Any model for cosmic-ray acceleration, taking into account propagation effects, must be able to explain these observations.

Fermi Acceleration

The by far most popular model for cosmic-ray acceleration is the *first order Fermi acceleration*, or *diffuse shock acceleration* mechanism. It is named after Enrico Fermi, who proposed a similar variant, now known as *second order Fermi acceleration*, in 1949 [111]. Both variants are briefly outlined in the following, with a focus on the (more efficient) first order process.

In second order Fermi acceleration, cosmic rays are accelerated by repeated elastic scattering off moving magnetic inhomogeneities, or *clouds*. The term *second order* is due to the mean relative energy gain per scattering ($\Delta E/E$) for this process, which is proportional to the second power of the average cloud velocity v divided by the speed of light,

$$\frac{\Delta E}{E} \propto \left(\frac{v}{c}\right)^2 . \tag{3.4}$$

A feature of this model is that it naturally leads to power-law spectra for the accelerated particles, matching the observation that the energy spectrum of cosmic rays at Earth follows a power law over wide energy ranges. However, because v/c is a small number in typical environments (Fermi estimated $v/c \approx 10^{-4}$), the process turns out to be rather inefficient.

---

[3] Strictly speaking, this is true only in the hadronuclear scenario. For photohadronic neutrino production, the neutrino energy spectrum also depends on the spectrum of the target radiation field.

First order Fermi acceleration describes the acceleration of particles at a shock wave propagating through a medium. As in the second order mechanism, cosmic rays gain energy stochastically in multiple scatterings. Because the particles repeatedly cross the shock front however, the average energy gain per scattering is directly proportional to the shock front velocity divided by the speed of light in this case,

$$\frac{\Delta E}{E} \propto \left(\frac{v}{c}\right) . \tag{3.5}$$

With typical shock velocities $v/c \gtrsim 10^{-2}$, this process is evidently much more efficient than the second order process. Moreover, for an idealized shock, it predicts an energy spectrum

$$\frac{\mathrm{d}N}{\mathrm{d}E} \propto E^{-2} \tag{3.6}$$

for the accelerated cosmic rays, close to the spectrum that is observed at Earth. In fact, the difference is easily explained by diffusion processes that alter the cosmic-ray energy spectrum during propagation to Earth (see *e.g.* [83]). Because of these features, and because shock fronts are not uncommon in astrophysical environments, *e.g.* in supernova remnants, the diffuse shock acceleration model is a widespread model for cosmic-ray acceleration. A short motivation of eq. 3.5 and 3.6 is given below, following the derivation in [83], to which the reader is referred for a more detailed explanation.

First, we consider a general process that increases the energy of a particle by an amount ΔE proportional to its energy E, *i.e.* $\Delta E = \xi E$. After n cycles, the particle's energy is

$$E_n = E_0 (1 + \xi)^n , \tag{3.7}$$

where E_0 is the initial energy. If the particle has a probability P_{esc} to escape the acceleration region during each cycle, the number of particles with energy greater than E is

$$N(\geq E) \propto \sum_{m=n}^{\infty} (1 - P_{\mathrm{esc}})^m = \frac{(1 - P_{\mathrm{esc}})^n}{P_{\mathrm{esc}}} . \tag{3.8}$$

Solving eq. 3.7 for n and substituting into eq. 3.8 gives

$$N(\geq E) \propto \frac{1}{P_{\mathrm{esc}}} \left(\frac{E}{E_0}\right)^{-\gamma+1} , \tag{3.9}$$

with

$$\gamma \equiv 1 - \frac{\ln(1 - P_{\text{esc}})}{\ln(1+\xi)} \approx 1 + \frac{P_{\text{esc}}}{\xi}\,. \tag{3.10}$$

The differential energy spectrum is then

$$\frac{\mathrm{d}N}{\mathrm{d}E} \propto E^{-\gamma}\,. \tag{3.11}$$

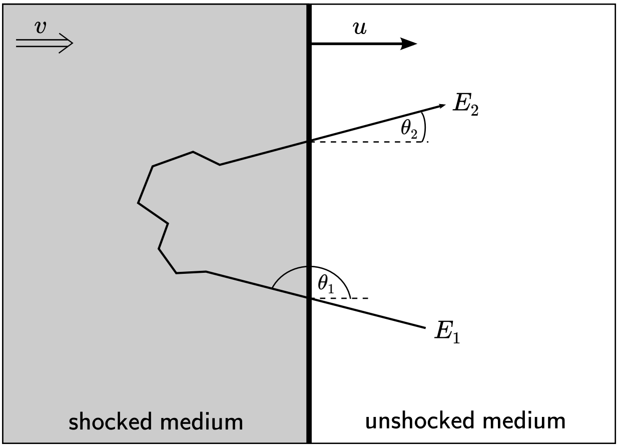

Figure 3.2 — *Fermi Shock Acceleration Sketch.* A particle with initial energy E_1 crosses a shock front back and forth, returning to the unshocked medium with final energy $E_2 > E_1$. Reproduced from [83].

Now, we consider the case of a shock front moving with velocity u through a medium (see fig. 3.2). The shocked gas follows the shock front, but with a velocity $v < u$. In this setup, one acceleration cycle is defined by the particle crossing the shock front back and forth once, as indicated in the figure. The particle's energy before and after the crossing is denoted by E_1 and E_2; its initial and final scattering angle by θ_1 and θ_2, respectively. In the reference frame of the shocked gas (denoted by primes here), the initial energy of the particle is

$$E_1' = \frac{E_1(1 - \beta\cos\theta_1)}{\sqrt{1-\beta^2}}\,, \tag{3.12}$$

where $\beta = v/c$ is the velocity of the shocked medium divided by the speed of light. Having passed through the shock front into the shocked medium, the particle's motion is randomized by multiple elastic scatterings in the magnetic field. Thus, just before crossing the shock front again back into the unshocked medium, we have $E'_1 = E'_2$. Transforming back into the laboratory frame gives

$$E_2 = \frac{E'_2(1 + \beta \cos\theta'_2)}{\sqrt{1-\beta^2}} \,. \tag{3.13}$$

Using eq. 3.12 and 3.13, we can now express the relative energy gain ξ as a function of β, θ_1, and θ_2:

$$\xi = \frac{E_2 - E_1}{E_1} = \frac{1 - \beta\cos\theta_1 + \beta\cos\theta'_2 - \beta^2\cos\theta_1\cos\theta'_2}{1-\beta^2} - 1 \,. \tag{3.14}$$

To obtain the average energy gain, we need to average over $\cos\theta_1$ and $\cos\theta'_2$. By definition (see fig. 3.2), we have $-1 \leq \cos\theta_1 \leq 0$ and $0 \leq \cos\theta'_2 \leq 1$, and thus $\langle\cos\theta_1\rangle \approx -2/3$ and $\langle\cos\theta'_2\rangle \approx 2/3$. Substituting into eq. 3.14 gives

$$\xi = \frac{1 + \frac{4}{3}\beta + \frac{4}{9}\beta^2}{1-\beta^2} - 1 \approx \frac{4}{3}\beta = \frac{4}{3}\left(\frac{v}{c}\right) , \tag{3.15}$$

which is equivalent to eq. 3.5.

Having obtained an expression for ξ, we now turn to the escape probability P_esc. It can be computed by dividing the rate of particles that escape the acceleration region (by moving away from the shock into the shocked medium) by the rate with which particles cross the shock front. For particles with a number density ρ, the former is simply $\rho(u - v)$, while the latter can be calculated as the projection of an isotropic flux onto the shock front,

$$\int_0^1 \mathrm{d}\cos\theta \int_0^{2\pi} \mathrm{d}\phi \, \frac{c\rho}{4\pi} \cos\theta = \frac{c\rho}{4} \,. \tag{3.16}$$

Thus,

$$P_\mathrm{esc} = \frac{\rho(u-v)}{c\rho/4} = \frac{4(u-v)}{c} \,. \tag{3.17}$$

Substituting eq. 3.15 and 3.17 into eq. 3.10, we obtain

$$\gamma = 1 + \frac{P_{\mathrm{esc}}}{\xi} = 1 + 3\left(\frac{u}{v} - 1\right) . \tag{3.18}$$

Remarkably, in this simple model, the spectral index of the cosmic rays depends only on the velocities of the shock front and the shocked medium. Furthermore, for fast (but non-relativistic) shocks moving with a speed larger than the speed of sound in the medium, kinetic gas theory predicts $u/v \approx 4/3$, and hence we arrive at $\gamma \approx 2$ (*cf.* eq. 3.6).

Thus, the Fermi acceleration model predicts a power-law spectrum with an index close to -2 for the cosmic rays at their sources. If the cosmic rays produce neutrinos in hadronuclear interactions and the secondary particles do not lose or gain energy before they decay, the neutrinos follow the energy spectrum of the cosmic rays. Unless in exotic scenarios, this energy spectrum of the neutrinos is not altered during their propagation to Earth. *In this benchmark scenario, it is hence expected that cosmic neutrinos arrive at Earth with an energy spectrum close to* E^{-2}. The energy spectrum of photohadronically produced neutrinos depends on the target photon field in general, but the produced neutrino flux naturally cannot exceed the primary cosmic ray flux.

Other Acceleration Models, Modifications, and Exotic Scenarios

The first order Fermi acceleration mechanism has also been considered for relativistic shocks. Analytic calculations show that a slightly steeper spectrum is expected in this case, $\sim E^{-2.3}$ [112, 113]. Furthermore, also other, non-diffusive acceleration mechanisms have been proposed. This includes plasma wake field acceleration (*e.g.* [114,115]), magnetic reconnection (*e.g.* [116–118], for a general review see [119]), and the acceleration in high-potential electric fields (*e.g.* in pulsars, see [120]). The reader is referred to the literature for a comprehensive discussion of these models.

The neutrino energy spectrum can differ from the primary cosmic-ray spectrum if the neutrino-producing secondary particles are influenced by the surrounding conditions of the source environment. For instance, prior to their decay, the pions and muons produced in cosmic-ray interactions can lose energy due to synchrotron radiation in strong magnetic fields or further interactions in very dense surroundings. This generally suppresses the neutrino flux and also modifies its energy spectrum, as discussed *e.g.* in [121–124]. Alternatively, muons produced in astrophysical environments can also gain energy before decaying through secondary acceleration, leading to an enhancement of the neutrino flux (see *e.g.* [125, 126]).

Finally, the neutrino energy spectrum could be distorted in exotic scenarios that affect the propagation of the neutrinos. One example are so-called *secret* neutrino interactions, *i.e.* interactions of high-energy cosmic neutrinos with relic neutrinos from the cosmological neutrino background, that could occur at rates much higher than expected for the weak interaction [127–129].

3.1.3 Flavor Composition

Three Benchmark Scenarios

The majority of neutrinos produced in astrophysical sources originate from the decay chain of the pion, as indicated in eq. 3.2. If the pions and muons decay without being influenced by the surrounding conditions, the neutrinos are produced with a flavor composition of $\nu_e : \nu_\mu : \nu_\tau = 1 : 2 : 0$. This is referred to as the *pion-decay* source scenario. During propagation to Earth, the flavor composition is altered by neutrino oscillations. Because the neutrinos are created at different positions within the source and carry different energies, they are typically produced incoherently, *i.e.* with a random oscillation phase. Hence, after propagation over astronomical baselines, the averaged oscillation probability in eq. 2.13 applies. Inserting the measured values of the mixing matrix, one finds that the initial composition of $1 : 2 : 0$ is transformed to approximately $1 : 1 : 1$ at Earth. *Hence, in this benchmark scenario, we expect equal numbers of cosmic electron, muon, and tau neutrinos at Earth.*

Two more benchmark scenarios can be defined, serving as boundary cases for the flavor composition. The first is the *muon-damped* source, for which the neutrinos from pion decay dominate over those from muon decay. This can be the result of energy losses of the muons, *e.g.* in strongly magnetized sources. In the limiting case, the neutrinos from muon decay are suppressed so strongly that the cosmic neutrino flux in the energy range of interest entirely consists of muon neutrinos from pion decay, *i.e.* $\nu_e : \nu_\mu : \nu_\tau = 0 : 1 : 0$.

In the second scenario, the neutrino flux is produced in the decay of neutrons rather than pions, this is the so-called *neutron-beam* source. This typically requires very extreme source environments that are magnetized even stronger than in the muon-damped scenario. As only electron neutrinos are produced in neutron decays, the flavor composition is $\nu_e : \nu_\mu : \nu_\tau = 1 : 0 : 0$ in the limiting case.

Again, these flavor compositions are altered due to neutrino oscillations. Using the oscillation parameters from table 2.1 (inverted ordering), the transformations for the three benchmark scenarios described here are

- $1 : 2 : 0 \;\rightarrow\; 0.93 : 1.05 : 1.02$ (pion-decay)
- $0 : 1 : 0 \;\rightarrow\; 0.19 : 0.43 : 0.38$ (muon-damped)
- $1 : 0 : 0 \;\rightarrow\; 0.55 : 0.19 : 0.26$ (neutron-beam).

These transformations are graphically displayed in fig. 3.3. Note that all scenarios discussed here neglect the production of tau neutrinos at the sources, which is a common assumption [35].

Modifications and Exotic Scenarios

The three benchmark scenarios introduced above represent idealized cases, the general picture is more complicated. Most important is the notion that the flavor composition of cosmic neutrinos depends on the neutrino energy [130, 131]. This is a consequence of energy-dependent energy loss processes of muons and pions, which can lead to a transition between different scenarios as a function of energy. For example, Kashti and Waxman [130] argue that pion-decay sources transform into muon-damped sources at energies around 100 TeV, so that the flavor composition at the source transitions from $1 : 2 : 0$ to $0 : 1 : 0$. More involved transition scenarios are considered in [131]. Note however that if the standard neutrino oscillation picture is valid, and for the oscillation parameter values in table 2.1, the flavor composition at Earth

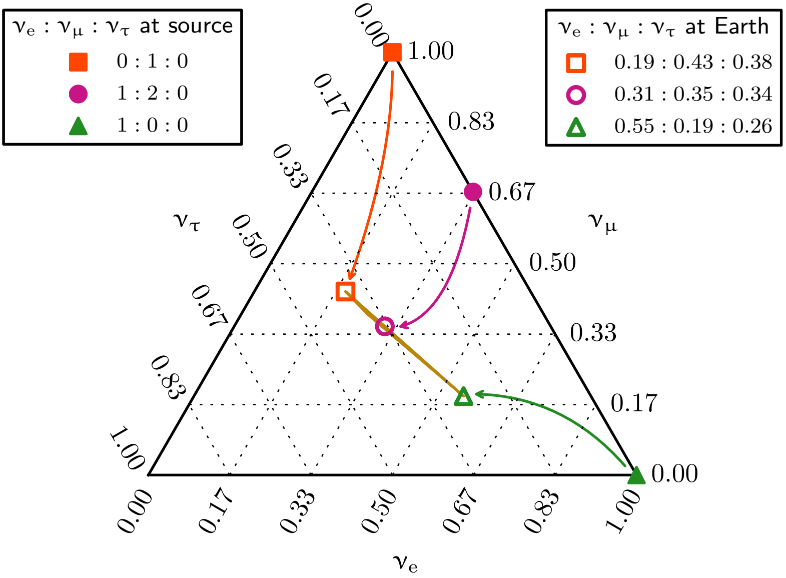

Figure 3.3 — *Flavor Composition of Cosmic Neutrinos.* Each point on the triangle corresponds to a specific ratio of $\nu_e : \nu_\mu : \nu_\tau$, where the fraction of each flavor can be read off the three axes. The expected flavor composition for pion-decay sources (circle), muon-damped sources (square), and neutron-beam sources (triangle) at the source (filled symbols) and, after oscillations, at the Earth (open symbols) is shown. The narrow filled area in the center corresponds to the parameter region to which *any* composition at the source is transformed, provided that standard neutrino oscillations hold. Calculated with the oscillation parameters from table 2.1 (inverted ordering).

is constrained to the region indicated by the narrow filled area in the center of fig. 3.3 for *any* composition at the source, at any energy.

The flavor composition can be altered beyond that in non-standard scenarios. For instance, the flavor composition could be changed considerably if some neutrino mass states are unstable and decay during propagation over very long distances [132, 133]. In another scenario, CPT and Lorentz invariance violation effects affect the flavor composition of high-energy cosmic neutrinos [134]. Conversely, the non-observation of non-standard flavor compositions can be used to derive limits on the lifetime of neutrinos or CPT/Lorentz invariance violations.

3.1.4 Connection to Ultra-High-Energy Cosmic Rays

As we are considering the production of neutrinos in sources of high-energy cosmic rays, the fluxes of these particles are naturally connected. Two important arguments regarding the connection to ultra-high-energy cosmic rays (UHECRs, $E > 10^{18}\,\mathrm{eV}$) are worth mentioning and outlined in this section.

Cosmogenic Neutrinos

The first argument concerns a flux of neutrinos not actually from within the cosmic-ray sources, but nevertheless produced by cosmic rays accelerated there. As first noted by Greisen [135] and Zatsepin and Kuzmin [136], cosmic-ray protons with energies exceeding $10^{19}\,\mathrm{eV}$ interact with the ever-present cosmic microwave background photons via photohadronic interactions (*cf.* eq. 3.3), leading to a suppression of the UHECR flux at the highest energies (the so-called *GZK cut-off*). Provided that the UHECRs are indeed protons, such interactions would lead to a flux of so-called cosmogenic neutrinos. The flux of these neutrinos was first predicted in [137]; more recent calculations can be found *e.g.* in [46]. Generally, due to the high energies of the interacting protons, cosmogenic neutrinos are expected to carry energies around $10^{18}\,\mathrm{eV}$. Although the IceCube Neutrino Observatory is sensitive to cosmogenic neutrino fluxes predicted by some models, no neutrinos of such energies have been observed so far [138]. The focus of this work are neutrinos produced within the acceleration environments of high-energy cosmic rays, with typical energies between $10^{12}\,\mathrm{eV}$ and $10^{16}\,\mathrm{eV}$, *i.e.* well below those of cosmogenic neutrinos.

The Waxman–Bahcall Upper Bound

A famous argument on the neutrino flux from the sources of ultra-high-energy cosmic rays (UHECRs) was made by Eli Waxman and John

Bahcall in 1998 [139]. Starting from the observed intensity of cosmic rays with energies greater than 10^{19} eV, they derived an upper limit on the flux of neutrinos produced within the sources of these particles, referred to as Waxman–Bahcall upper bound. The basic argument is based on several assumptions:

(i) Protons are accelerated in the sources with an energy spectrum proportional to E^{-2}.

(ii) All protons undergo photohadronic interactions (*cf.* section 3.1.1 and eq. 3.3), producing neutrons, gamma rays and neutrinos.

(iii) The sources are optically thin to neutrons, which leave the sources and subsequently decay into protons, accounting for the UHECR flux observed at the Earth.

(iv) The luminosity evolution of far-away sources, from which UHECRs cannot reach the Earth (*cf.* previous section), is not stronger than that of any other known astronomical source class.

Given these assumptions and the observed intensity of UHECRs, the Waxman–Bahcall upper bound is

$$E^2\Phi < 3 \times 10^{-8}\,\mathrm{GeV\,s^{-1}\,sr^{-1}\,cm^{-2}}\,, \tag{3.19}$$

where Φ denotes the all-flavor differential neutrino flux per unit time, area and steradian, corrected for the effects of neutrino oscillations [45, 139, 140].

The argument has been extended to cover cases in which some of the above assumptions do not hold. Waxman and Bahcall themselves argue that it is also valid for pp interactions in the sources [45]. Mannheim, Protheroe and Rachen have shown that if experimental limits on the shape of the cosmic-ray energy spectrum are considered instead of assuming an E^{-2} spectrum, the upper bound can be considerably weaker [141]. Finally, Anchordoqui *et al.* [109] and Murase and Beacom [142] have generalized the argument to include the case of UHECRs being heavier nuclei instead of protons, finding stronger constraints in some cases.

The Waxman–Bahcall upper bound has been a benchmark for neutrino telescopes for a long time. The IceCube Neutrino Observatory is the first detector that is sensitive to a flux of neutrinos at the level of the Waxman–Bahcall bound. Indeed, the cosmic neutrino flux detected with IceCube is tantalizingly close to this bound [19, 20]. Note however that it was detected at energies much lower than those of the UHECRs, so that the two need not necessarily be connected.

3.1.5 Connection to High-Energy Gamma Rays

As already mentioned in section 3.1.1, high-energy neutrinos are always produced in conjunction with high-energy gamma rays in cosmic-ray interactions. When extragalactic sources are considered, measurements of the extragalactic diffuse gamma-ray background, *e.g.* by Fermi LAT [143], can be used to derive constraints on the diffuse flux of neutrinos from the same sources. The constraints depend on the production mechanism, *i.e.* whether the neutrinos and gamma rays are produced in pp or pγ interactions.

The case of pγ interactions has been discussed mostly in the context of cosmogenic neutrinos, *e.g.* in [46, 144]. Generally, constraints are more easily circumvented than in the pp scenario because the neutrino energy spectrum depends on the target photon spectrum, and the produced gamma rays are often attenuated by interacting with the ambient photons themselves, see *e.g.* [145, 146].

Conversely, a recent study by Murase *et al.* [147] has placed strong constraints on the neutrino energy spectrum at TeV–PeV energies. The study considers pp interactions in sources that are transparent to gamma rays up to 10 TeV, such as galaxy clusters or star-forming galaxies. Taking into account both Fermi LAT measurements of the extragalactic gamma-ray background and IceCube measurements of the cosmic neutrino flux, they find $\gamma \lesssim 2.1 - 2.2$ for the spectral index of the neutrino flux from these sources at TeV–PeV energies.

3.2 Candidate Source Classes

Many hypothetical sources of high-energy neutrinos have been proposed. As we consider the production of neutrinos in the sources of high-energy cosmic rays here, it is natural to begin with a discussion of the candidate sources of cosmic rays. A good starting point is the so-called *Hillas plot*, see section 3.2.1. Furthermore, as neutrinos with TeV energies play an important role in this work, it is evident that objects that emit gamma rays of such energies are candidate sources worth considering (section 3.2.2). Some specific candidate source classes within and outside of the Milky Way are outlined in section 3.2.3 and 3.2.4, respectively. Several model calculations for the neutrino flux from each of these potential sources exist, a selection is shown in section 3.2.5. A good review of possible high-energy neutrino sources can also be found *e.g.* in [108].

3.2.1 The Hillas Plot

If cosmic rays gain their energy through acceleration in astrophysical objects, these objects must be able to confine cosmic rays with energies lower than the maximum attainable energy. This typically requires the presence of a magnetic field. The Larmor radius r_L of a (relativistic) charged particle with energy E and charge number Z in a magnetic field with strength B is

$$r_L = \frac{E}{e \cdot Z \cdot c \cdot B}\,, \tag{3.20}$$

with the elementary charge e and the speed of light c. Hillas [148] has argued that the physical extent L of the cosmic-ray acceleration site should exceed at least twice the Larmor radius, *i.e.* $L > 2r_L$. More detailed, he finds that the characteristic velocity v of magnetic scattering centers (or the shock front velocity in case of first order Fermi acceleration) needs to be considered, so that $L > 2r_L/\beta$, where $\beta = v/c$. This yields the so-called Hillas criterion,

$$\left(\frac{E}{10^{20}\,\mathrm{eV}}\right) < 0.3 \cdot \frac{1}{2} \cdot Z \cdot \beta \cdot \left(\frac{L}{10^{12}\,\mathrm{km}}\right) \cdot \left(\frac{B}{\mathrm{G}}\right)\,, \tag{3.21}$$

where E, L, and B are expressed in convenient units.

Astrophysical objects can be compared to this criterion on the Hillas plot, displayed in fig. 3.4. For particular values of E, β, and Z, eq. 3.21 corresponds to a diagonal line on the plot (displayed is the limiting case $\beta = 1$ for $E = 10^{20}\,\mathrm{eV}$, and $Z = 1$ and $Z = 26$ for protons and iron nuclei, respectively). According to the Hillas criterion, only objects that lie above such a line on the plot are capable of accelerating the corresponding particles to the specified energy.

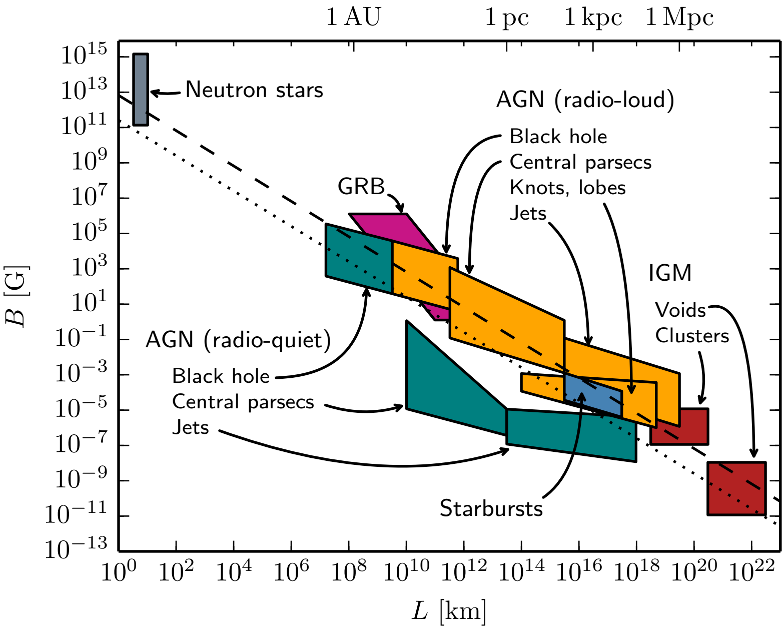

Figure 3.4 — *Hillas Plot.* The plot shows the physical extent L and the magnetic field strength B of a selection of astrophysical objects, as originally proposed by Hillas [148]. Displayed are neutron stars, gamma-ray bursts (GRB), different regions of active galactic nuclei (AGN), starburst galaxies, and galaxy clusters and voids in the intergalactic medium (IGM) (*cf.* section 3.2.3 and 3.2.4). The dashed (dotted) line indicates the Hillas criterion (eq. 3.21) for the acceleration of protons (iron) to $E = 10^{20}$ eV with $\beta = 1$. Reproduced from [149].

The Hillas plot is mostly employed to ascertain which sources can accelerate cosmic rays to the highest energies of 10^{20} eV or more. Evidently, there are not many objects meeting that condition; those that do are mostly objects outside our Galaxy. Environments theoretically capable of acceleration to lower energies (according to the Hillas criterion) are more numerous though, and not all possible candidates are displayed in the figure. There is hence a variety of astrophysical objects that need to be considered in the context of TeV–PeV neutrinos, as will be outlined in the next sections.

3.2.2 Sources of TeV Gamma Rays

Sources of gamma rays with TeV energies are good candidates for the emission of neutrinos with the same energies. If the gamma rays are produced in hadronic processes, *i.e.* in interactions of high-energy protons or nuclei, the simultaneous production of neutrinos is guaranteed. There are, however, also leptonic processes such as inverse Compton scattering of high-energy electrons that can produce TeV gamma rays. In this case, there would be no accompanying neutrinos.

The potential neutrino flux from a sample of galactic sources of TeV gamma rays, detected with the H.E.S.S. telescopes [150], was estimated by Kappes *et al.* in [151]. They find that a neutrino detector with 1 km^3 detection volume, situated on the northern hemisphere, would be able to detect several neutrinos per year from these sources.

Figure 3.5 shows the positions of a selection[4] of TeV gamma-ray sources in galactic coordinates. Note that the sources located within the Milky Way (green symbols) are clustered around the galactic plane, in particular around the galactic center. This is not the case for extragalactic sources (blue symbols), which are distributed isotropically.

3.2.3 Galactic Source Candidates

An extensive review of potential galactic sources of high-energy neutrinos is presented in [153]. Here, only two of the most promising candidates are outlined, namely shell-type supernova remnants (SNR) and pulsar wind nebulae (PWN). Both are residues of stellar explosions. Images of a supernova remnant and a pulsar wind nebula are displayed in fig. 3.6 (a) and (b), respectively.

Supernova Remnants

Supernova explosions occur *e.g.* when massive stars undergo a gravitational collapse at the end of their lifetime. In the explosion, the star's

---

[4] The source selection is taken from [152]. For PWN (AGN), only those whose flux level exceeds 10% (3%) of the Crab Nebula flux are shown.

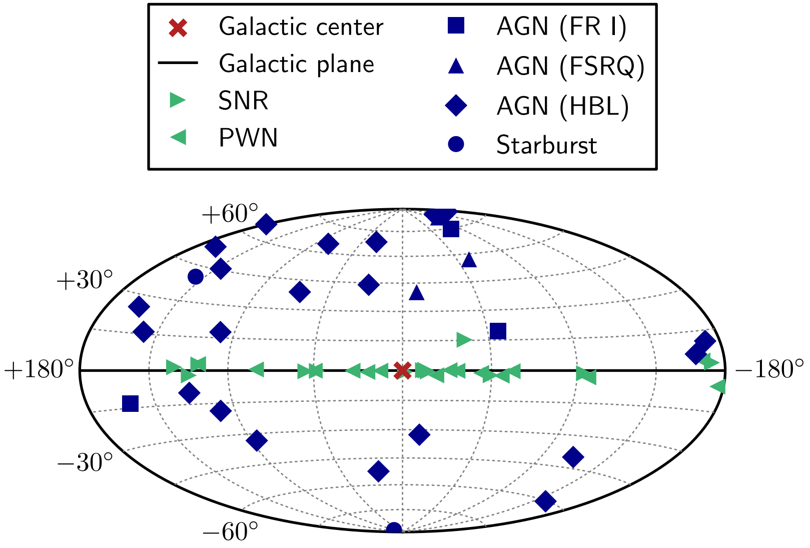

Figure 3.5 — *Skymap of Sources of TeV Gamma Rays.* Shown are the positions of a selection of TeV gamma-ray sources in a Hammer projection of the sky in galactic coordinates. Galactic sources are marked by green symbols, extragalactic sources by blue symbols. SNR: supernova remnant, PWN: pulsar wind nebula, AGN: active galactic nucleus (see section 3.2.3 and 3.2.4 for more information). Source positions taken from [152].

material is expelled at enormous velocities, thus driving a shock wave through the interstellar medium. Figure 3.6 (a) shows an image of the remnant of SN 1572, a supernova explosion within the Milky Way that was observed, among others, by the Danish astronomer Tycho Brahe in 1572. The shock wave is clearly visible at the outer edges of the remnant.

Cosmic rays can be accelerated at the shock front via the first order Fermi mechanism (*cf.* section 3.1.2). In fact, based on their energy release, supernova explosions are thought to be responsible for the bulk of cosmic rays in our Galaxy [107]. As such, they are also prime candidates for neutrino production, typically via the pp mechanism.

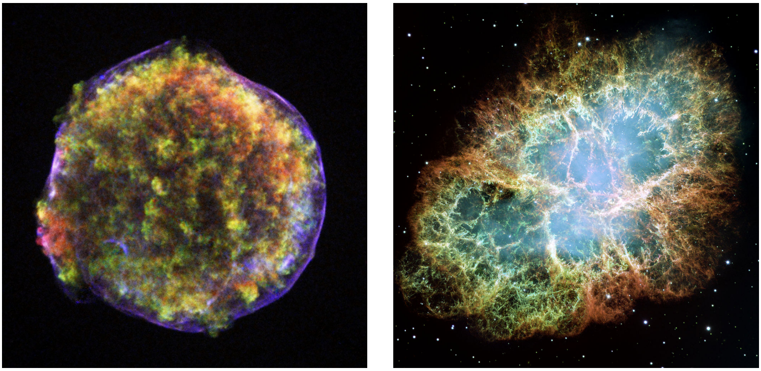
(a) (b)

Figure 3.6 — *Images of Galactic Neutrino Source Candidates.* (a) X-ray image of Tycho's supernova remnant. Credit: NASA / CXC / Rutgers / J.Warren & J.Hughes *et al.* (b) Composite image of the Crab Nebula. Credit: NASA, ESA, J. Hester and A. Loll (Arizona State University).

The expected neutrino flux from supernova remnants has been calculated *e.g.* in [151, 154, 155]. Neutrino emission from SNRs in the Cygnus region, a region with increased star formation rate in the Milky Way, was considered in [156]. Most studies find that the detection of only a few neutrinos per year can be expected in a neutrino detector such as the IceCube Neutrino Observatory, which renders a discovery challenging.

Pulsar Wind Nebulae

Pulsar wind nebulae are similar in nature to supernova remnants in that they are also the product of stellar explosions. The distinguishing feature is that PWN are powered by a central pulsar, *i.e.* a rapidly rotating neutron star. The pulsar drives a wind of relativistic particles, which then interact with the surrounding medium, producing gamma rays and, possibly, neutrinos. The most prominent PWN that can be observed from Earth is the Crab Nebula, depicted in fig. 3.6 (b). The pulsar wind can be seen as a blue haze in the center of the nebula. For a general review on pulsar wind nebulae, see *e.g.* [157].

Neutrino flux expectations from PWN are obtained *e.g.* in [158–161]. While some authors were optimistic concerning the detection of PWN in km^3-scale neutrino telescopes, this detection has yet to occur in the IceCube detector.

3.2.4 Extragalactic Source Candidates

While it is still unknown at which energies extragalactic cosmic rays begin to dominate the total cosmic-ray flux, it is rather evident that the cosmic rays of highest energies are accelerated outside the Milky Way [162] (based on the Hillas criterion, *cf.* fig. 3.4). This motivates to consider extragalactic objects also for high-energy neutrino emission, as has been done since a long time in the literature [47, 108, 163]. A selection of popular extragalactic candidate neutrino sources is introduced in the following.

Active Galactic Nuclei

Active galactic nuclei (AGNs) are compact regions in the centers of galaxies that appear very bright in electromagnetic radiation. The prevailing view is that these regions contain supermassive black holes that accrete surrounding matter, converting gravitational energy into radiation. The infalling matter forms an accretion disk. In many AGNs, relativistic jets perpendicular to the disk are observed. Depending on the observation angle with respect to the disk, AGNs exhibit different properties; this is often used to classify different types of AGNs [108]. A sketch showing the prevailing concept of the structure of AGNs is shown in fig. 3.7.

Several regions of AGNs are thought to be sites of cosmic-ray acceleration, such as the relativistic jets and the inner region close to the black hole. Therefore, these regions are also candidates for high-energy neutrino emission. Several models for neutrino emission from AGNs have been put forward, where generally photohadronic neutrino production is assumed. Stecker *et al.* predict the neutrino flux from the cores of AGNs, *i.e.* from the accretion disk region [42–44]. Most other models consider neutrino production in the relativistic jets, *e.g.* [141, 164, 165].

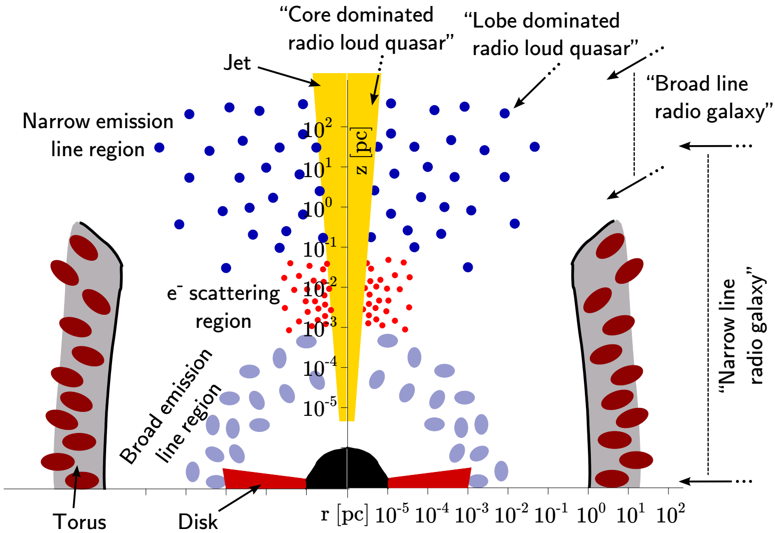
"Core dominated radio loud quasar"
"Lobe dominated radio loud quasar"
Jet
"Broad line radio galaxy"
Narrow emission line region
e⁻ scattering region
Broad emission line region
"Narrow line radio galaxy"
Torus
Disk
z [pc]
10^2 10^1 10^0 10^{-1} 10^{-2} 10^{-3} 10^{-4} 10^{-5}
r [pc] 10^{-5} 10^{-4} 10^{-3} 10^{-2} 10^{-1} 10^0 10^1 10^2

Figure 3.7 — *Sketch of an Active Galactic Nucleus.* Different regions of an AGN are shown as a function of their horizontal (r) and vertical (z) distance to the central black hole (both scaled logarithmically). As indicated, AGNs are often classified with respect to the angle under which we observe them. Most models predict neutrino emission either in the core region (close to the disk) or in the jets. Adapted from [166].

Gamma-Ray Bursts

Gamma-ray bursts (GRBs) are transient events that, for a brief period of 10^{-3} to 10^3 seconds, outshine every other source of gamma rays in the Universe by far [167]. They were first detected by a set of military satellites, operated by the US Air Force [168]. Their origin was longly debated, until dedicated satellite experiments successfully measured the so-called afterglow emission at longer wavelengths, determining that GRBs are extragalactic of origin and cosmologically distributed. Today, the generally adopted model for GRBs is the fireball shock model, which is illustrated in fig. 3.8. Long bursts (duration $> 2\,\mathrm{s}$) are very likely associated with the core-collapse of a supermassive star, whereas short bursts ($< 2\,\mathrm{s}$) are believed to be the result of two merging neutron stars, or the merging of a neutron star and a black hole. In both cases, jets with multiple relativistic shock fronts form, leading to the acceleration of particles. A general review on gamma-ray bursts is given in [167].

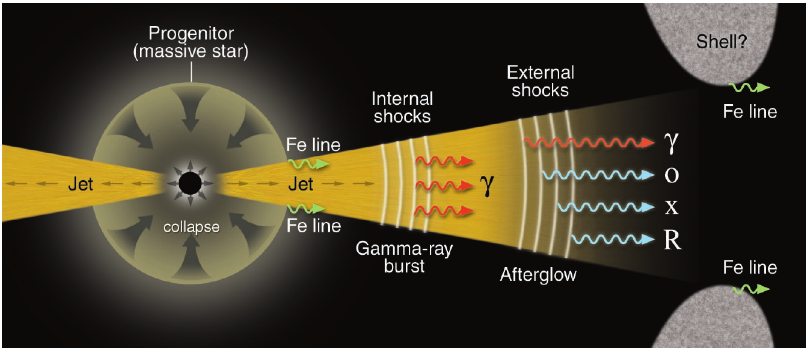

Figure 3.8 — *Sketch of a Gamma-Ray Burst.* In the jets, particles are accelerated at relativistically moving shock fronts. Neutrinos can be produced in photohadronic interactions of the accelerated cosmic rays (not shown). Taken from [169].

Gamma-ray bursts have been considered as cosmic-ray sources, and hence as neutrino sources, since a long time. On first approach, one would assume neutrinos to be produced in coincidence with the prompt gamma-ray emission. Two influential models for this characteristic type of neutrino emission from the burst were proposed by Waxman and Bahcall [139,170] and Guetta *et al.* [171]. These models, however, have been ruled out by IceCube searches for GRB neutrinos [172]. They were recently revised by Hümmer *et al.* [173], who predict significantly lower fluxes.

High-energy neutrinos are also predicted to be emitted during other phases of GRBs. For instance, Razzaque *et al.* predict neutrinos from prebursts of the stellar progenitor [174], whereas Waxman and Bahcall have also proposed a model of neutrino production during the afterglow phase [175]. Typically, it is assumed that neutrinos are produced in $p\gamma$ interactions in GRBs.

Starburst Galaxies

Starburst galaxies are galaxies with a highly increased star formation rate. As such, they are also host to a large number of supernova explosions, which, just as in our galaxy, are thought to accelerate cosmic rays. In addition, starburst galaxies have comparably large gas densities [176], so that neutrinos can be produced when cosmic rays interact with gas nuclei.

About 10% of nearby galaxies show increased star formation rates, and starburst activity increases rapidly with increasing distance [176], so that there is a substantial number of starburst galaxies in the Universe. Provided starburst galaxies are neutrino sources, this implies that even if each individual source is very weak, the cumulative flux from all sources could still be sizeable.

Loeb and Waxman have modeled the neutrino emission from starburst galaxies, finding a flux close to the Waxman–Bahcall bound [177]. Their model was reexamined by Stecker, who predicts significantly lower fluxes [178].

Galaxy Clusters

The largest gravitationally bound objects in the Universe are so-called galaxy clusters [179]. Shock fronts can form within these clusters *e.g.* when matter accretes onto filaments and knots of high density. Although magnetic field strengths within galaxy clusters are probably not larger than some microgauss, the structures are so large that cosmic rays could be accelerated at the shock fronts up to energies of $10^{18} - 10^{19}\,\mathrm{eV}$ [180] (*cf.* fig. 3.4).

A model based on the assumption that galaxy clusters are significantly contributing to the cosmic-ray flux just below the ankle at $6 \times 10^{18}\,\mathrm{eV}$ was proposed by Murase *et al.* [181]. They find that the neutrinos produced in association with the cosmic rays could be detectable in neutrino telescopes like the IceCube Neutrino Observatory.

3.2.5 Flux Predictions

Neutrino flux predictions for specific astrophysical objects typically vary between different authors, and sometimes, as experimental limits improve, also in time. Nevertheless, it is helpful to visualize some prototypical models, see fig. 3.9. The displayed models were proposed prior to the discovery of the cosmic neutrino flux at the IceCube experiment.[5]

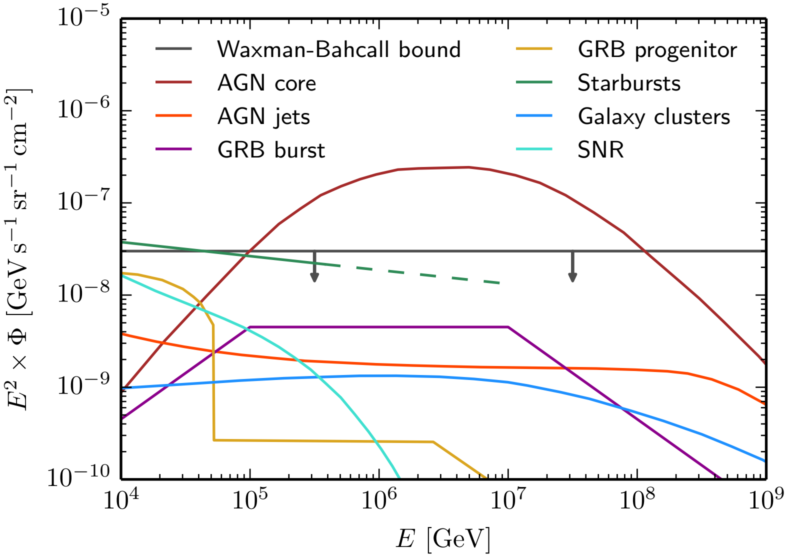

Figure 3.9 — *Neutrino Flux Predictions for Astrophysical Sources.* All-flavor neutrino fluxes are displayed, assuming a flavor composition of $\nu_e : \nu_\mu : \nu_\tau = 1 : 1 : 1$ at Earth. Shown are models for neutrinos from AGN cores [42–44], from AGN jets [165], from GRB bursts [45, 170], from GRB progenitors [174], from starburst galaxies [177], from galaxy clusters [181], and from galactic supernova remnants [155]. As a comparison, the Waxman–Bahcall upper bound is indicated [140]. The vertical axis is scaled with E^2 for better readability.

---

[5] The only exception is the SNR model [155], which was proposed after the discovery, but explicitly not scaled to explain the flux measured by IceCube.

Chapter 4

The IceCube Neutrino Observatory

> *"Fanciful though this proposal seems, we suspect that within the next decade, cosmic ray neutrino detection will become one of the tools of both physics and astronomy."*
>
> — Kenneth Greisen (1960) [10]

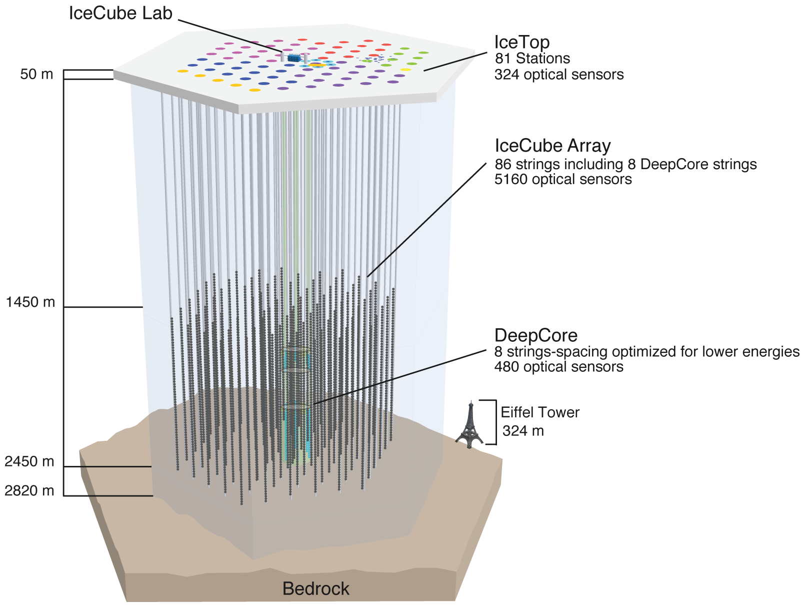
IceCube Lab
50 m
IceTop
81 Stations
324 optical sensors
IceCube Array
86 strings including 8 DeepCore strings
5160 optical sensors
1450 m
DeepCore
8 strings-spacing optimized for lower energies
480 optical sensors
Eiffel Tower
324 m
2450 m
2820 m
Bedrock

Figure 4.1 — *Sketch of the IceCube Neutrino Observatory.* Shown are the main IceCube array, the more densely instrumented DeepCore sub-array in the deep ice, and the cosmic-ray detector IceTop at the surface. The colored circles indicate detector units deployed in different seasons.

On May 13, 2011, the last seven IceCube detector strings were included into routine operation. Since then, the IceCube Neutrino Observatory – the world's largest neutrino detector, located at the geographical South Pole in Antarctica – has taken data in its final configuration. With this accomplishment, a long journey towards the construction of a km^3-sized neutrino telescope was finally completed. Beginning with Greisen's prophecy in 1960, it encompassed the pioneering (though never realized) DUMAND project, pursued for more than 20 years between 1973 and 1995; smaller prototype detectors in lake Baikal (since 1981) and the Mediterranean (since 1989); and IceCube's predecessor at the South Pole, AMANDA, in operation between 1993 and 2009. For an excellent review on this journey, see [13].

The IceCube Neutrino Observatory is placed at a unique location: the geographical South Pole. It employs the Antarctic glacier as a detection medium, registering neutrino interactions by detecting Cherenkov radiation from secondary particles with its 5,160 optical sensors, buried at depths between 1,450 and 2,450 meters below the surface (see fig. 4.1). The optical sensors, called Digital Optical Modules (DOMs), are arranged on 86 strings of 60 DOMs each, deployed between 2004 and 2010. In addition, the observatory features IceTop, a cosmic-ray detector consisting of 81 stations that are installed on the surface above the IceCube detector.

This chapter outlines some general aspects of IceCube (section 4.1), its detection principle (section 4.2) and main components (section 4.3), the detector simulation (section 4.4), as well as the observed event signatures (section 4.5) and corresponding reconstruction algorithms (section 4.6).

4.1 A Neutrino Telescope at the South Pole

From a scientific perspective, IceCube's location has a very convenient virtue: The local zenith angle is invariably connected to the declination of astrophysical objects.[1] This implies that the exposure is uniform in right-ascension, and particular objects are always observed under the same zenith angle. As an illustration, fig. 4.2 shows the positions of the same sources as in fig. 3.5, but in equatorial coordinates. Sources located at positive declinations are always observed through the Earth (the *northern sky*, top half of the map), whereas sources located at negative declinations are always above the horizon (the *southern sky*, bottom half of the map). Note that the majority of galactic sources, as well as the galactic center, are always above the horizon at the South Pole.

---

[1] In IceCube coordinates, the zenith angle θ varies from 0° for vertically downgoing particles to 180° for vertically upgoing particles, so that declination $\delta = \theta - 90°$.

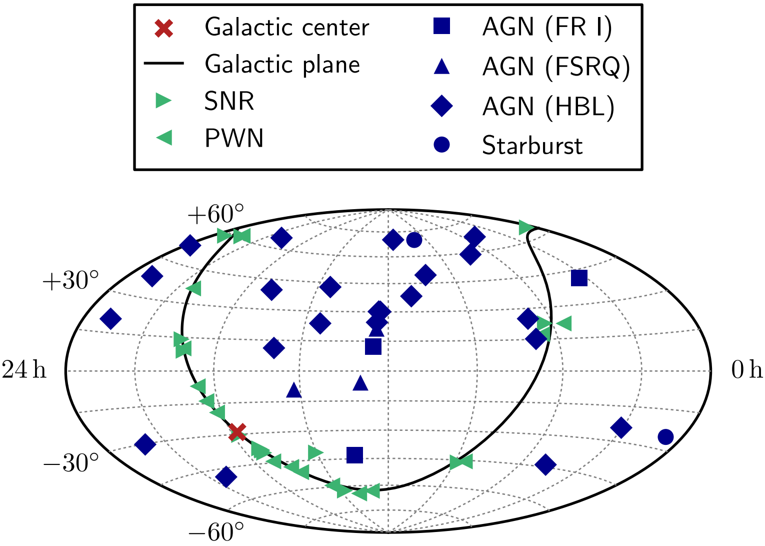

Figure 4.2 — *TeV Gamma-Ray Sources as Seen from South Pole.* Same as fig. 3.5, but using equatorial coordinates. Neutrinos from sources displayed in the top (bottom) half of the map always reach the IceCube detector from below (above) the horizon. Source positions taken from [152].

While neutrinos can reach the IceCube detector from all directions, neutrinos arriving from below have to traverse the Earth to do so. Because the interaction cross section increases with energy (*cf.* fig. 2.5), the Earth is no longer transparent to neutrinos at high energies. Electron and muon neutrinos are noticeably absorbed in the Earth above energies of 10 TeV, as shown in the left panel of fig. 4.3. Tau neutrinos are not absorbed; the tau leptons produced in their interactions immediately decay, producing a new tau neutrino (this is sometimes called *regeneration*). However, the energy of the tau neutrino is reduced, as illustrated in the right panel of fig. 4.3. This means that neutrinos of very high energies cannot reach the detector unaffected through the Earth, but only from above or from directions close to the horizon, where the overburden of material is still small.

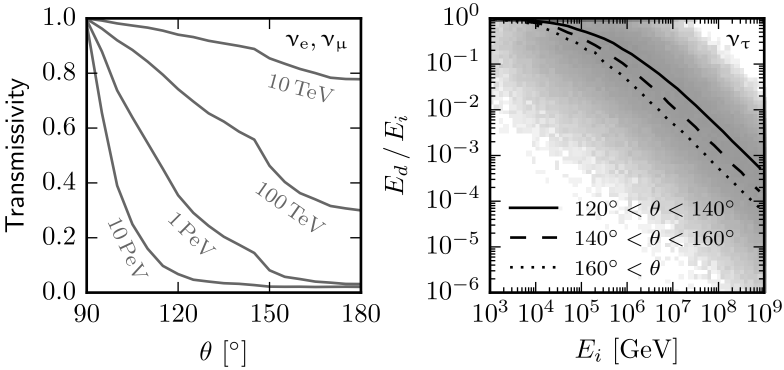

Figure 4.3 — *Neutrino Propagation through Earth.* Left: Transmissivity of electron and muon neutrinos of different energies as a function of the zenith angle θ. Right: Fractional energy retained by tau neutrinos, as a function of their initial energy E_i. The lines show mean values for different intervals of θ; the gray histogram shows a distribution of simulated neutrinos in the range $120° < \theta < 180°$.

4.2 Detection Principle

IceCube can detect high-energy neutrinos when they interact with nuclei or electrons in the ice inside or around the instrumented volume. Such interactions produce secondary particles, which, provided they are charged and relativistic, emit Cherenkov radiation. By analyzing this Cherenkov light, the initial properties of the neutrinos can be inferred. The interactions that lead to the emission of Cherenkov light are explained in this section, focusing on neutrino-nuclei interactions.

4.2.1 Neutrino Interactions in Ice

High-energy neutrinos interact with nuclei in the ice via deep inelastic scattering (*cf.* section 2.1.2). Different outcomes are possible, according to the neutrino flavor and the type of interaction. Four cases can be distinguished, as shown in fig. 4.4: neutral-current interactions of any neutrino flavor (a), and charged-current interactions of electron, muon, and tau neutrinos (b)–(d). In all cases, a hadronic particle shower[2] is initiated at the interaction point. In charged-current interactions, a charged lepton is produced in addition, corresponding to the flavor of the interacting neutrino.

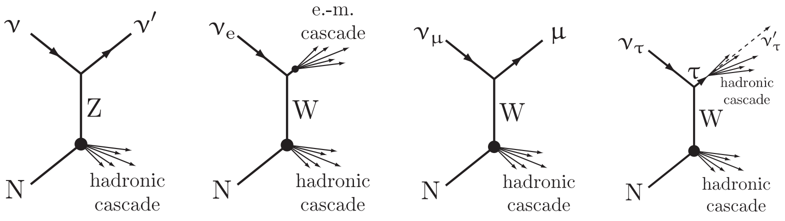

(a) (b) (c) (d)

Figure 4.4 — *Schematic Diagrams for Neutrino Interactions in Ice.* (a) Neutral-current interaction. (b)–(d) Charged-current interactions of ν_e, ν_μ, and ν_τ, respectively. Taken from [182].

Charged leptons behave very differently in ice. Electrons immediately initiate an electromagnetic particle shower by emitting bremsstrahlung photons, quickly radiating all their energy. Like hadronic showers, electromagnetic showers extend over a range of not more than a few meters in ice. In contrast, thanks to their higher mass, muons can travel considerably larger distances with little energy loss. The same is true in principle for taus; however, their very short lifetime usually prohibits long propagation distances, except at very high energies above $\sim 1\,\mathrm{PeV}$. With their decay, taus usually initiate another hadronic particle shower.[3] Average propagation distances of muons and taus as well as average extents of electromagnetic and hadronic showers are depicted in the left panel of fig. 4.5.

---

[2] *Hadronic* in this case means that the major part of the energy is carried by hadronic particles. Every hadronic shower also has an electromagnetic component, which constantly increases by the decay of neutral pions.

Because muons can travel such long distances, it is worthwhile to investigate the processes by which they lose energy in more detail. The total average energy loss of muons along their path is shown in the right panel of fig. 4.5, along with the main contributing processes. While low-energy muons mainly lose energy due to ionization, energy losses by pair production, bremsstrahlung, and photo-nuclear interactions dominate above energies of $\sim 1\,\mathrm{TeV}$. These processes are all stochastic in nature, *i.e.* the muons deposit their energy at irregular intervals rather than continuously.

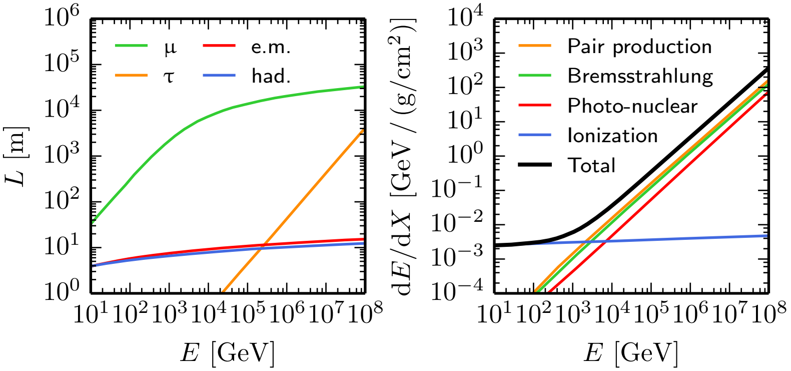

Figure 4.5 — *Secondary Particle Propagation in Ice.* Left: Average propagation distance of muons (μ) and taus (τ), and average extent of electromagnetic (e.m.) and hadronic (had.) particle showers (LPM effect [183, 184] not included), in water, as a function of the initial energy E. Corresponding distances in ice are similar [185]. Reproduced from [186]. Right: Energy loss per unit profile density $\mathrm{d}E/\mathrm{d}X$ of muons for different processes, as a function of the muon energy E. Reproduced from [187].

4.2.2 Cherenkov Radiation

Cherenkov radiation is emitted by particles that propagate through a medium with a speed exceeding that of light in the medium. This effect was first observed by Pavel Cherenkov [188]. It is the result of a coherent superposition of electromagnetic waves that arise from the polarization of the medium due to the passing particle. A sketch of the effect is shown in fig. 4.6, illustrating that the waves superimpose coherently only if the particle moves faster than light in the medium.

---

[3] Note however that $\sim 17\%$ decay into electrons and muons, respectively [51].

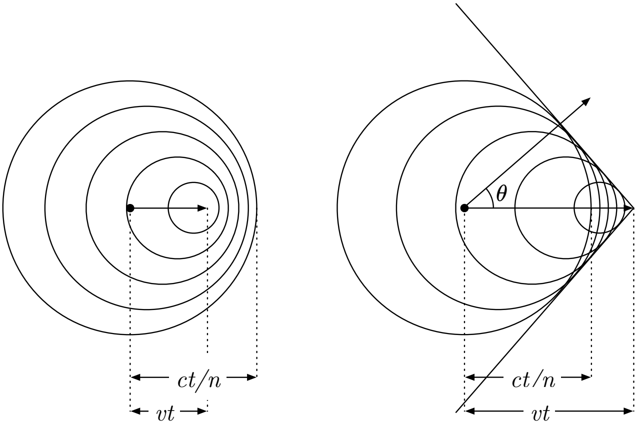

Figure 4.6 — *Sketch of the Cherenkov Effect.* The left (right) panel shows a particle propagating for a time t with a speed v lower (higher) than the speed of light c/n in a medium with refractive index n. The circles represent wave fronts of light emitted as the passing particle polarizes the medium. If $v > c/n$, a Cherenkov cone with half-opening angle θ forms. Adapted from [189].

As can be seen from the sketch, the Cherenkov light is emitted under a characteristic angle θ. This angle is determined solely by the refractive index n of the medium and the speed v of the particle,

$$\cos\theta = \frac{1}{n\beta}\,, \tag{4.1}$$

with $\beta = v/c$. For highly relativistic particles propagating in ice, $\beta \approx 1$ and $n \approx 1.31$ [190], and thus $\theta \approx 40°$.

The number of emitted Cherenkov photons per unit path length x and wavelength λ for particles with charge ze is given by the Frank–

Tamm formula,

$$\frac{\mathrm{d}^2 N}{\mathrm{d}x \mathrm{d}\lambda} = \frac{2\pi\alpha z^2}{\lambda^2} \left(1 - \frac{1}{\beta^2 n^2(\lambda)}\right) , \tag{4.2}$$

where $\alpha \approx 1/137$ is the fine structure constant and the refractive index n depends on the wavelength[4] [51]. A relativistic particle with $\beta \approx 1$ passing through ice produces ≈ 250 photons per cm in the wavelength interval between 300 nm and 500 nm, where photosensors are typically most sensitive [192].

In neutrino telescopes, Cherenkov radiation is emitted by muons and taus, but also by the charged particles in hadronic and electromagnetic particle showers. The amount of light emitted by an electromagnetic shower is proportional to the total track length of particles in that shower, which is in turn proportional to the total energy of the shower [193]. This argument is also valid for showers initiated by stochastic energy losses of muons along their track. Hadronic showers are more complicated than electromagnetic ones, however, a hadronic shower generically produces less light than an electromagnetic shower of the same energy.[5] The ratio between the light yield of a hadronic shower and an electromagnetic shower is $\sim 80\%$ for an initial energy of 1 TeV and increases with energy [193].

4.3 Detector Components

The principal detection unit of the IceCube Neutrino Observatory is the Digital Optical Module (DOM). The full detector consists of 5,160 DOMs, buried deep in the ice at the South Pole. They are attached to 86 cables, called *strings*, that provide power and communication to the central data acquisition system to them. 78 of the strings are arranged on a hexagonal grid with 125 m spacing and host 60 DOMs each, placed 17 m apart between depths of $1,450$ and $2,450$ m below the surface. These strings instrument a volume of $\sim 1\,\mathrm{km}^3$ of ice.

---

[4] In particular, the refractive index is very close to unity for small wavelengths, so that the integral of eq. 4.2 over λ is finite [191].

[5] The main reasons are the production of slow neutrons, energy losses in the form of hadronic binding energies, and the higher Cherenkov threshold of charged hadrons compared to electrons [193].

The remaining 8 strings form the so-called DeepCore array. They are installed in between regular strings in the center of the array and host 10 DOMs placed every 10 m between depths of 1, 750 and 1, 850 m and 50 DOMs placed every 7 m between depths of 2, 100 and 2, 450 m. While with the regular strings it is possible to detect neutrino interactions above ∼ 100 GeV, the DeepCore array allows the observation of interactions down to ∼ 10 GeV [194].

The strings were deployed at South Pole during seven successive austral summers between 2004 and 2010. Data taking commenced already in 2005, with only one operational string. Each following year, the existing detector was expanded by newly deployed strings, forming the partial configurations that are displayed in fig. 4.7. Data analyzed in this work was taken with the 40-string configuration (IC40, 2008–2009), the 59-string configuration (IC59, 2009–2010), the 79-string configuration (IC79, 2010–2011), and the final 86-string configuration (IC86, since 2011).

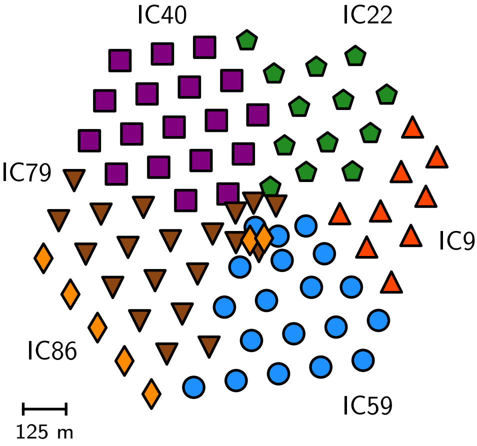

Figure 4.7 — *IceCube Configurations.* Top view indicating the relative positions of all strings. The labels (ICX) mark strings that were added to the array in one season to form a new configuration with X strings in total.

The IceTop cosmic-ray detector is installed on the surface of the ice above the IceCube detector. It consists of 81 stations, where each station comprises two ice-filled tanks that are monitored by two DOMs each [195]. Charged particles created in cosmic-ray air showers that pass through the tanks emit Cherenkov radiation, which is recorded by the two DOMs. The IceTop detector is used to study the cosmic-ray energy spectrum and composition, but also as a veto detector for the main IceCube array. In this work however, IceTop data are not analyzed.

In the remainder of this section, some important components of the IceCube detector are explained in more detail. The discussion is largely based on references [196–200], to which the reader is referred for further details.

4.3.1 The Digital Optical Module

The Digital Optical Module is the central component of IceCube. It consists of a 25 cm-diameter photomultiplier tube (PMT) and several electronics boards, contained within a 35.6 cm-diameter glass pressure housing (see fig. 4.8). The PMT signal is read out and digitized within the DOM, so that each module represents an autonomous detection unit.

The main electronics board accommodates two systems that digitize the PMT signal: a custom analog transient waveform digitizer (ATWD) samples the signal every 3.3 ns for a time interval of up to 422 ns, and a commercial fast analog-to-digital converter (FADC) samples the signal every 25 ns for up to 6.4 µs. The digitized PMT signal is transmitted via the cable to the surface whenever it exceeds a threshold of 0.25 photoelectrons; this is referred to as a *hit*. If a neighboring or next-to-neighboring DOM on the same string also exceeds this threshold within 1 µs, the full 6.4 µs-long waveform is transmitted (this is called *local coincidence*), otherwise only three samples of the FADC around the peak value are sent.

Another board, the flasher-board, hosts 12 LEDs pointing radially outwards, 6 horizontally and 6 pointing upwards at an angle of 48°. These LEDs are used in so-called flasher runs, which are regularly conducted for calibration purposes.

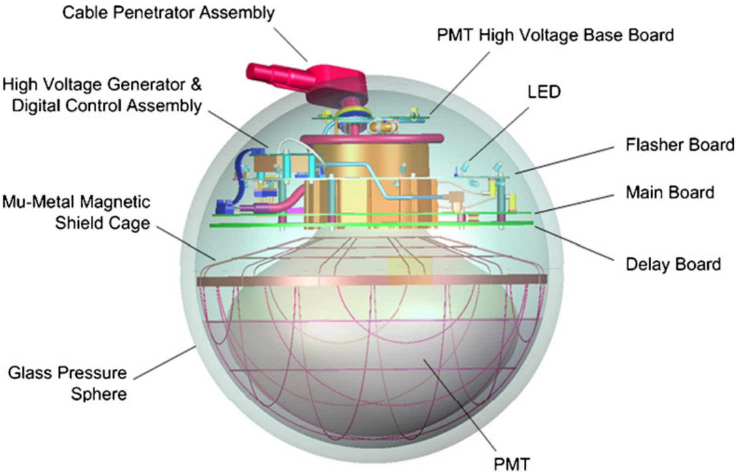
Cable Penetrator Assembly
PMT High Voltage Base Board
High Voltage Generator & Digital Control Assembly
LED
Flasher Board
Main Board
Mu-Metal Magnetic Shield Cage
Delay Board
Glass Pressure Sphere
PMT

Figure 4.8 — *The IceCube Digital Optical Module.* Sketch showing the individual components of the IceCube Digital Optical Module. Taken from [196].

4.3.2 The Deep Antarctic Ice

The deep Antarctic ice belongs to the clearest natural media found on Earth, allowing photons to travel for hundreds of meters before being absorbed. Compared to clear water, however, it has relatively large scattering coefficients, meaning that light quickly diffuses in the ice. Moreover, the ice is an inhomogeneous detection medium. This is illustrated in fig. 4.9, which shows the scattering and absorption coefficients of the ice as a function of depth and wavelength; the coefficients vary strongly with depth. The inhomogeneity is a result of the historical growth of the Antarctic glacier by snow accumulation; horizontal layers with more scattering and absorption correspond to larger deposits of dust and soot in the past [201].

Several models of the optical properties of the ice were developed, based on measurements of the dust concentration performed during string deployment and calibration flasher runs. The models describe the ice as a layered structure, with uniform properties within each

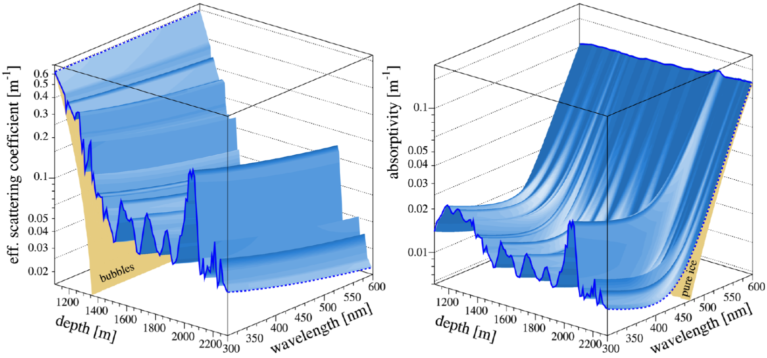

Figure 4.9 — *Light Scattering and Absorption in South Pole Ice.* Displayed are the effective scattering (left) and absorption (right) coefficient as a function of depth below the surface and photon wavelength. The region with strong scattering and absorption around depths of 2,000 m is referred to as *dust layer*. Taken from [198].

layer. Recent studies have shown that these layers are tilted with respect to the vertical axis [199], and that the scattering is anisotropic, *i.e.* the light is scattered preferably into the flow direction of the Antarctic glacier [202].

The ice model is an important ingredient to the production of simulation data for the IceCube experiment (see section 4.4). Because the knowledge about the optical properties of the ice has gradually improved over the years, different ice models were used for the production of simulation data sets. Specifically, data taken during the construction phase of IceCube are usually compared to simulation data available at the time, which are often based on ice models that are superseded by now.

4.3.3 Data Acquisition and Online Filtering

The data acquisition system (DAQ) is a software trigger algorithm that combines the incoming stream of DOM hits into physics events. Multiple trigger conditions exist, where the simplest condition is the *simple multiplicity trigger* (SMT). The data analyzed in this work satisfy the

SMT-8 trigger, which requires 8 local coincidence hits within a time window of 5 µs. The readout window contains all hits that satisfy this condition, as well as the hits in the preceding 4 µs and subsequent 6 µs.

The full IceCube detector is triggered more than 2,000 times a second. The main cause are atmospheric muons that penetrate down to the detector (see chapter 5 for a more detailed explanation). Since the data are transferred into the North via a satellite with limited bandwidth, not all triggered events can be sent. Instead, the event stream is filtered by a computing system at South Pole, the so-called *online filter*.

In order to decide which events are interesting enough to be transmitted, their properties are reconstructed in several steps. First, *pulses* are extracted from the digitized waveforms by deconvolving them with single-photoelectron pulse templates; each pulse is specified by its arrival time and the extracted number of photoelectrons. Based on these pulses, simple reconstruction algorithms try to infer basic properties of the light-emitting particle, such as its energy, direction, and interaction time and vertex. This information is then used by the filter algorithms to decide whether an event is transmitted or not.

There are several filter algorithms, tailored to the different event signatures in the IceCube detector (see section 4.5). The event samples analyzed here were selected by three different filters, the cascade filter, the muon filter, and the EHE filter. The cascade filter is designed to select spherical, shower-like events, whereas the muon filter aims at selecting elongated, track-like events. Finally, the extremely-high-energy (EHE) filter selects any type of event with a minimum number of 1,000 photoelectrons recorded in all DOMs.

4.4 Detector Simulation

In the process of selecting neutrino candidate events, it is essential to verify the selection process through Monte-Carlo simulations. To this purpose, the IceCube Collaboration has developed a simulation framework that describes the complete process of neutrino generation, propagation, interaction, and detection. Neutrino event samples simulated with this framework can then be compared to the experimental data.

Generation and propagation of neutrinos is handled by a software package called NeutrinoGenerator, which is based on the ANIS neutrino event generator [58]. The program injects neutrinos with a particular flavor, energy, and direction at the surface of the Earth, checks whether they are absorbed before reaching the detector and, if not, forces an interaction within a volume that contains the IceCube detector and its surroundings. Each generated neutrino is assigned a weight that is proportional to its generation and interaction probability. Using these weights, the simulated neutrino samples can be used to describe arbitrary neutrino fluxes.

The next step in the simulation chain is to propagate the secondary particles created in the interaction and to calculate their energy losses and light yield. For secondary muons and taus, this is performed by the Muon Monte Carlo (MMC) program [187][6], whereas particle showers are treated with the Cascade Monte Carlo (CMC) program [203].

Subsequently, the Cherenkov light produced by the secondary particles needs to be tracked on its path to the IceCube DOMs, taking into account scattering and absorption in the ice [199]. This can be done by direct simulation of the photon propagation for each simulated event [204]; however, this approach is often computationally prohibitive. Instead, the photon propagation is usually performed ahead of time for various geometrical configurations of the light emitter and detector. The results, stored in multi-dimensional tables [205], can then be accessed during event simulation by evaluating spline functions fitted to these tables [206].

Finally, the photon detection in the IceCube DOMs is simulated, based on laboratory measurements of the photomultiplier tubes contained in the DOMs [197]. The description of this process requires detailed knowledge *e.g.* about the efficiency of the photocathode, the angular response of the DOM as a whole, and the digitization electronics. From this point on, the simulated data can be treated in the same way as the experimental data, and are subjected to the same event selection algorithms. This allows the estimation of background rejection and signal selection efficiencies, and generally serves as a verification tool.

---

[6] MMC is written in Java; recent simulations often use PROPOSAL [185], the C++ translation of MMC.

4.5 Event Signatures

As already mentioned in section 4.2, the signature that a neutrino interaction leaves in the IceCube detector depends upon the flavor of the interacting neutrino and the type of interaction. Here, we define four different signatures, all displayed in fig. 4.10.

The first two signatures, (a) and (b), are the result of charged-current interactions of muon neutrinos. The muons created in such interactions can travel several kilometers in ice, leading to elongated, track-like signatures. In (a), the neutrino interaction happens outside the instrumented volume of IceCube, resulting in a *throughgoing track* signature. Contrarily, (b) shows a *starting track*, resulting from a neutrino interaction inside the IceCube detector.

A *shower* event is displayed in (c). These events result from neutral-current interactions (in which case there is a single hadronic shower) and from charged-current interactions of electron neutrinos (in which case there is an electromagnetic and a hadronic shower); these cannot be distinguished. The typical extent of showers (a few meters) is much smaller than the average spacing between adjacent strings (125 m), so that the light emission appears point-like. The strong scattering of the light in the ice then leads to a spherical hit pattern in the detector.

Charged-current interactions of tau neutrinos constitute a special case. At energies below $\sim 1\,\mathrm{PeV}$, the decay length of the produced tau is so short that the showers at the interaction vertex and the decay point overlap and cannot be separated. In this case, the signature is again a shower as displayed in (c). With increasing energy however, the tau decay length also increases and the two showers may be separated. This is referred to as *double bang* signature and shown for a simulated event with a very high energy of 200 PeV in (d). Double bang events have not been observed in experimental data yet.

4.6 Event Reconstruction

Event reconstruction is used to derive estimates of the fundamental properties (*parameters*) of the particle(s) that have emitted the Cherenkov radiation. For throughgoing track events, these are the direction of the muon and its energy loss pattern along the track. For

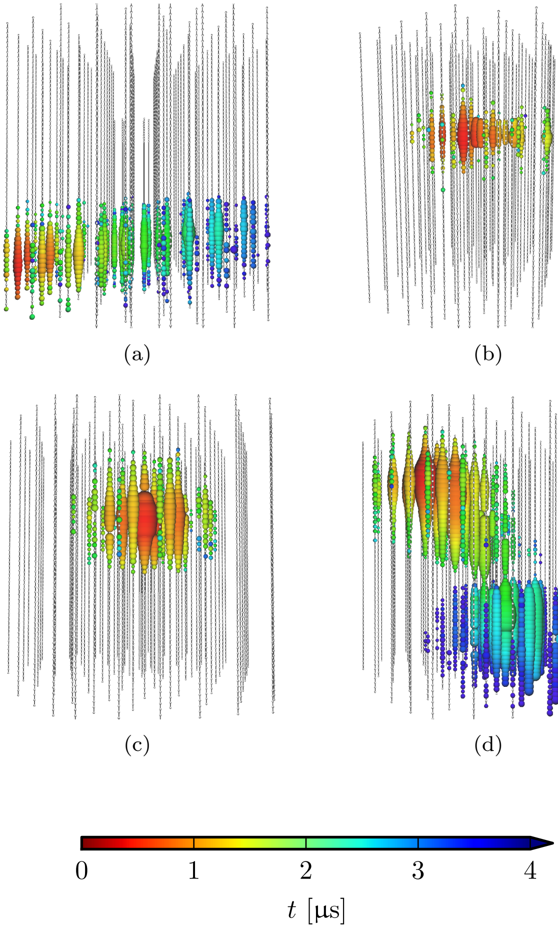

Figure 4.10 — *Event Signatures in the IceCube Detector.* The size of the DOMs indicate the number of recorded photoelectrons, the color marks the photon arrival time (red early, blue late, see scale at the bottom). (a) Throughgoing track, $E \approx 140\,\mathrm{TeV}$. (b) Starting track, $E \approx 70\,\mathrm{TeV}$. (c) Shower, $E \approx 1\,\mathrm{PeV}$. (d) "Double bang", $E \approx 200\,\mathrm{PeV}$. The events in (a)–(c) are experimental data, the event in (d) was simulated.

starting tracks, the time and position of the interaction vertex and the energy of the initial shower can be reconstructed in addition. Fundamental properties of shower events are the time and position of the interaction vertex, the direction of the particle shower, and its total deposited energy. The reconstruction of double bang events is more complex and, as such events have not been detected yet, not covered here.

One of the basic challenges in the analysis of IceCube data is the selection of relatively few neutrino events from the vast background of atmospheric muon events (see chapter 5). Because of the large background, the application of computationally extensive reconstruction algorithms to the full event sample is prohibitive. Rather, a staged approach is taken: Simple, computationally inexpensive "first-guess" algorithms are applied to all events. Events that appear background-like based on the results of these algorithms are rejected, so that more elaborate algorithms can be applied to the remaining data. This procedure is repeated several times, using evermore complex reconstruction algorithms, until the background is sufficiently reduced. The intermediate steps are referred to as event selection *levels*. The first selection levels are common to all analyses, subsequent levels become increasingly specialized to the analysis in question.

A short outline of higher-level reconstruction algorithms relevant for this work is given here. For more detailed information, see [207–210], upon which the following discussion is based.

4.6.1 Track Reconstruction

There are three important higher-level track reconstruction algorithms, which differ in the track parameters that they aim to reconstruct and their treatment of photon propagation in the ice.

The first algorithm is mainly used to reconstruct the direction of a track. It uses so-called *Pandel functions* [211], which are analytic probability density functions (PDFs) of the residual time that a photon needs to propagate from its emission point to a DOM after accounting for the geometric time, *i.e.* the time that the photon needs if it travels along the geometrically shortest path. The PDFs can be calculated for each DOM and depend on the assumed properties of the track; the most likely track parameters are those that maximize the product of

PDFs over all DOMs. This reconstruction algorithm achieves an angular resolution of better than 1° for track events, as has been verified with observations of the cosmic-ray moon shadow [212] (see fig. 4.11).

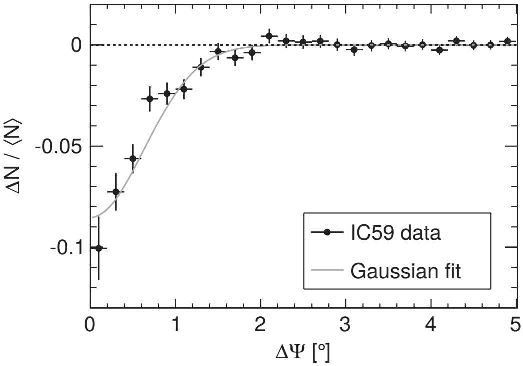

Figure 4.11 — *The Cosmic-Ray Moon Shadow.* Shown is the background-subtracted number of cosmic-ray induced muons as a function of the angular separation from the direction of the moon, observed with the 59-string configuration of IceCube. A clear deficit is observed at the position of the moon, this is referred to as the moon shadow and can be used to infer the angular resolution of the track reconstruction algorithm. The fitted Gaussian has a width of $0.63° \pm 0.04°$. Taken from [212].

The second algorithm reconstructs the energy of a muon that enters the detector, or starts inside it. As an input, it requires the direction of the track, which can be obtained with the previous algorithm. In its simplest form, the algorithm scales a template muon to the observed pattern of light deposition. Because muons lose energy stochastically and thus exhibit large event-to-event variations, this approach achieves a poor energy resolution. Better results can be obtained by splitting the track into several segments, and then fitting templates to each segment separately. This yields the energy loss pattern of the muon along its track, which can be used to infer the total energy of the incoming muon. The energy resolution that is achieved by this algorithm is displayed in fig. 4.12.

Finally, the third algorithm treats a muon as a series of energy depositions (*cascades*) along a track and scales these cascades to match the

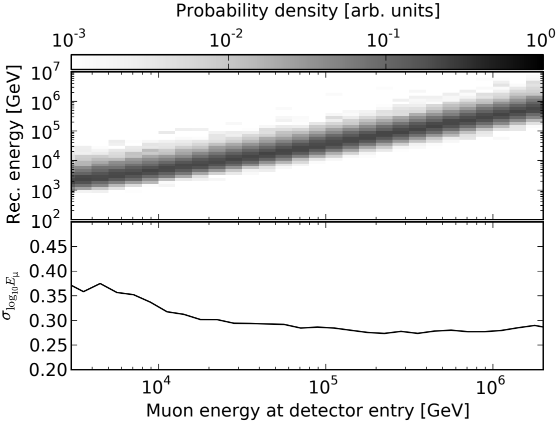

Figure 4.12 — *Muon Energy Reconstruction Performance.* The top (bottom) panel shows reconstructed muon energies (muon energy resolution) as a function of the muon energy at detector entry. Adapted from [210].

energy loss pattern of the muon. The expected signal from a cascade in a DOM is computed by evaluating a pre-calculated 5-dimensional table, obtained through photon-tracking simulations [205], and interpolated with spline functions [206] (similar as in event simulation, *cf.* section 4.4). This expected signal, which depends on the parameters of the assumed track, is then compared to the measured signal, assuming that the photon detection probability in each DOM follows a Poisson distribution. This yields a likelihood value for each combination of a cascade and a DOM. The light emitted by each cascade may be observed by any DOM in the detector, so that the combination of all cascades and all DOMs yields a linear equation system. For a given track direction, this system can be solved analytically. The algorithm then consists of two steps which are successively repeated; first a track direction is chosen, followed by solving the linear equation system to obtain the individual energy depositions. This procedure is followed until the product of likelihoods over all DOMs is maximized, either by performing a grid search or by using an optimization algorithm. In this way, the algorithm is capable of reconstructing both the direction of a muon as well as its energy losses along the track. Because of its complexity and high computational demands however, it is typically applied only to relatively small samples of events.

4.6.2 Shower Reconstruction

The prevailing algorithm used for shower reconstruction at high event selection levels is a variant of the third algorithm in the previous section. As the light deposition pattern of a shower is simpler than that of a muon, it can be applied also to larger event samples. The main difference to the track-algorithm is that instead of assuming many cascades along a track, a single cascade at a specific vertex is assumed. The likelihood is then maximized to obtain the time, vertex, direction, and energy deposition of the shower that fits the observed light pattern best. The resolution in energy and direction achieved by this reconstruction algorithm is displayed in fig. 4.13.

4.6.3 Relation to Neutrino Properties

It should be noted that the reconstructed properties of showers and tracks do not necessarily immediately correspond to properties of the interacting neutrino. On the contrary, for throughgoing tracks, the point of interaction cannot be determined and the reconstructed energy of the muon track at the detector represents only a lower limit on the initial neutrino energy. A similar argument applies to neutral-current interactions, in which the neutrino leaves the detector with an indeterminable fraction of its initial energy. Only in charged-current ν_e interactions (and, in some cases, charged-current ν_τ interactions) does the neutrino deposit all of its energy inside the instrumented volume of the detector, thus allowing one to obtain a meaningful estimate of the neutrino energy.

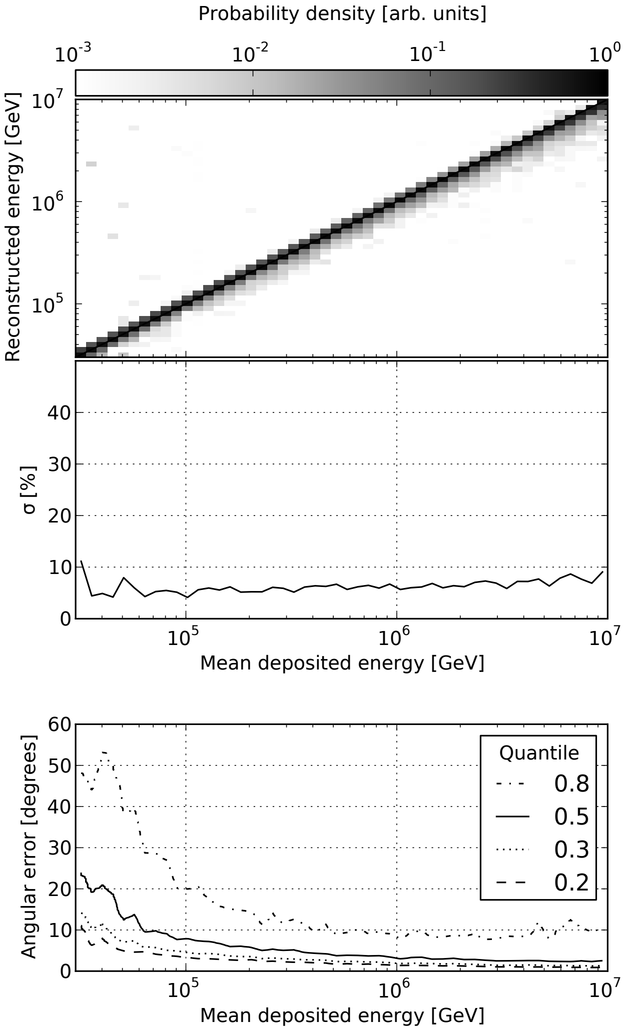

Figure 4.13 — *Shower Reconstruction Performance.* The top plot shows reconstructed shower energies (top panel) and shower energy resolution (bottom panel) as a function of the shower energy deposit. The bottom plot shows the angular resolution for shower events as a function of the shower energy deposit. Taken from [210].

Chapter 5

Atmospheric Backgrounds in Neutrino Telescopes

> *"For the rain it raineth every day."*
>
> — William Shakespeare (Feste's Song)

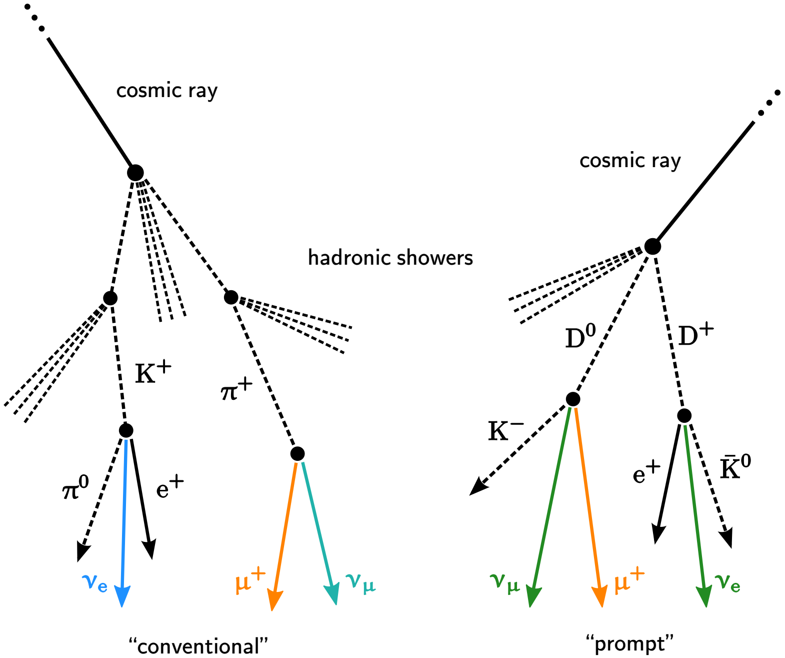

cosmic ray
hadronic showers
cosmic ray
K+
π+
D0
D+
K−
π0
e+
e+
K̄0
νe
μ+
νμ
νμ
μ+
νe
"conventional"
"prompt"

Figure 5.1 — *Sketch of Two Atmospheric Air Showers.* Muons and neutrinos from pion and kaon decays are referred to as *conventional*; those from the decay of charm mesons as *prompt*.

Superimposed on any flux of cosmic neutrinos is a steady “rain” of particles that is created in air showers in the Earth’s atmosphere. Some of these particles, namely muons and neutrinos, can reach underground neutrino telescopes like the IceCube detector; they are thus a background to searches for cosmic neutrinos. Ironically, the air showers are induced by the very same cosmic rays whose origin the cosmic neutrinos may help to reveal.

An exemplary sketch of two air showers, reduced to the relevant parts, is displayed in fig. 5.1. The shower on the left shows the production of muons and neutrinos via the decay of pions and kaons. These constitute the majority of particles reaching the IceCube detector and are commonly referred to as *conventional atmospheric muons and neutrinos*. While muons decay into neutrinos, too, their long mean lifetime of 2.2 μs [51] prevents them from doing so before reaching the detector if their energy exceeds a few GeV [41]. Neutrinos from the decay of atmospheric muons are hence neglected in this work.

As indicated, pions and kaons do not always decay, but often interact again with air molecules. The interplay between decay and interaction is governed by the density of the atmosphere and the energy and lifetime of the particle. For a given atmospheric density and particle, the *critical energy* is defined as the energy at which decay and interaction are equally likely; below, decay prevails, above, interaction is more likely. In the Earth’s atmosphere, the critical energy of charged pions is $\approx 115\,\mathrm{GeV}$, that of charged kaons is $\approx 850\,\mathrm{GeV}$, and that of neutral, long-lived kaons is $\approx 205\,\mathrm{GeV}$ [83]; these are all well below the energy ranges of the event samples analyzed in this work ($> 1\,\mathrm{TeV}$). Because the pions and kaons lose energy when interacting, the energy spectrum of conventional atmospheric muons and neutrinos in the energy range considered here is steeper ($\simeq E^{-3.7}$) than that of the primary cosmic rays ($\simeq E^{-2.7}$).

At high energies, *prompt atmospheric muons and neutrinos* become important. As shown in the right part of the figure, these result from decays of mesons that contain heavy quarks (mostly charm quarks), such as D-mesons (or, more generally, *charm mesons*). They are called *prompt* because charm mesons have mean lifetimes of $10^{-12}\,\mathrm{s}$ or less and thus immediately decay at all energies relevant here (the critical energies are larger than $10\,\mathrm{PeV}$ [83]). Consequently, the energy spectrum of prompt atmospheric muons and neutrinos follows that of the primary cosmic rays, and is expected to surpass the corresponding conventional spectrum at high energies. However, neither prompt atmospheric muons nor neutrinos have been experimentally observed yet, so that predictions for their contribution to the total flux are uncertain.

This chapter begins with a brief outline of the basic properties of atmospheric muons (section 5.1) and neutrinos (section 5.2). Thereafter, techniques to reject these backgrounds to search for cosmic neutrinos are introduced in section 5.3.

5.1 Atmospheric Muons

5.1.1 Flux Characteristics

The vast majority of particles detected by the IceCube detector are atmospheric muons. In fact, the data acquisition system of IceCube is mainly triggered by atmospheric muons; the total trigger rate as a function of time is shown in fig. 5.2. In addition to the abrupt jumps resulting from the addition of new detector strings, a periodic variation of the trigger rate is visible. This variation is caused by seasonal density variations in the atmosphere. With increasing density, interaction of pions and kaons becomes more likely with respect to their decay, so that fewer muons are produced, and vice versa.

The atmospheric muon flux has been measured up to energies of $\sim 100\,\mathrm{TeV}$ at ground level; a compilation of measurements is presented *e.g.* in [213]. Besides the energy spectrum, the ratio of positive and negative muons, μ^+/μ^-, is an interesting observable; it allows to infer the ratio of kaons and pions in the air shower [214].

Except in very optimistic scenarios, the transition from conventional to prompt atmospheric muons is expected to occur at PeV energies [215]. While a measurement of the prompt atmospheric muon component would be interesting in itself, it would also be of great interest for neutrino telescopes. First, because atmospheric muons are a major background to cosmic neutrino searches, and second, because properties of the prompt atmospheric neutrino flux may be inferred from the prompt muon flux.[1] It has been proposed to measure the prompt muon

---

[1] Note however that there is also a flux of atmospheric muons from short-lived, unflavored mesons such as the η, ρ, and ω, with no associated prompt neutrinos; in fact, this flux may dominate over that from charm mesons [216].

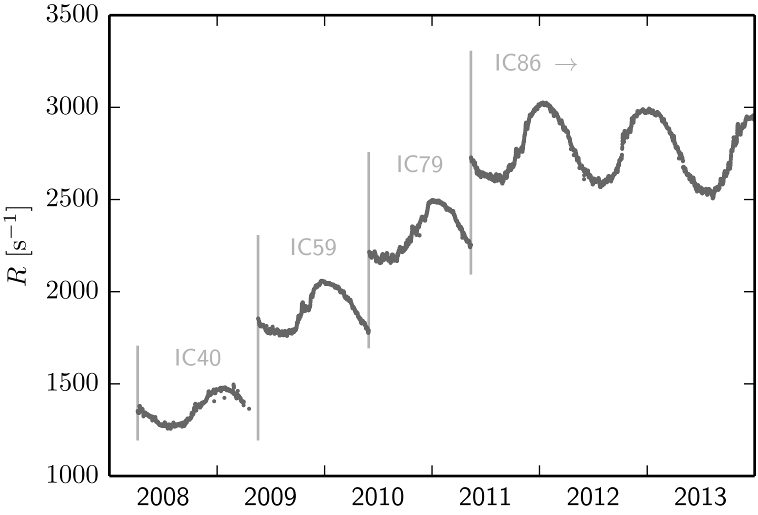

Figure 5.2 — *IceCube Total Trigger Rate.* Trigger rate R of the IceCube detector between April 2008 and December 2013. The different detector configurations (*cf.* section 4.3) are labeled.

(and neutrino) component by observing the seasonal variations of the flux in the $10 - 100\,\text{TeV}$ energy range [217]. Another method is to measure the energy spectrum of single high-energy muons by selecting events that exhibit exceptionally large stochastic energy losses [218]. An attempt at such a measurement has been made with the IceCube detector, however, the results are still inconclusive [219, 220].

In the IceCube detector, penetrating atmospheric muons have three characteristic properties: they can only arrive from directions between the zenith and a few degrees above the horizon, where the ice overburden is not too large; they leave a track signature in the detector; and they are typically detected by optical sensors at the detector boundary first (in contrast to neutrino interactions that occur inside the detection volume). These properties can be exploited to distinguish atmospheric muons from neutrino events (see section 5.3).

It is important to note that the last two properties are less universal than the first: while almost always fulfilled for the majority of muons, which arrive in large bundles with a near-uniform energy loss pattern, single high-energy muons that deposit their energy irregularly may pass the sensors at the detector boundary unnoticed and/or deposit a large fraction of their energy in a single energy loss, appearing as a shower event. Such events can mimic the signature of neutrino interactions and constitute an important background, which is increasingly difficult to reject as the energy (and hence emitted radiation) of the penetrating muon decreases.

5.1.2 Estimating the Background with Simulations

Estimates for the contribution of the penetrating muon background are usually based on Monte-Carlo simulations performed with the air shower simulation code CORSIKA [221], followed by the detector simulation as described in section 4.4. The main difficulty lies in the simulation of a sufficient number of air showers: because such a vast number of muons reach the IceCube detector, also signatures that occur very rarely can appear as a substantial background in searches for neutrino events. Sampling such rare cases often enough requires the production of a number of air showers comparable to the number of naturally occurring showers during the data taking period, which amounts to some 10^{11} showers above 10 TeV per year. A study of the time consumption of muon background simulation, which has led to an optimization of the production settings, is summarized in appendix A.

Furthermore, the outcome of the simulations depends strongly on the assumed elemental composition of the primary cosmic rays (which is not well known for cosmic rays with PeV energies, which are mainly responsible for the penetrating muon background relevant in this work) and on the model that describes their interactions in the atmosphere (which cannot be tested under laboratory conditions at such high energies). A detailed discussion of these difficulties can be found in [222].

For these reasons, estimates of residual atmospheric muon backgrounds in neutrino event samples are often uncertain and fraught with systematic uncertainties. Fortunately, the rejection efficiency usually strongly increases with the muon energy, so that the muon background often becomes negligible at high energies.

In some cases, the background of atmospheric muons can be estimated from the experimental data itself, without relying on air shower simulations [19, 20]. However, such an approach can be taken only for very particular event selection techniques, and simulations are necessary again to obtain *e.g.* the spectral shape of the background.

5.2 Atmospheric Neutrinos

5.2.1 Flux Characteristics

Atmospheric neutrinos are dominantly electron and muon neutrinos.[2] Models for the flux of conventional and prompt atmospheric neutrinos are displayed in fig. 5.3 as a function of the neutrino energy and zenith angle.[3] As discussed at the beginning of this chapter, the prompt flux decreases less strongly with increasing energy than the conventional flux.

While the prompt electron and muon neutrino flux are very similar (and assumed equal in the following), the flux of conventional muon neutrinos is larger than that of conventional electron neutrinos by more than an order of magnitude. This is because kaons, and in particular pions, predominantly decay into muon neutrinos rather than electron neutrinos [51]. As a consequence, the prompt electron neutrino flux surpasses its conventional counterpart at much lower energies than the prompt muon neutrino flux does. This is also evident from fig. 5.4, which shows the fraction of parent particles that contribute to the total flux as a function of the neutrino energy.

Figure 5.3 further shows that the prompt atmospheric neutrino flux, like the primary cosmic-ray flux, is isotropic, whereas the conventional flux is peaked towards the horizon ($\cos\theta = 0$). The cause for this alteration of the conventional flux is the same as for the steeper energy spectrum: pions and kaons are more likely to interact in the atmosphere rather than to decay into neutrinos; the denser the atmosphere, the more so. Pions and kaons that give rise to neutrinos from vertical directions reach denser parts of the atmosphere more quickly, leading to a suppression of the neutrino flux.

---

[2] There is a small flux of prompt atmospheric tau neutrinos from the decay of $\mathrm{D_S}$-mesons. This flux, however, is suppressed with respect to the prompt flux of the other two flavors by a factor of ~ 20 [223], and so is neglected here.

[3] The model of [224] predicts the conventional flux up to 10 TeV. Above this energy, an extrapolation is commonly used, see next section.

Finally, fig. 5.3 illustrates that if a cosmic neutrino flux at the level of the Waxman–Bahcall bound exists, the prompt atmospheric neutrino flux is a sub-dominant component at all energies. The fact that a cosmic flux at approximately this level was detected with the IceCube detector [20] implies that a measurement of the prompt atmospheric neutrino component with IceCube will be challenging.

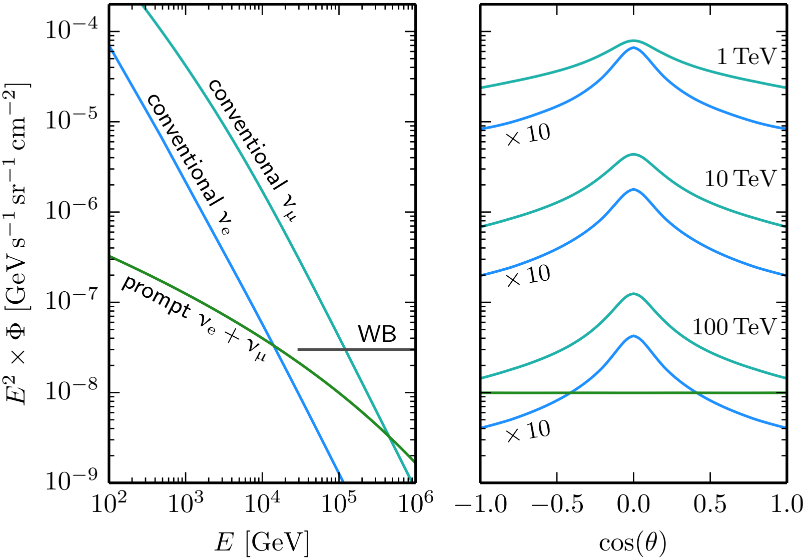

Figure 5.3 — *Atmospheric Neutrino Fluxes.* Fluxes of conventional [224] and prompt [223] atmospheric neutrinos, as a function of the neutrino energy E (left, averaged over all directions) and the zenith angle θ (right, at three different energies). Electron and muon neutrino fluxes are shown separately for conventional neutrinos and combined for prompt neutrinos. In the left plot, a cosmic flux with spectrum $\propto E^{-2}$ at the level of the Waxman–Bahcall bound (*cf.* section 3.1.4) is shown in addition (WB, sum of all flavors). Note that the vertical axis is scaled with E^2 and that the flux of conventional atmospheric ν_e is multiplied by 10 in the right panel for better readability.

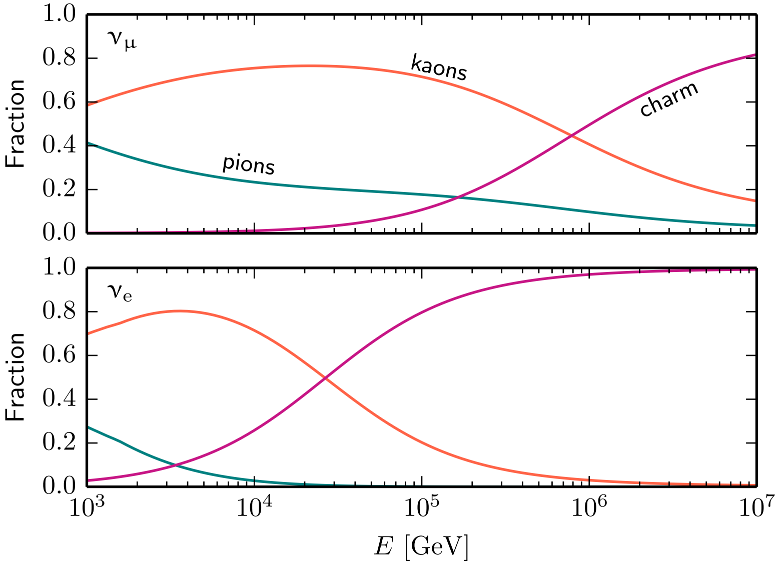

Figure 5.4 — *Parent Particles of Atmospheric Neutrinos.* Fraction of parent particles that contribute to the total atmospheric muon neutrino (top) and electron neutrino (bottom) flux, respectively, as a function of the neutrino energy E. Flux prediction for pions and kaons from [224], for charm mesons from [223].

Contrary to atmospheric muons, atmospheric neutrinos reach the IceCube detector from all directions.[4] Below the horizon, the Earth works as an effective shield against all other particles created in air showers, so that neutrinos from these directions arrive without detectable signs of their origin. Observed individually, such neutrinos hence cannot be distinguished from neutrinos of cosmic origin. On the other hand, neutrinos produced in the atmosphere above the South Pole typically reach the IceCube detector together with muons that were produced in the same air shower. Thus, for downgoing neutrinos, this property may be used to identify atmospheric neutrinos (see section 5.3).

---

[4] Although neutrinos with energies $\gtrsim 10\,\mathrm{TeV}$ that pass through the Earth are attenuated, *cf.* fig. 4.3.

5.2.2 Modeling of the Background

Similar to the case of atmospheric muons, the contribution of atmospheric neutrinos to IceCube event samples is estimated with Monte-Carlo simulations. However, usually no full simulation of atmospheric air showers is carried out.[5] Rather, as described in section 4.4, the neutrino event simulation begins with the injection of neutrinos at the surface of the Earth, and then simulates the propagation and detection in IceCube. Neutrino events simulated with this scheme can be weighted to arbitrary neutrino flux models. Correlations between atmospheric muons and neutrinos are not accounted for in this approach and corrections need to be applied if such correlations play an important role in the event selection (see next section).

The left panel of fig. 5.5 shows two model calculations for the flux of conventional atmospheric neutrinos. In this work, the HKKMS model by Honda *et al.* [224] is used. As the calculation predicts the flux only up to 10 TeV, an extrapolation must be used at higher energies; the extrapolation described in [225, section 5.1.2] is used here. Moreover, the HKKMS model is based on a parametrization of the primary cosmic-ray flux from [226], which does not agree well with recent measurements of the cosmic-ray energy spectrum. Therefore, a correction as described in [23] is applied, adjusting the model such that it conforms with the more recent cosmic-ray flux parametrization from [214] (referred to as H3a model). The dotted line in the left panel of fig. 5.5 shows the HKKMS model with this correction applied.

The right panel of fig. 5.5 shows a selection of model calculations for the prompt atmospheric neutrino flux. Evidently, the variation between the predictions is much larger than in the case of conventional atmospheric neutrinos. This is mainly due to uncertainties in computations of the charm production in hadronic interactions [227]. The ERS model by Enberg *et al.* [223] is used to predict the contribution of prompt atmospheric neutrinos in this work. Similar to the HKKMS model, the ERS model is based on a cosmic-ray flux parametrization (from [228]) that is not in accordance with recent cosmic-ray measurements. Again, a correction is applied [23] that adjusts the flux to conform with the H3a parametrization [214] (dotted line in the figure).

---

[5] Albeit the simulation software was recently extended to allow for simultaneous simulation of muons and neutrinos from air showers [225, section 5.2.4].

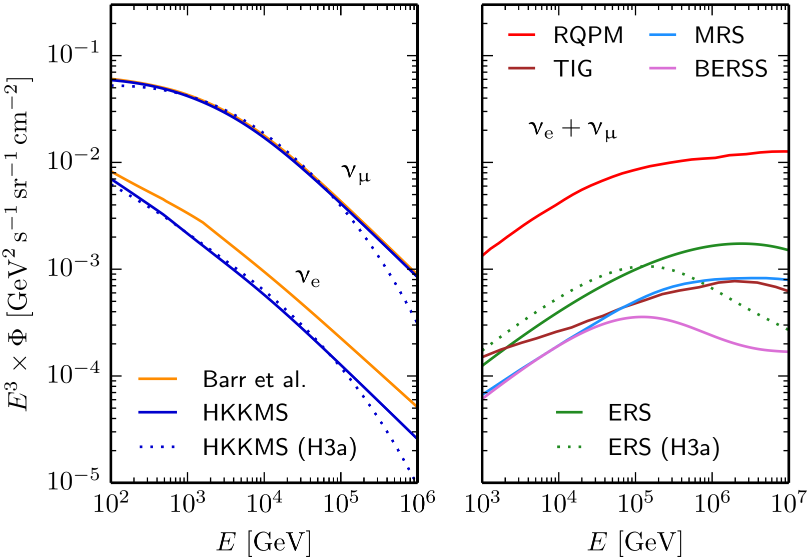

Figure 5.5 — *Comparison of Atmospheric Neutrino Flux Models.* Atmospheric neutrino flux predictions, averaged over all directions and scaled with E^3, as a function of the neutrino energy E. Left: Conventional atmospheric electron and muon neutrinos; model by Barr *et al.* [229] and HKKMS model [224]. Right: Sum of prompt atmospheric electron and muon neutrinos; RQPM model [230], MRS model [231], TIG model [228], BERSS model [227], and ERS model [223]. The dotted lines show the HKKMS and ERS model, modified to conform with the H3a cosmic-ray flux model from [214], respectively, as used in this work.

An update of the ERS model was recently presented in [227] (see "BERSS" in the figure). In addition to adopting the H3a cosmic-ray flux parametrization, the model predicts a lower flux compared to the original calculation (even when accounting for the new cosmic-ray flux parametrization). However, the shape of the updated model, i.e. its dependence on energy, agrees well with the modified ERS model (at least up to ~ 1 PeV, above which energy a detector with the size of IceCube is unlikely to detect any atmospheric neutrinos). Because the absolute normalization of the prompt flux is a free parameter in the analysis presented in this work, the modified ERS model can therefore still be used without being in contradiction with the updated model.

5.3 Rejection Techniques

In the process of searching for cosmic neutrino events, the main task is the rejection of the vast atmospheric muon background. The atmospheric neutrino background – consisting, just like the sought-after signal, of neutrinos – is more difficult to reject. In fact, the only telltale characteristic of atmospheric neutrinos is that, provided they are downgoing, they are often accompanied by atmospheric muons. This case is further discussed in section 5.3.3 and section 5.3.4.

As explained in section 5.1.1, there are three characteristics of atmospheric muons that are usually exploited to reject such events: they are downgoing, track-like, and enter the detector from outside. Specific suitable rejection criteria depend on the analysis performed with the respective sample. Here, we are mainly concerned with searches for a diffuse flux of cosmic neutrinos (as opposed to searches that aim to identify individual sources of cosmic neutrinos). For such searches, three general approaches to event selection have been established in the IceCube Collaboration. These approaches are briefly outlined in the following.

5.3.1 Selecting Upgoing Track Events

In the first approach, the property of the muon background to always arrive from above the detector is exploited. Accordingly, searches following this approach accept only events from directions below (or close to) the horizon, and, to ensure a precise directional reconstruction, only track events. The most persistent class of background in this case are atmospheric muon events that are erroneously reconstructed as upgoing; this often happens *e.g.* when two muons from unrelated air showers arrive simultaneously and are recorded as one event. To eliminate such cases, reconstruction quality criteria are applied in addition to the zenith angle criterion. Signs indicative of a well reconstructed event are, for example, good likelihood values of the track reconstruction algorithm, and a large number of hits matching the hypothesis of a through-going relativistic charged particle, so-called *direct hits*. More details on the selection of track events can be found in [22, 23, 207].

Advantages — The prime advantage of this approach is that it is sensitive to neutrino interactions that occur outside the instrumented volume of the IceCube detector: muons created in charged-current interactions of muon neutrinos can reach the detector from distances of several kilometers. This allows for the selection of large samples of atmospheric neutrinos, which are mainly muon neutrinos. Furthermore, thanks to the precision achieved in the directional reconstruction of track events, it is usually possible to reduce the atmospheric muon background to a negligible level even at low energies, so that neutrinos with energies down to a few hundred GeV can be selected.

Disadvantages — Drawbacks of the approach are, by design, its restriction to charged-current interactions of muon neutrinos[6], and to the northern hemisphere. The second point also implies that atmospheric neutrinos cannot be suppressed with respect to cosmic neutrinos, because the Earth effectively filters all other components of atmospheric air showers.

5.3.2 Selecting Shower Events

The second approach is to select shower events, exploiting that atmospheric muons mostly appear as tracks. Various criteria to distinguish between showers and tracks exist, a few examples are given here. For more details, please refer to [24, 25, 207].

Event reconstruction criteria are based on reconstructions of the events, mostly on reconstructions under the hypothesis of a shower event. Some of the reconstruction algorithms return quality parameters that can be used to reject events that do not fit the assumed hypothesis. Other criteria can be constructed *e.g.* from reconstructions of the interaction vertex, performed on two parts of an event, divided in time. Usually, while the two sets of vertex parameters are similar for shower events, they differ for track events, where the muon travels considerable distances.

On the other hand, *shape* criteria distinguish atmospheric muons from neutrino-induced showers by the different topological shapes of their event signatures. For instance, elongated track events can be rejected by requiring a minimum “fill ratio” of hit DOMs in a hypothetical sphere around the hit pattern. Another criterion, treating the DOM hit pattern as a rigid body, is to require the eigenvalues of the tensor of inertia of this body to be approximately equal, as expected for near-spherical objects.

---

[6] Charged-current interactions of tau neutrinos may be detected if a muon is produced in the tau decay; this happens in 17% of all such interactions.

Advantages — The selection of shower events allows the observation of neutrinos from the entire sky as well as all neutrino flavors. Compared to track events, the deposited energy is correlated more strongly with the initial neutrino energy, which increases the sensitivity to spectral features. Furthermore, the conventional atmospheric neutrino background, consisting mostly of muon neutrinos, is usually less prominent, because charged-current interactions of muon neutrinos are suppressed by the event selection.

Disadvantages — The restriction to shower events implies that only neutrinos that interact within the instrumented volume of the IceCube detector can be selected. Hence, the resulting event samples are usually much smaller than those selected with the first approach. Moreover, atmospheric muons can mimic the signature of a neutrino-induced shower event if they deposit a large fraction of their energy in a single, catastrophic energy loss. This can be alleviated by additionally applying veto criteria, as explained in the next section, but usually an irreducible background of atmospheric muon events remains.

5.3.3 Vetoing Atmospheric Muons

In this approach, events whose sequence of recorded pulses exhibits signs of a penetrating muon are rejected. As such, the approach exploits all revealing muon characteristics, in particular that they are typically detected by DOMs at the detector boundary first.

Straightforward veto criteria are to require that neither the DOM which recorded the first signal nor that which recorded the largest signal be positioned on an outer detector string or in the top-most detector layers [24,25]. Another veto that has been implemented is to demand that fewer than three of the first 250 recorded photoelectrons be recorded by DOMs in the outer layer [19,20]. A more complex veto implementation, in which the size of the veto region scales with the total number of recorded photoelectrons, was introduced in [21].

Furthermore, causality criteria can be applied. These criteria reject events with pulses that are causally incompatible with the assumption of a neutrino interaction (*e.g.* arriving too early), but indicative of an incoming atmospheric muon (see *e.g.* [21, 24]).

Advantages — As in the second approach, neutrinos from all directions and of all flavors can be selected. In addition to shower events, starting tracks also pass the event selection. Most notably however, because atmospheric muons and neutrinos are produced jointly in air showers, the approach automatically suppresses the flux of atmospheric neutrinos. This is known as the self-veto effect of atmospheric neutrinos and is quantitatively discussed in the following section.

Disadvantages — Just as the previous approach, veto-based event selections are restricted to neutrino interactions within the instrumented volume of the detector. Furthermore, because the approach entirely relies on penetrating muons to reveal themselves when they enter the detector, it is prone to events in which muons pass unnoticed between two strings, thus faking a neutrino signature. Even though this happens rarely, the large number of atmospheric muons continuously arriving at the detector usually leads to a residual background of atmospheric muon events that rises substantially with decreasing energy.

5.3.4 The Atmospheric Neutrino Self-Veto

The possibility so suppress the atmospheric neutrino background by vetoing the accompanying atmospheric muons was first conceived by Schönert *et al.* [232]. Their calculation was however restricted to the suppression of conventional atmospheric muon neutrinos due to muons created in the same meson decay. While these *correlated* muons are mainly responsible for the self-veto of muon neutrinos, electron neutrinos can only be vetoed by *uncorrelated* muons that are created in a different part of the air shower. The recent calculation of Gaisser *et al.* [233] incorporates both of these cases as well as the self-veto of prompt atmospheric neutrinos. Figure 5.6 shows the modification of the atmospheric neutrino flux for veto-based event selections according to this calculation, assuming that penetrating muons with energies greater than 1 TeV are always rejected.

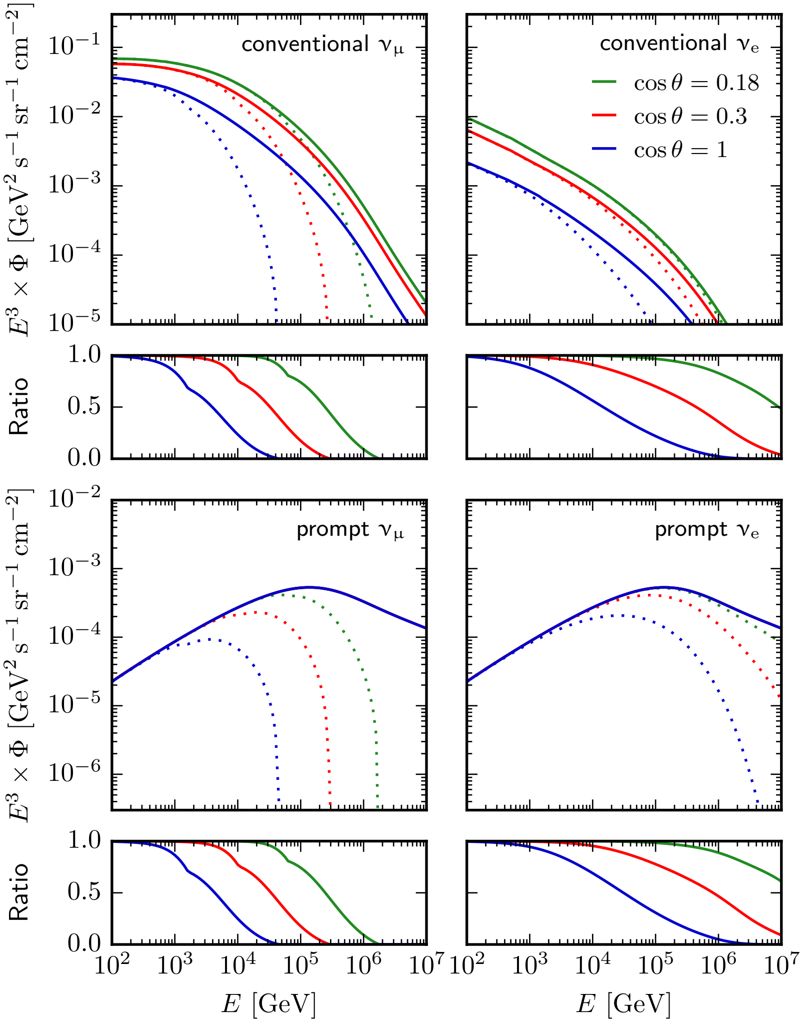

Figure 5.6 — *Atmospheric Neutrino Self-Veto.* Atmospheric neutrino fluxes at three different zenith angles θ, without (solid lines) and with (dotted lines) self-veto effect [233], as a function of the neutrino energy E. Top: Conventional ν_μ (left) and ν_e (right) [224]. Bottom: Prompt ν_μ (left) and ν_e (right) [223]. Both models are modified, *cf.* section 5.2.2.

Chapter 6

Searches for Cosmic Neutrinos with IceCube

> *"If it looks like a duck, and quacks like a duck,*
> *we have at least to consider the possibility that we have a small*
> *aquatic bird of the family Anatidae on our hands."*
>
> — Douglas Adams (1987) [234]

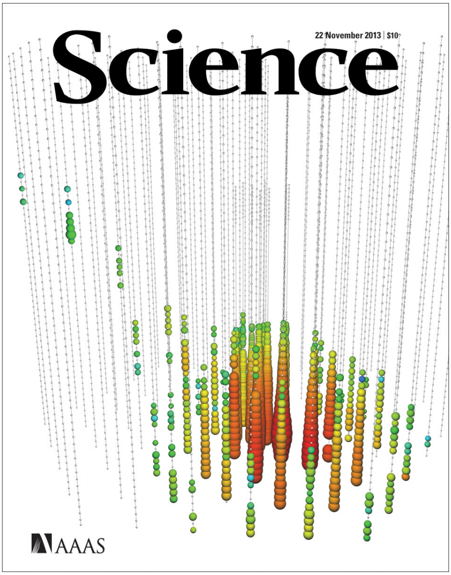

Figure 6.1 — *Cover Page of Science Magazine on November 22, 2013.* The cover page shows an IceCube event view. The issue contained the article in which the IceCube Collaboration presented the first evidence for cosmic neutrinos [19].

Searches for cosmic neutrinos have been carried out with the IceCube Neutrino Telescope since the beginning of its construction. They can be broadly grouped in two categories: those that search for a directional or transient excess over the atmospheric background, and those that search for a diffuse excess that is independent of direction and time. While searches of the first kind will often allow the immediate identification of the source(s) responsible for the excess, they rest upon the premise that the signal of individual sources is strong enough to be detectable. Conversely, searches of the second kind may detect the cumulative signal of many sources even if they are too weak to be detected individually, but leave more room for interpretation of the signal.

The most recent IceCube searches for a directional or transient signal are described in [26–30], none of them has found a significant excess over the background. In this chapter, we will therefore focus on searches for a diffuse flux of cosmic neutrinos. There, first indications for a deviation from the expected atmospheric backgrounds were obtained in searches performed on data taken during the construction phase of IceCube [23–25]. Two shower events with deposited energies of 1.0 PeV and 1.1 PeV, respectively, were then found in a search with the complete detector that was actually targeted at EeV-energy neutrinos [235]. This result triggered a new search that was specifically designed to select neutrino interactions occurring inside the IceCube detector. In two years of data collected with the complete detector, this search found 26 events with deposited energies between 30 TeV and 300 TeV in addition to the two PeV events, thus providing the first solid evidence for a flux of cosmic neutrinos [19] (*cf.* fig. 6.1). Later, the same search performed on a third year of data revealed another 9 events, among them a shower event with a deposited energy of 2 PeV, the highest-energy neutrino interaction observed so far [20].

Further improved searches have then shown that the cosmic neutrino flux extends down to neutrino energies of 25 TeV [21], that it is also visible in the form of muon neutrino-induced tracks from the northern hemisphere [22], and that its flavor composition is compatible with the benchmark $\nu_e : \nu_\mu : \nu_\tau = 1 : 1 : 1$ scenario [36].

This work aims to obtain a comprehensive picture of the cosmic neutrino flux observed by IceCube. To this end, the event samples selected by six of the aforementioned searches [20–25] are combined and analyzed simultaneously.[1] These searches are introduced in more detail in section 6.1. The compilation of a combined event sample is then presented in section 6.2. Hereafter, variables denoted by a prime refer to reconstructed event quantities.

6.1 Searches for a Diffuse Flux of Neutrinos

The searches combined in this work are listed in table 6.1. Based on the signature of the events that they select, they are grouped into searches for shower events (S1, S2), searches for track events (T1, T2), and hybrid event searches that select both types of events (H1, H2). These are described in section 6.1.1, 6.1.2, and 6.1.3, respectively; effective neutrino detection areas and distributions of reconstructed observables are presented in section 6.1.4. A timeline indicating the periods in which the data for the searches were taken is displayed in fig. 6.2.

Table 6.1 — *List of Combined Searches.* The event signatures selected by the searches, the reconstructed observables (see following sections for a description), and the references are listed. The labels are used throughout the following work.

Label	Signature	Observables	References
S1	showers	E'_{dep}	[24, 236]
S2	showers	E'_{dep}	[25, 237]
T1	tracks	$(\mathrm{d}E/\mathrm{d}X)'_{\mu}$, θ'	[23, 238]
T2	tracks	E'_{μ}, θ'	[22, 239]
H1	showers, tracks	E'_{dep}, θ'	[19, 20]
H2	showers, tracks	E'_{dep}, θ', q'_{track}	[21, 225]

6.1.1 Searches for Shower Events

Both searches for shower events were performed on one year of data each, taken with partial configurations of IceCube (*cf.* section 4.3),

---

[1] The event samples selected in [36, 235] have a large overlap with some of those used here, so that the additional information is very limited.

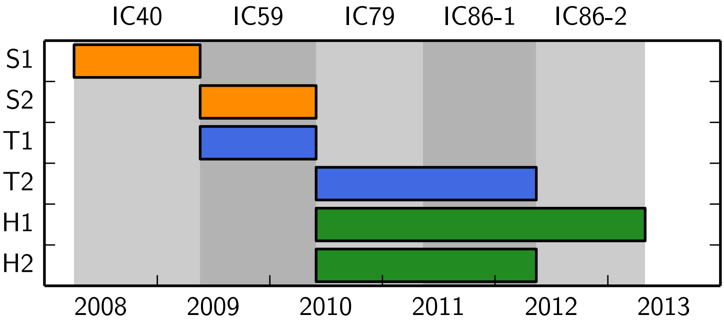

Figure 6.2 — *Data-Taking Periods.* The combined data-taking period begins in April 2008 and ends in May 2013. The gray bands indicate different IceCube detector configurations, as labeled at the top.

namely the IC40 configuration (S1) and the IC59 configuration (S2). Their event selection strategies are very similar and are a combination of shower event selection techniques (section 5.3.2) and veto techniques (section 5.3.3). This combination proved necessary because the partial detector configurations, due to their small size, were particularly susceptible to penetrating muons that leave only little evidence of their identity. Despite their use of veto techniques, neither search originally accounted for the self-veto of atmospheric neutrinos (*cf.* section 5.3.4). For the analysis presented here, the results were corrected for this effect based on the calculation by [233].

The search S1 provides two distinct event samples, S1a and S1b, where less restrictive event quality criteria are imposed for the second sample. The event sample of search S2 was extended to lower energies compared to the one presented in [25]; further details on this extension can be found in appendix B. Both searches cover the entire sky and provide a reconstructed deposited energy E'_{dep} for their event samples. The reconstructions used were not validated with respect to their directional resolution; hence zenith angle data are not available.

The background of atmospheric muons was determined through air shower simulations with the CORSIKA code [221] in both searches. However, in both cases, a reliable estimation could not be obtained at all energies due to limited statistics. Therefore, a parametrization of the muon background as a function of E'_{dep} based on the available simulation data was derived in the course of this work. The parametrization allows the estimation of the muon background also at energies where no simulation data were available.

As a first step, the selection efficiency as a function of the reconstructed deposited energy E'_{dep} was determined using a sample of simulated electron neutrino events. This shower selection efficiency is displayed in fig. 6.3 for all three event samples. Because the signatures of muons and neutrinos cannot be distinguished at the final selection level, the efficiency is valid in good approximation also for the residual muon background.

For each sample, the muon background is then parametrized by a power law, convolved with the selection efficiency. The normalization and spectral index of the power law are determined by a least-square fit to the simulation data of background muons. The result of this procedure is visualized in fig. 6.4. The comparison of the parametrization with the original simulation data in this figure shows that reasonable agreement is achieved with this simple model.

6.1.2 Searches for Track Events

The two searches for track events considered here both follow the event selection techniques described in section 5.3.1. The first one (T1) uses one year of data, taken with the 59-string configuration of IceCube, while the second one (T2) uses two years of data, taken with the 79-string and 86-string configuration of IceCube. The residual background of atmospheric muon events is negligible for both. The events of sample T1 have reconstructed zenith angles $\theta' > 90°$, whereas the event sample of T2 is slightly extended above the horizon, $\theta' > 85°$.

While the event samples of both searches include events with muon energies well below 1 TeV, only the high-energy tail of the spectrum (above a few TeV of muon energy) is used here. This greatly facilitates the treatment of systematic uncertainties, which are particularly difficult to account for in the high-statistics threshold region of track searches, at the expense of a slightly reduced ability to constrain the atmospheric neutrino flux.

The search T1 provides a proxy for the muon energy loss, $(\mathrm{d}E/\mathrm{d}X)'_{\mu}$, whereas T2 provides a muon energy proxy, E'_{μ}. Both searches provide a reconstructed zenith angle, θ', for the respective samples.

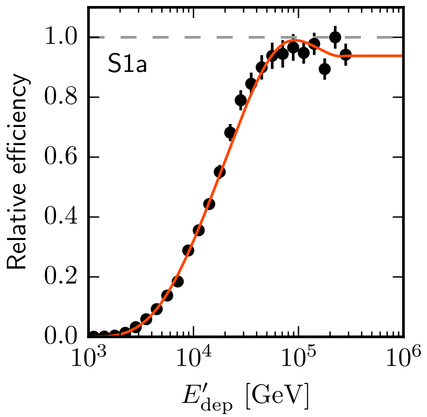

(a) Samples S1a and S1b.

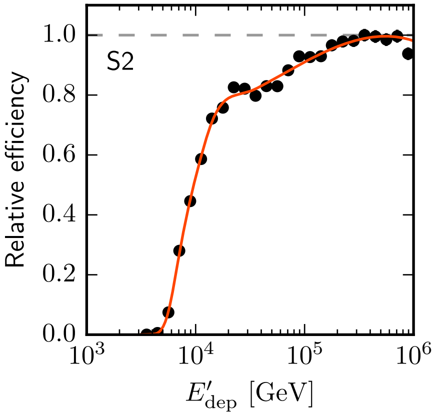

(b) Sample S2.

Figure 6.3 — *Selection Efficiencies for Shower Samples.* The selection efficiency, relative to the maximum efficiency, is shown as a function of the reconstructed deposited energy E'_{dep}. The black points are simulation data, the orange line represents a spline fit through these points.

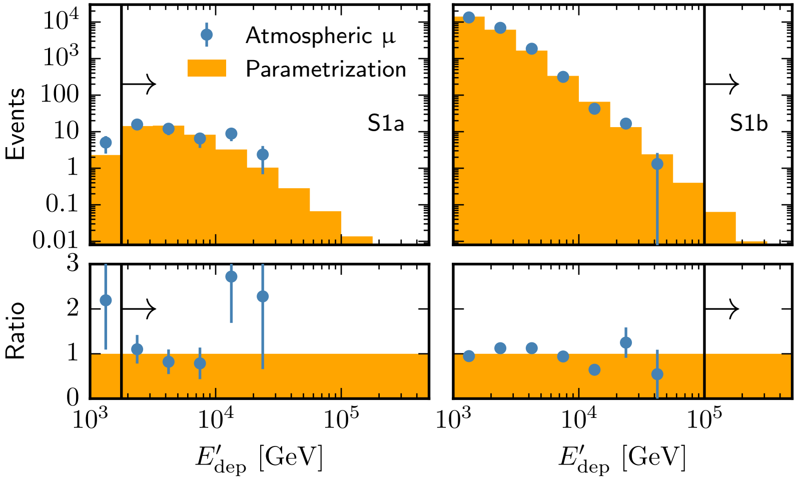

(a) Samples S1a and S1b.

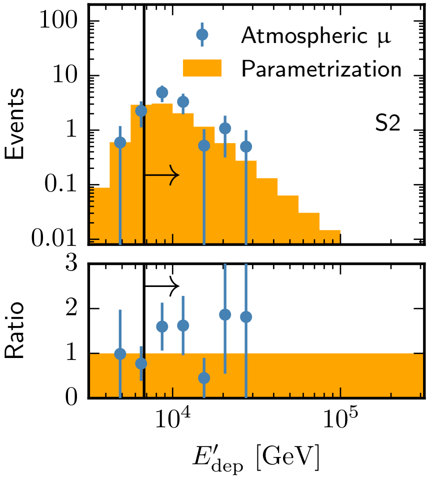

(b) Sample S2.

Figure 6.4 — *Muon Background Parametrization for Shower Samples.* Simulation data and derived parametrization as a function of E'_{dep}. Final fit ranges (*cf.* section 6.2) are indicated by arrows.

6.1.3 Hybrid Event Searches

Both hybrid event searches, H1 and H2, almost entirely rely on the veto techniques described in section 5.3.3 to reject the background of atmospheric muons. As a result, they are able to select shower events as well as track events that start inside the detection volume over the entire sky. The event samples of searches H1 and H2 comprise three and two years of data, respectively, taken with the IC79 and IC86 configuration of IceCube. A residual muon background is present in both event samples. The atmospheric neutrino self-veto effect was implemented in the same way as for the shower searches, based on [233].

To ensure a sufficiently high veto probability, the search H1 requires that more than 6,000 photoelectrons, integrated over all optical modules in an event, be recorded. This criterion results in an energy threshold of $\sim 30\,\mathrm{TeV}$ in deposited energy. The search H2 employs a more complex veto algorithm than H1, thus reducing the energy threshold to $\sim 1\,\mathrm{TeV}$ in deposited energy.

A reconstructed deposited energy E'_{dep} as well as a reconstructed zenith angle θ' is available for the event samples of both searches. In addition, H2 provides a variable, q'_{track}, that denotes the number of photoelectrons that can be causally associated with an outgoing muon track, and thus allows the separation of showers and starting track events. This variable is used to split H2 in two subsamples, one that consists mostly of showers (H2a, $q'_{\mathrm{track}} < 10\,\mathrm{p.e.}$), and one that consists of tracks (H2b, $q'_{\mathrm{track}} > 10\,\mathrm{p.e.}$).

6.1.4 Effective Areas and Observable Distributions

Figure 6.5 shows effective neutrino detection areas for all event samples. The effective neutrino area is the area of a hypothetical ideal detector that detects neutrinos with full efficiency. Given a neutrino flux Φ per unit energy, time, area, and solid angle, it can be used to calculate an expected number of events,

$$N = \int_0^T \mathrm{d}t \int \mathrm{d}\Omega \int \mathrm{d}E \;\; \Phi(E,\theta) \times A_{\mathrm{eff}}(E,\theta)\,, \tag{6.1}$$

where T is the running time of the experiment and $A_{\mathrm{eff}}(E,\theta)$ the effective area as a function of neutrino energy and zenith angle.

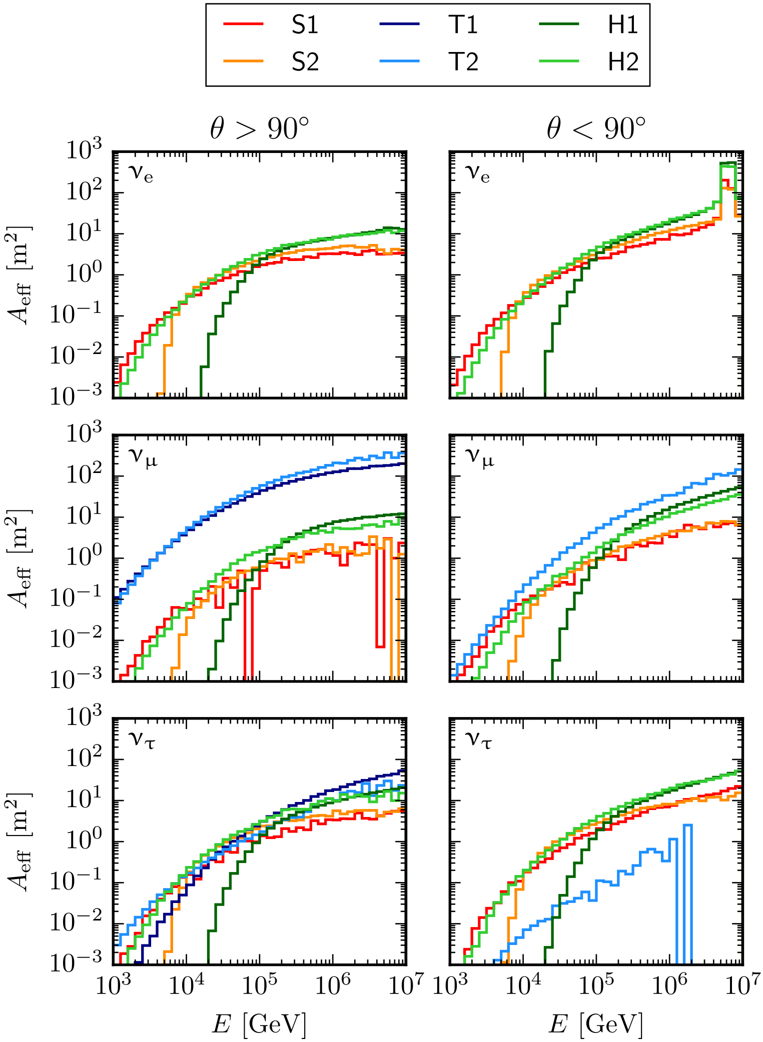

Figure 6.5 — *Comparison of Effective Neutrino Areas.* The effective neutrino area A_{eff} in the northern ($\theta > 90°$, left) and southern ($\theta < 90°$, right) sky is shown for electron (top), muon (center), and tau (bottom) neutrinos, as a function of the neutrino energy E.

Note that while the effective area is a useful quantity to assess the efficiency of an event selection, it does not incorporate the presence of backgrounds, specifically the atmospheric muon background, which can strongly impact the sensitivity. Thus, the sensitivity of an event selection should not be judged from the effective area alone, but should also take the neutrino purity of the sample into account.

Figures 6.6–6.9 show distributions of the experimental data as well as background and signal expectations for the observables of the different samples. The background expectations are derived from simulations, as described in section 5.1 and 5.2. For conventional and prompt atmospheric neutrinos, the simulation is weighted to the models by Honda *et al.* [224] and Enberg *et al.* [223], respectively, where both models were modified to conform with the cosmic-ray composition model from [214] (*cf.* section 5.2.2). The two displayed cosmic neutrino spectra are both power laws,

$$\Phi = 10^{-18}\,\mathrm{GeV}^{-1}\,\mathrm{s}^{-1}\,\mathrm{sr}^{-1}\,\mathrm{cm}^{-2} \times \left(\frac{E}{100\,\mathrm{TeV}}\right)^{-\gamma}, \qquad (6.2)$$

with $\gamma = 2$ and $\gamma = 2.5$, respectively. In both cases, a flavor composition of $\nu_e : \nu_\mu : \nu_\tau = 1 : 1 : 1$ at Earth is assumed.

6.2 Compilation of a Combined Event Sample

The event sample analyzed in this work is a combination of the samples introduced in the previous section. As evident from fig. 6.2, some of the samples have common data taking periods. This can lead to events being present in multiple samples. For the combined analysis presented here, however, it is important that the different event samples are statistically independent, *i.e.* that individual events are not present more than once in the combined sample. It is therefore important to identify the overlap between the samples and remove events that occur more than once, both in simulation and experimental data.

The data for event samples S2 and T1 were both taken with the 59-string configuration of IceCube. However, because S2 consists entirely of showers and T1 entirely of tracks, the event samples are completely independent, *i.e.* no adjustments are necessary. Conversely, the samples T2, H1, and H2, all based on data taken between 2010 and 2012,

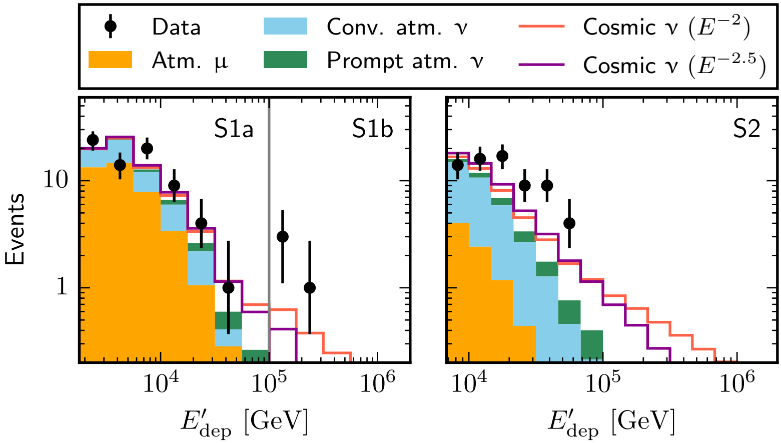

Figure 6.6 — *Default Observable Distributions of Shower Samples.* The background of atmospheric muons and neutrinos is shown as a stacked, filled histogram. Two exemplary cosmic neutrino spectra are displayed in addition, each added onto the background histogram. The distributions show the sum of all neutrino flavors. The error bars on the experimental data are 68% C.L. intervals as defined in [240].

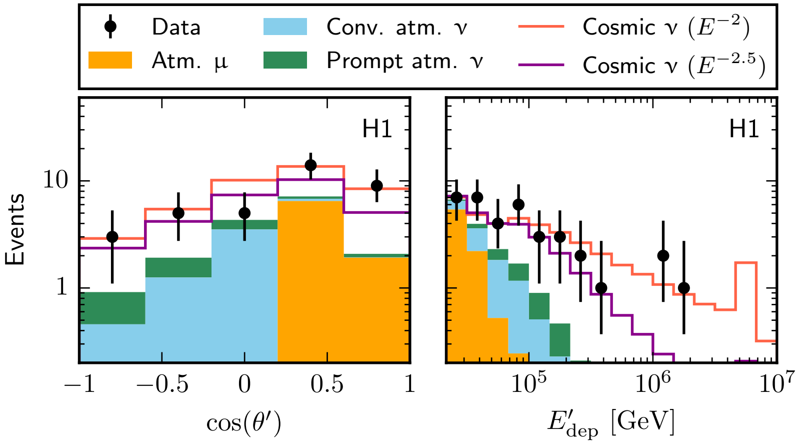

Figure 6.7 — *Default Observable Distributions of Hybrid Sample H1.* See description of fig. 6.6.

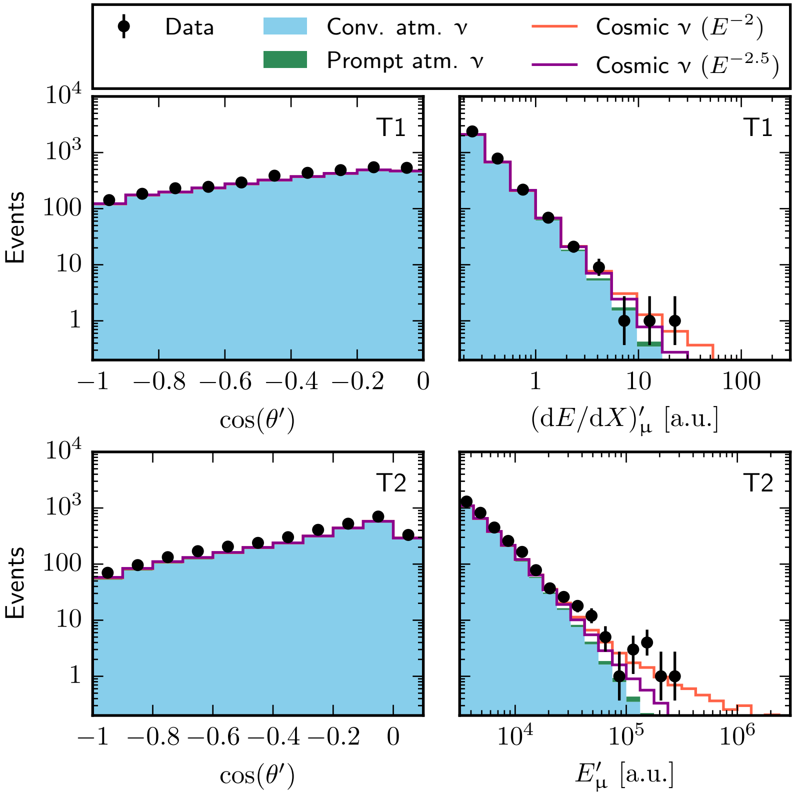

Figure 6.8 — *Default Observable Distributions of Track Samples.* See description of fig. 6.6.

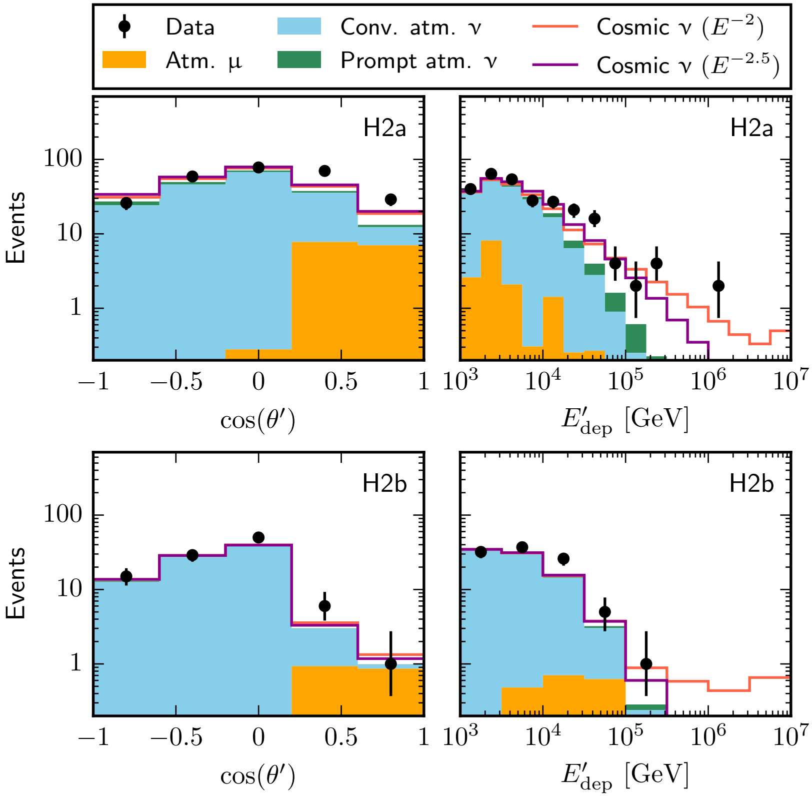

Figure 6.9 — *Default Observable Distributions of Hybrid Sample H2.*
See description of fig. 6.6.

show large overlaps. Specifically, the high-energy part of sample H2 is almost entirely contained in H1, and some tracks in T2 that start inside the detector are also present in H1 and H2.

Because the simulation data provided by the searches are based on different simulation runs, it was not possible to remedy the overlap by simply removing identical events from all but one sample. Instead, additional selection criteria were devised, to ensure that the samples are independent. First, events from sample T2 that start inside the detector were removed by applying the outer-layer veto criterion of samples H1 and H2 in reverse, *i.e.* an early signal was explicitly required in the outer layer of the detector. The fraction of events that are retained in sample T2 is shown in fig. 6.10; a good agreement between simulation and experimental data is observed.

Second, only events in H2 with fewer than 6,000 photoelectrons recorded in total were retained. The events in H1 have more than 6,000 photoelectrons by construction, so that the two samples are independent with this adjustment. The fraction of events retained in H2 is displayed in fig. 6.11. Again, there is good agreement between simulation and experimental data.

The observable distributions of samples T2 and H2 with the above modifications applied are shown in figs. 6.12 and 6.13. Together with the (unmodified) samples S1, S2, T1, and H1, they provide the basis for the likelihood analysis introduced in the following chapter.

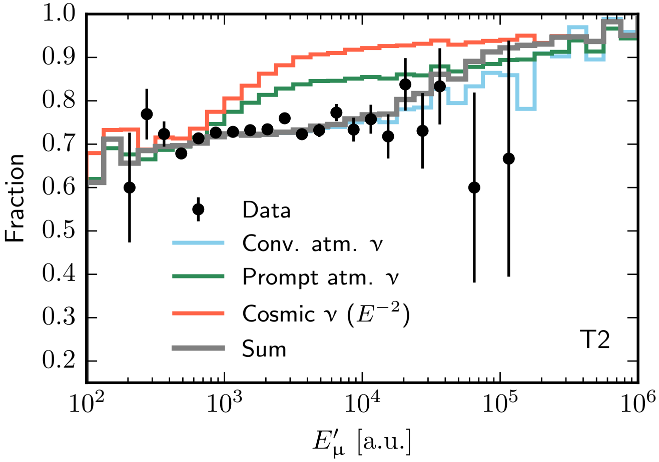

Figure 6.10 — *Fraction of Events Retained in Event Sample* T2*.* Fraction of events in sample T2 with a signal in the veto region, as a function of the muon energy proxy E'_μ.

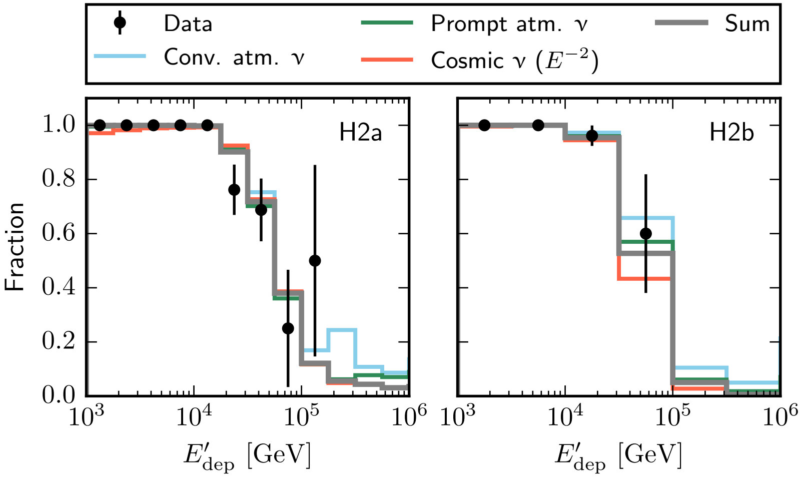

Figure 6.11 — *Fraction of Events Retained in Event Sample* H2*.* Fraction of events in samples H2a and H2b with fewer than 6000 p.e. recorded, as a function of the reconstructed deposited energy E'_{dep}.

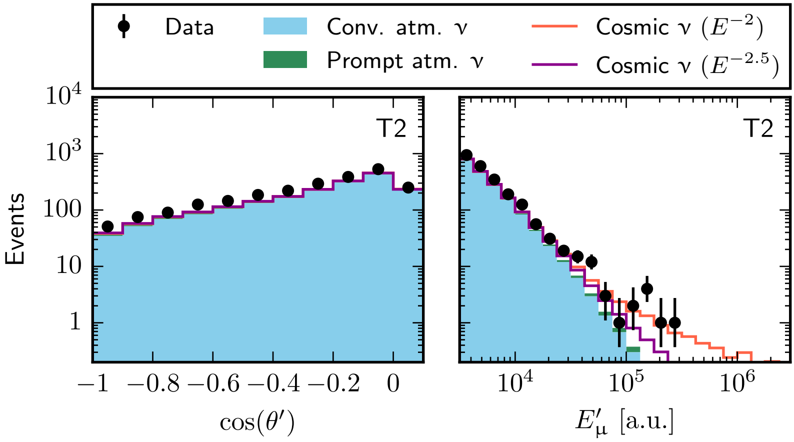

Figure 6.12 — *Modified Observable Distributions of Track Sample T2.* Same as fig. 6.8, but with the modifications to make the event samples statistically independent (*cf.* fig. 6.10).

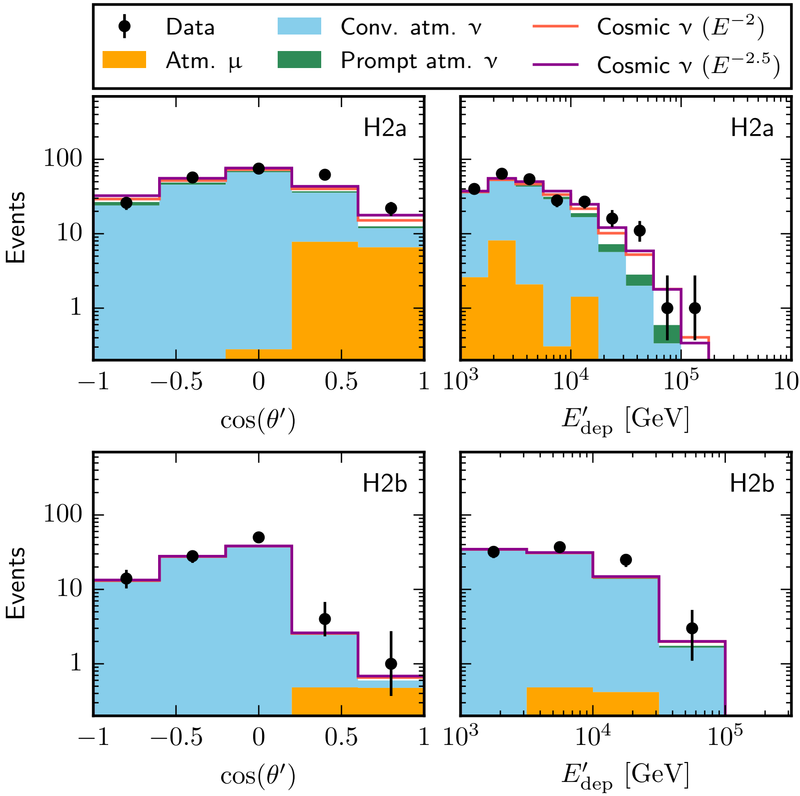

Figure 6.13 — *Modified Observable Distributions of Hybrid Sample H2.* Same as fig. 6.9, but with the modifications to make the event samples statistically independent (*cf.* fig. 6.11).

CHAPTER 7

A Likelihood Analysis on Multiple Event Samples

> *"There is always a well-known solution to every human problem – neat, plausible, and wrong."*
>
> — HENRY LOUIS MENCKEN (1920) [241]

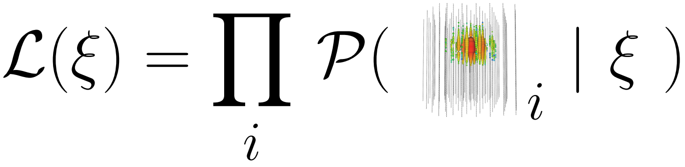
$\mathcal{L}(\xi) = \prod_i \mathcal{P}(\quad _i \mid \xi)$

Figure 7.1 — *Conceptual Principle of the Likelihood Analysis.* The abstract equation shows the conceptional principle of the analysis: The likelihood $\mathcal{L}$ represents the combined probability to observe the experimental data, given a set of model parameter values ξ. Maximizing $\mathcal{L}$ with respect to ξ yields the model parameter values that describe the observed data best.

THE MOTIVATION TO PERFORM a combined analysis of the event samples described in the previous chapter was twofold: to understand whether the different results are in agreement with each other, and to obtain better constraints on the properties of the cosmic neutrino flux by utilizing all information available. The analysis technique is described in this chapter, while the results are presented in chapter 8.

The conceptual principle of the likelihood analysis is illustrated in fig. 7.1. Its aim is to describe the combined experimental data by a set of model distributions that represent the components contributing to the measurement, *i.e.* the background of atmospheric muons and neutrinos, and the cosmic neutrino signal. The expected observations for a specific model are obtained by folding the expected neutrino or muon flux with the detector response (usually determined by simulation). Hence, this concept is sometimes referred to as *forward folding* (as opposed to *unfolding*, where the observed data are transferred into a neutrino flux). The models used in this analysis and the corresponding parameters are described in section 7.1.

The model parameters that yield the best agreement of the model distributions with the experimental data are established by means of a likelihood function, or *test statistic*. The procedure of maximizing the likelihood function with respect to the model parameters is referred to as *fit*. The likelihood method can further be employed to obtain confidence intervals for the parameters, to compare the level of agreement of different models, and to assess the quality of agreement of individual models. This is explained further in section 7.2.

Systematic uncertainties in the models or in the detector description can distort the model distributions, and hence bias the fit result. To avoid this, the impact of systematic effects was parametrized and incorporated in the likelihood method. Parametrizations of the effects relevant for this work are introduced in section 7.3.

Finally, section 7.4 describes data challenges based on pseudo experiments that were performed to test the validity of the method.

7.1 Modeling

The model distributions used in the analysis are obtained through Monte-Carlo simulations, as already described for the background components in section 5.1 and 5.2. One-dimensional projections of baseline (*i.e.* not fitted to the data) distributions of the background components and two exemplary signal fluxes are displayed in figs. 6.6–6.9 and 6.12, 6.13. A binning similar to that shown in the figures is used in the analysis, the exact binning is given in appendix C.

7.1.1 Background Components

The absolute normalization of the conventional (ϕ_{conv}) and prompt (ϕ_{prompt}) atmospheric neutrino background are free model parameters in the fit procedure, reflecting the theoretical uncertainties associated with these components. They specify the normalization in units of the default model normalization and affect the model distributions of all event samples the same. Variations of the spectral index of the primary cosmic-ray spectrum, which is implemented as a systematic uncertainty (see section 7.3), can change both components further.

The normalization of the muon background is also determined in the fit; the details are described in section 7.3.

7.1.2 Cosmic Neutrino Component

Because no source of cosmic high-energy neutrinos has been identified so far, only general assumptions about the nature of a cosmic neutrino flux can be made. Various models for the cosmic neutrino component are tested in this analysis, as outlined in the following and summarized in table 7.1. All models assume a flux of neutrinos constant in time.

Spectral Models

In all spectral models, the cosmic neutrino flux is assumed to arrive at Earth isotropically and to consist of all three flavors in equal parts (*i.e.* $\nu_e : \nu_\mu : \nu_\tau = 1 : 1 : 1$, *cf.* section 3.1.3).

The simplest model is the *power law* model,

$$\Phi(E) \equiv \frac{\mathrm{d}N}{\mathrm{d}E\,\mathrm{d}t\,\mathrm{d}\Omega\,\mathrm{d}A} = \phi \times \left(\frac{E}{100\,\mathrm{TeV}}\right)^{-\gamma}, \tag{7.1}$$

where Φ denotes the all-flavor neutrino flux per energy interval, time, solid angle, and area, ϕ its normalization at 100 TeV, and γ its spectral index. Both ϕ and γ are free parameters in the the likelihood analysis.

In the *power law + cut-off* model, the flux at high energies is suppressed ("cut off") by an additional factor of $\exp(-E/E_{\mathrm{cut}})$, where E_{cut} is a free parameter. Sources that accelerate cosmic rays only up to a certain energy could produce a neutrino flux that can be approximated by such a spectral shape.

The *two power laws* model describes the flux as the sum of two power laws, Φ_1 and Φ_2, with parameters ϕ_1, γ_1, ϕ_2, and γ_2. This spectral behavior could be the result of a superposition of the flux from two distinct classes of sources.

Finally, the *differential* model allows for more general spectral deviations. It describes the cosmic neutrino flux with nine independent basis functions, defined in nine logarithmically spaced energy intervals between 10 TeV and 10 PeV. The normalizations $\phi_1 - \phi_9$ of the basis functions are free parameters, while the energy spectrum in each interval is assumed to be proportional to E^{-2}. This model is inspired by a similar procedure carried out in [20, 21], and bears resemblance with unfolding techniques as used *e.g.* in [89].

North-South Model

A simple test concerning the isotropy of the cosmic neutrino flux can be made with the *north-south* model. Here, the cosmic neutrino component consists of two independent neutrino fluxes, one entirely from the northern and one entirely from the southern hemisphere (separated at declination $\delta = 0°$ / zenith angle $\theta = 90°$). Both are assumed to follow a power law as defined in eq. 7.1, with free parameters ϕ_{N}, γ_{N}, ϕ_{S}, and γ_{S}, and a flavor composition as for the spectral models. The model also acts as a test for unconsidered detector-related systematic effects that affect the two hemispheres differently.

Although generally of interest, more complex anisotropic models would require the use of right-ascension information, which, having been selected for diffuse searches, the event samples combined here do not contain.[1] They are thus not carried out here. Note however that the north-south model could be sensitive to certain anisotropic scenarios, like *e.g.* a flux of neutrinos from the inner part of the Milky Way, which is located in the southern hemisphere.

---

[1] This information is usually removed for searches of a diffuse flux, to avoid experimenter's bias for future point-source searches.

Flavor Models

The assumptions about the flavor composition are weakened in the flavor models, while the assumption of isotropy is restored. It is furthermore assumed that each flavor component of the flux has the same energy spectrum, *i.e.* a power law with spectral index γ as defined in eq. 7.1. The flux normalization for neutrino flavor α is denoted by ϕ_α.

In the *2-flavor* model, the flux of ν_μ and ν_τ are still assumed to be equal at Earth (with combined normalization $\phi_{\mu+\tau}$), while the ν_e flux is allowed to deviate. The relation $\phi_\mu = \phi_\tau$ is, in good approximation, true for any flavor composition at the source, provided that standard neutrino oscillations (as introduced in section 2.1.3) transform the neutrino flux during propagation.[2] The model thus allows a measurement of the flavor composition at Earth under this constraint.

More generally, no assumptions about the flavor composition are made in the *3-flavor* model, allowing one to obtain the flavor composition at Earth that is favored by the experimental data, and to test for non-standard neutrino oscillation scenarios.

Table 7.1 — *Models for the Cosmic Neutrino Flux.* The second column indicates whether an isotropic flux is assumed; the third column lists assumptions about the flavor composition of the flux. The last column gives the free parameters of the model.

Model	Isotropy	Flavor	Parameters
power law	yes	$\phi_e = \phi_\mu = \phi_\tau$	ϕ, γ
power law + cut-off	yes	$\phi_e = \phi_\mu = \phi_\tau$	ϕ, γ, E_{cut}
two power laws	yes	$\phi_e = \phi_\mu = \phi_\tau$	ϕ_1, γ_1, ϕ_2, γ_2
differential	yes	$\phi_e = \phi_\mu = \phi_\tau$	$\phi_1, \ldots, \phi_9$
north-south	no	$\phi_e = \phi_\mu = \phi_\tau$	ϕ_N, γ_N, ϕ_S, γ_S
2-flavor	yes	$\phi_\mu = \phi_\tau$	ϕ_e, $\phi_{\mu+\tau}$, γ
3-flavor	yes	–	ϕ_e, ϕ_μ, ϕ_τ, γ

---

[2] Deviations up to 20% can occur, depending on the exact values of the oscillation parameters.

7.2 Likelihood Method

7.2.1 Test Statistic

The *test statistic* measures the level of agreement between the experimental data and the model distributions, which are both binned in the available observables (*cf.* table 6.1 and appendix C). To derive it, we first compute

$$\mathcal{L}(\xi) = \prod_{i=1}^{N} \mathcal{P}(n_i \,|\, \nu_i(\xi))\,, \tag{7.2}$$

where

$$\mathcal{P}(n_i \,|\, \nu_i(\xi)) = \frac{\nu_i^{n_i}(\xi)}{n_i!} \times \exp(-\nu_i(\xi)) \tag{7.3}$$

is the Poisson probability to observe n_i events in bin i, given the combined prediction $\nu_i(\xi)$ of the model distributions in this bin for the set of parameter values ξ. $\mathcal{L}(\xi)$ is thus the likelihood to observe the combined experimental data in all N bins, given the model prediction based on ξ. The test statistic is then defined as

$$-\ln \mathcal{L}(\xi) = -\sum_{i=1}^{N} \ln \left(\frac{\nu_i^{n_i}(\xi)}{n_i!} \times \exp(-\nu_i(\xi)) \right)\,. \tag{7.4}$$

Minimizing $-\ln \mathcal{L}$ with respect to ξ maximizes $\mathcal{L}$, and thus yields the parameter values that describe the observed data best. The usage of the negative logarithm is a measure to ease the optimization process, which is performed numerically.

Some parameters of the model are not of primary interest to the analysis, such as parameters that model the effect of systematic uncertainties. These are usually referred to as *nuisance parameters*. Often, prior knowledge about the values that these parameters can take exists. In this case, an additional penalty term can be multiplied to the likelihood function for each nuisance parameter η. The term is known as *prior* and penalizes deviations from the default central value η^*. Here, a Gaussian-shaped penalty term with width σ is used. With m nuisance parameters included, eq. 7.4 reads

$$-\ln \mathcal{L} = -\sum_{i=1}^{N} \ln \left(\frac{\nu_i^{n_i}}{n_i!} \times \exp(-\nu_i) \right) + \sum_{j=1}^{m} \frac{(\eta_j - \eta_j^*)^2}{2(\sigma_j)^2}\,. \tag{7.5}$$

7.2.2 Pseudo Experiments

For various purposes, it can be helpful to generate *pseudo experiments*, consisting of artificial data, for a particular set of model parameter values. This can for instance be achieved by randomly drawing, for each bin, from a Poisson distribution with mean equal to the model prediction for that bin. Performing this many times yields an *ensemble* of pseudo experiments, which can then be studied for its statistical properties.

The so-called *Asimov data set* [242] represents another useful pseudo experiment. Given a set of model parameter values, it is defined as the data set for which the minimization of eq. 7.5 exactly returns these input parameter values. In our case, the Asimov data set is simply given by the combined prediction of the model distributions in each bin. Cowan *et al.* [242] have shown that this data set can be seen as a representative one for the assumed model parameter values, and that it can be used to estimate the expected sensitivity of the experiment.[3]

7.2.3 Likelihood Ratio Tests

A likelihood ratio test ranks two models M1 and M2 with respect to their agreement with the observed data.[4] The corresponding test statistic is defined as

$$-2\,\Delta\ln\mathcal{L} = -2\,\ln\left(\mathcal{L}_{\mathrm{M1}}/\mathcal{L}_{\mathrm{M2}}\right)\,, \tag{7.6}$$

where $\mathcal{L}_{\mathrm{M1}}$ and $\mathcal{L}_{\mathrm{M2}}$ are maximized separately. If the sample size is sufficiently large and no parameter value is close to a physical bound, this quantity is χ^2-distributed with k degrees of freedom, where k is the difference in the number of parameters between M2 and M1 [51, 244]. The likelihood ratio test p-value, which denotes the probability to observe a value of $-2\,\Delta\ln\mathcal{L}$ larger than that obtained with the experimental data, provided model M1 is true, can then be computed analytically.

---

[3] The Asimov data set is named after the writer Isaac Asimov. In his short story "Franchise" [243], elections are held by selecting a single, representative voter that replaces the entire electorate.

[4] One restriction is that the two models must be nested, *i.e.* the parameter space of model M1 must be a subset of that of M2.

If either of the above conditions is not fulfilled, the distribution of $-2\,\Delta\ln\mathcal{L}$ can deviate from a χ^2-distribution. In this case, the exact distribution can still be computed from an ensemble of pseudo experiments, generated from the best-fit parameter values of model M1. The p-value is then given by the percentage of pseudo experiments that lead to a larger value of $-2\,\Delta\ln\mathcal{L}$ than observed with the experimental data. All likelihood ratio test p-values quoted in this work were obtained with this procedure.

Obtaining Confidence Intervals

Likelihood ratio tests can also be employed to obtain confidence intervals for the model parameters. To this effect, the parameter of interest is constrained to a particular value, and a likelihood ratio test with respect to the model without this constraint is carried out. Performing this for a series of values is known as a *profile likelihood scan* [51]. In the approximation that $-2\,\Delta\ln\mathcal{L}$ is χ^2-distributed, the confidence intervals are then obtained by determining the parameter values for which $-2\,\Delta\ln\mathcal{L}$ equals a certain value, which depends on the desired confidence level; values for four different confidence levels are given in table 7.2. The approximation was verified and is used to obtain the confidence intervals quoted in this work.

In a similar way, 2-dimensional profile likelihood scans are performed by constraining two parameters simultaneously. The corresponding values of $-2\,\Delta\ln\mathcal{L}$ that define the 2-dimensional confidence regions are also listed in table 7.2.

Table 7.2 — *Definition of Confidence Intervals.* Listed are the values of $-2\,\Delta\ln\mathcal{L}$ that define one- and two-dimensional confidence intervals in the χ^2-approximation for various confidence levels.

Confidence Level	1D	2D
68%	1	2.3
90%	2.71	4.61
95%	3.84	5.99
99%	6.63	9.21

Goodness-of-fit Tests

Finally, a likelihood ratio test can also be used to assess the fit quality of a single model. The test statistic for this goodness-of-fit test is defined as

$$-2\,\Delta\ln\mathcal{L} = -2\,\ln\left(\mathcal{L}/\mathcal{L}_{\mathrm{sat}}\right)\,, \tag{7.7}$$

where $\mathcal{L}_{\mathrm{sat}}$ is the likelihood of the "saturated" model that exactly predicts the observed outcome (i.e. $\nu_i = n_i$ in eq. 7.4). In analogy to the likelihood ratio test p-value, the goodness-of-fit p-value denotes the probability to observe a value of $-2\,\Delta\ln\mathcal{L}$ larger than that obtained with the experimental data, provided the tested model is true. As before, the distribution of the test statistic is computed from an ensemble of pseudo experiments.[5]

7.2.4 Construction of a Credible Energy Interval

Many of the models for the cosmic neutrino flux introduced in section 7.1.2 describe a flux that is not bounded in energy. In practice, the experimental data provide evidence for a cosmic neutrino flux only in a limited energy range. Data outside this interval do not contribute to the evidence, either because the background is too large or because the flux is too low.

To compute this *credible energy interval*, the following procedure was devised: The model distributions are modified at the lower and upper end by successively removing simulated events, ordered in energy. The fit is repeated at each step, with the parameters of the flux component under investigation held fixed. The bounds of the credible energy interval are defined by the energies at which the test statistic rises by $-2\,\Delta\ln\mathcal{L} = 1$ with respect to the fit with the unmodified model distributions.

7.3 Systematic Uncertainties

This section describes the systematic effects that were investigated as part of the presented analysis. Those that were found to impact the results were parametrized and incorporated as nuisance parameters, as outlined in the following.

---

[5] Note that although seemingly intuitive, carrying out this procedure with the regular test statistic (eq. 7.5) does not yield a meaningful goodness-of-fit p-value [245].

7.3.1 Energy Calibration Scale

The energy calibration scale is arguably the most important systematic uncertainty that needs to be considered. A shift of this scale would distort the relation between reconstructed energy observables and the true neutrino energy, and thus affect the model distributions. It could be the result of several systematic effects, such as an uncertainty in the optical efficiency of the detector modules or an imperfect model of the scattering and absorption in the South Pole ice. Because the knowledge about these effects has evolved with time, they were not treated consistently in the simulation of the event samples that enter this analysis (*e.g.* different models of the ice were used). Here, the attempt is to account for them by a generic variation of the energy calibration scale that is independent for each of the event samples, with corresponding parameters $\phi_{E,\mathsf{S1}}$, $\phi_{E,\mathsf{S2}}$, $\phi_{E,\mathsf{T1}}$, $\phi_{E,\mathsf{T2}}$, $\phi_{E,\mathsf{H1}}$, and $\phi_{E,\mathsf{H2}}$. For each parameter, $\phi_E = 1$ corresponds to the baseline value, and the width of the prior is 15%. The details of the implementation are outlined below.

Shower and Hybrid Event Samples

The energy observable used for the shower and hybrid event samples (S1, S2, H1, and H2) is the reconstructed deposited energy, E'_{dep}. To first order, this quantity scales linearly with the energy calibration scale. The variation of the energy scale ϕ_E is hence implemented as a scaling of the model distributions from E'_{dep} to $\phi_E \times E'_{\mathrm{dep}}$.

In practice, this is achieved by fitting a spline function to the cumulative distribution of E'_{dep} and evaluating this spline function at E'_{dep} and $\phi_E \times E'_{\mathrm{dep}}$ to determine the number of events that migrate from one bin to the next. This procedure is carried out after all other fit parameters have already been applied. Figure 7.2 shows a few exemplary spline functions that were obtained for event sample H1.

Having applied the scaling, it is important to account for the event selection efficiency, which changes as a function of E'_{dep}. The event selection efficiencies that were obtained for samples S1 and S2 have al-

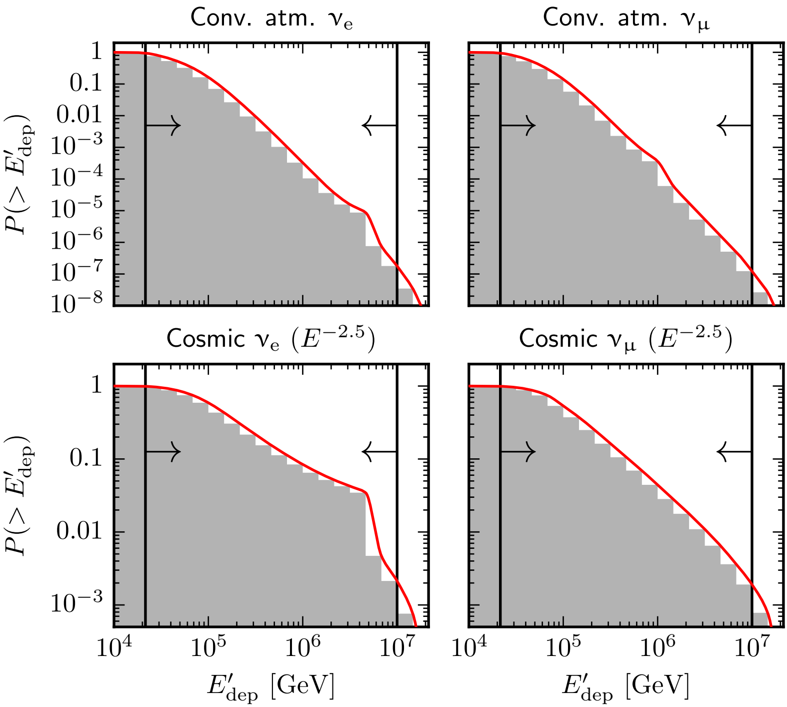

Figure 7.2 — *Illustration of the Energy Calibration Scale Implementation for Shower and Hybrid Samples.* Event sample H1 is used as an example. The gray histogram represents the inverse cumulative model distribution of E'_{dep} for conventional ν_e and ν_μ (top) and cosmic ν_e and ν_μ (bottom). The red line shows a spline function fitted to the distribution. The black arrows indicate the range used in the analysis.

ready been shown in fig. 6.3. The efficiency for sample H1 was obtained in the same way and is displayed in the left panel of fig. 7.3. Finally, the efficiency for sample H2, shown in the right panel of fig. 7.3, was provided by [246], and modified to account for the modifications made to the sample in the course of this work (*cf.* section 6.2). The scaled distributions are corrected for the varying selection efficiency based on these curves.

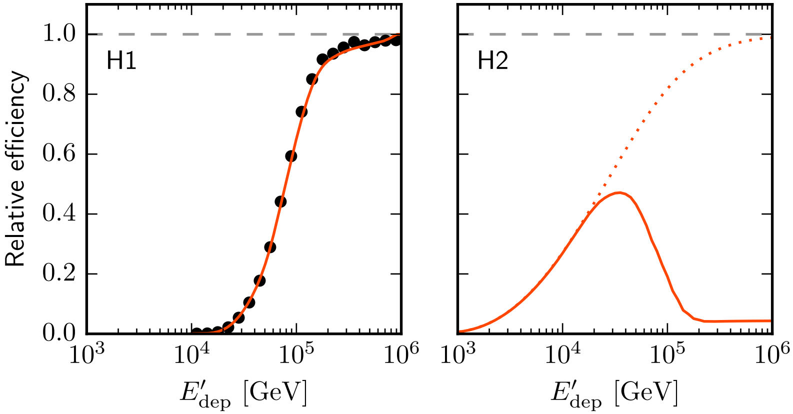

Figure 7.3 — *Selection Efficiencies for Hybrid Samples.* Relative event selection efficiency for samples H1 (left) and H2 (right), as a function of the deposited energy E'_{dep}. In the left plot, the black points are simulation data, and the orange line represents a spline fit through these points. The dashed curve in the right plot was provided by [246]. The solid curve takes into account the modifications that were applied to make the samples statistically independent, as described in section 6.2.

Track Event Samples

A slightly different approach to implement the energy calibration scale was taken for the track samples T1 and T2. Here, simulation data with different optical efficiencies of the optical modules were available. These simulation data were used to obtain a parametrization for the energy calibration scale.

An example of the procedure, based on sample T2, is displayed in fig. 7.4. A correction factor was obtained by interpolating between the different simulation data sets. Because only the high-energy tail of the distributions is used here (*cf.* section 6.1.2), this correction factor can be modeled independently of the energy observable (E'_{μ} in this example) in good approximation, see the left panel. The correction factor depends on the shape of the distribution however, and is thus different for each component of the flux, as shown in the right panel. Correction factors for sample T1 were obtained by the same procedure.

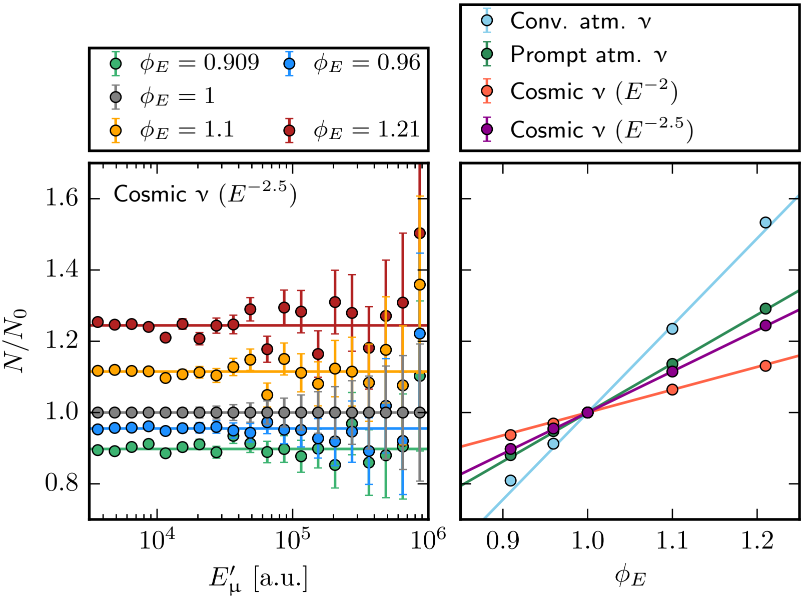

Figure 7.4 — *Illustration of the Energy Calibration Scale Implementation for Track Samples.* Event sample T2 is used as an example. Left: Number of events per bin in simulation sets with varied optical efficiencies, relative to the number of events in the default simulation set, for simulated cosmic neutrinos (with spectrum $E^{-2.5}$). The optical efficiencies are specified relative to the default efficiency. The lines represent fits of a constant to the simulation data. Right: Constants fitted to the simulation data as illustrated in the left panel for various components of the neutrino flux, as a function of the optical efficiency used in the simulation. The points represent the different simulation data sets, the lines show an interpolation between these sets.

7.3.2 Spectral Index of the Primary Cosmic-Ray Flux

Because atmospheric neutrinos are produced by cosmic rays impinging on the atmosphere, their energy spectrum directly depends on the cosmic-ray energy spectrum. Hence, the uncertainty on the spectral index of the primary cosmic-ray flux is implemented as a nuisance parameter that tilts the spectrum of atmospheric neutrinos by $\Delta\gamma_{\mathrm{cr}}$ relative to the default model. Note that positive values of $\Delta\gamma_{\mathrm{cr}}$ correspond to a steeper spectrum. A width of 0.05 is used for the prior (*cf.* [247]).

7.3.3 Normalization of the Muon Background

A tailored estimation of the residual muon background was obtained for the event samples S1, S2, H1, and H2. Due to the different methods used, the uncertainties of the estimates are largely uncorrelated. In all cases, the dominant uncertainty is the absolute normalization. Therefore, a nuisance parameter that varies the normalization of the residual muon background was implemented for each of the mentioned samples ($\phi_{\mu,\mathsf{S1}}$, $\phi_{\mu,\mathsf{S2}}$, $\phi_{\mu,\mathsf{H1}}$, and $\phi_{\mu,\mathsf{H2}}$). These parameters can vary independently, and are each constrained by a prior of width 50%.

7.3.4 Atmospheric Pion-to-Kaon Ratio

A mis-modeling of the pion-to-kaon ratio in atmospheric air showers could result in a deviation of the conventional atmospheric electron-to-muon neutrino ratio from the model prediction. Hence, the impact on the fit results of a realistic deviation of this ratio was determined. The impact on the parameters of the cosmic neutrino flux was found to be negligible, hence, the atmospheric pion-to-kaon ratio is not treated in the form of a nuisance parameter in the likelihood analysis.

7.4 Data Challenges

The likelihood method outlined in this chapter was verified through various data challenges, *i.e.* with pseudo experiments based on known model parameter values. This section presents a selection of these checks, which also act as estimates for the sensitivity of the analysis.

Two exemplary cosmic neutrino flux models are used, both based on the *power law* model introduced in section 7.1.2. They are defined by the following parameter values (see eq. 7.1):

$$(1) \qquad \phi = 3 \times 10^{-18}\,\mathrm{GeV}^{-1}\,\mathrm{s}^{-1}\,\mathrm{sr}^{-1}\,\mathrm{cm}^{-2}, \qquad \gamma = 2\ ;$$

$$(2) \qquad \phi = 6 \times 10^{-18}\,\mathrm{GeV}^{-1}\,\mathrm{s}^{-1}\,\mathrm{sr}^{-1}\,\mathrm{cm}^{-2}, \qquad \gamma = 2.5\ .$$

7.4.1 Energy Spectrum

First, the ability to recover the flux parameters ϕ and γ is tested. The results are shown in fig. 7.5 and 7.6 for the two test fluxes, respectively.

The distribution of the parameter values obtained from the 2,000 pseudo experiments show that the input parameter values can be recovered on average. The contours obtained from the Asimov data set illustrate the expected sensitivity of the analysis to the assumed test flux.

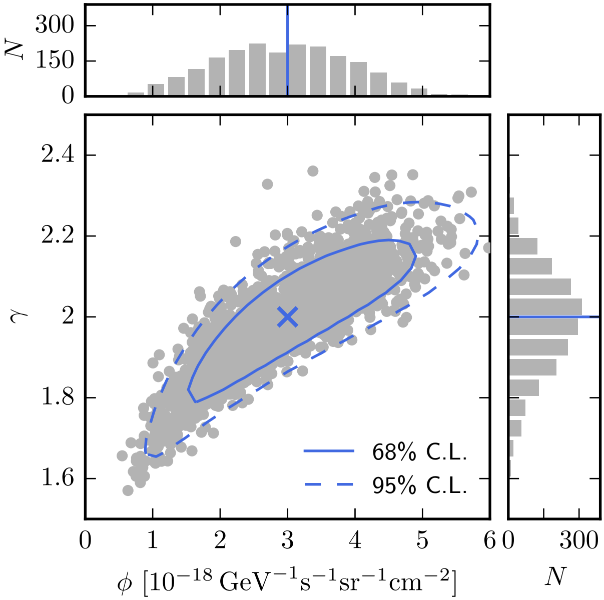

Figure 7.5 — *Energy Spectrum Data Challenge: Test Flux (1).*
Flux parameters ϕ and γ recovered by the likelihood analysis. The blue cross marks the input parameter values. The blue lines represent the 68% and 95% confidence level contours obtained from the Asimov data set. Results of 2,000 random pseudo experiments are shown as gray dots; the small panels at the sides show projected histograms.

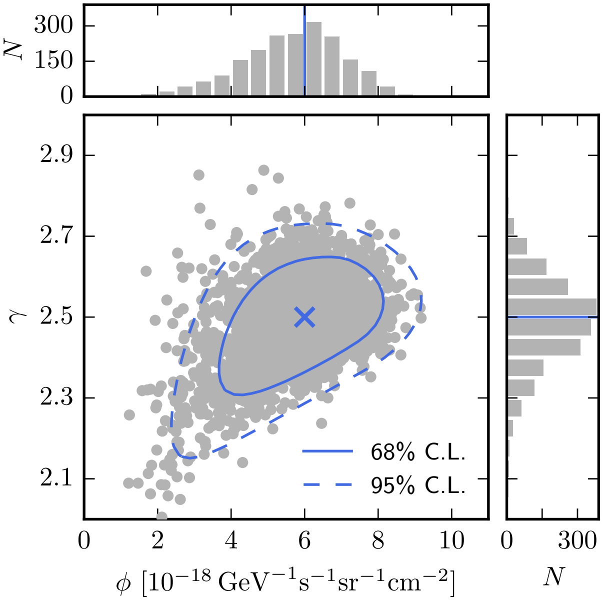

Figure 7.6 — *Energy Spectrum Data Challenge: Test Flux (2).*
See description of fig. 7.5.

A data challenge for the calculation of a credible energy interval is shown in fig. 7.7. As can be expected, the credible energy interval for the hard test flux (1) covers higher energies than the credible energy interval for the softer test flux (2), on average. Note however that the bounds of the interval can vary strongly depending on the particular realization of the model, as the spread of the random pseudo experiments indicates. Moreover, the agreement between the data and the model distributions can improve at first with the introduction of a boundary, before it eventually deteriorates.

7.4.2 Flavor Composition

In the *2-flavor* model introduced in section 7.1.2, the flavor composition of the cosmic neutrino flux at Earth can be expressed by the fraction of electron neutrinos with respect to the total flux. Data chal-

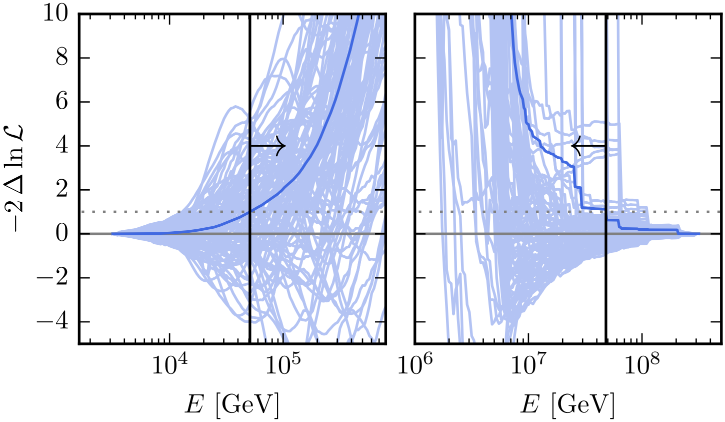

(a) Test Flux (1).

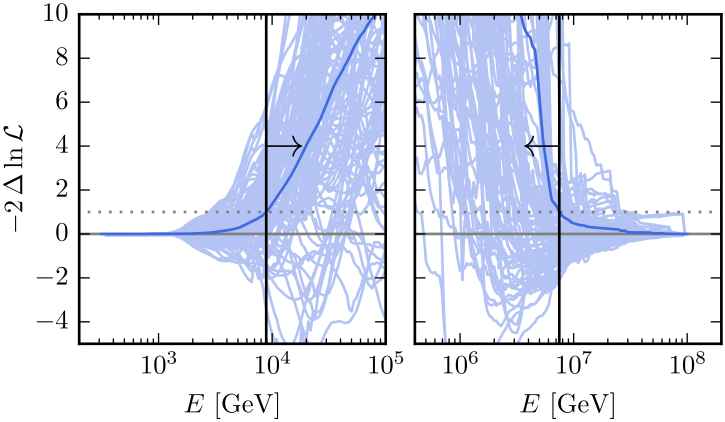

(b) Test Flux (2).

Figure 7.7 — *Credible Energy Interval Data Challenge.* Variation of the test statistic, as a function of the lower (left) and upper (right) energy bound. The dark blue line represents the Asimov data set, with the derived expected bounds indicated by the black arrows. The results of 100 random pseudo experiments are shown in light blue. The abrupt steps in particular for the upper bound are due to a lack of statistics in the simulation of the model distributions at very high energies.

lenges for this quantity with the test fluxes (1) and (2) are shown in fig. 7.8 and 7.9, respectively. The input fraction of the test flux was 0.33 in both cases, as marked by the pink line. This corresponds to the pion-decay source scenario introduced in section 3.1.3. The sensitivity of the analysis can be judged from the indicated 68% and 90% confidence intervals, and is slightly better for the harder test flux (1). On average, the input electron neutrino fraction is recovered in the random pseudo experiments.

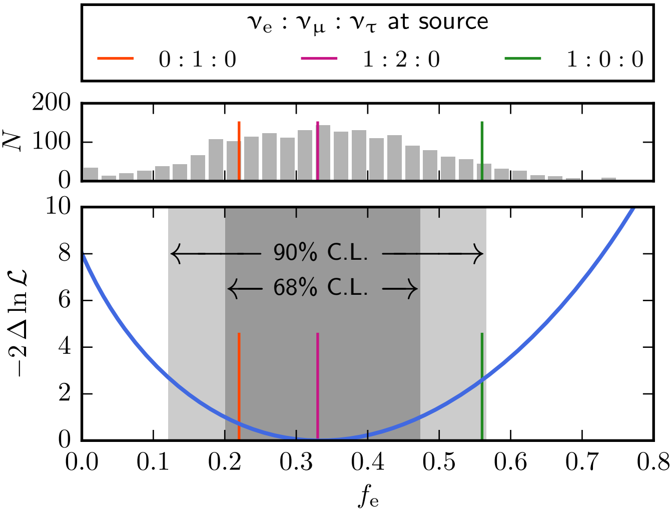

Figure 7.8 — *Flavor Composition Data Challenge (2-Flavor Model): Test Flux (1).* Electron neutrino fraction f_e at Earth recovered by the likelihood analysis. The blue line shows a profile likelihood scan for the Asimov data set, the derived 68% and 90% confidence level intervals are indicated. The histogram in the upper panel shows the results of 2,000 random pseudo experiments. Fractions expected for the different source scenarios introduced in section 3.1.3 are marked by the colored lines.

Data challenges for the flavor composition in the *3-flavor* model are presented in fig. 7.10 and 7.11 for test fluxes (1) and (2), respectively. Again, the input flavor composition corresponds to that of a pion-decay source, *i.e.* $\nu_e : \nu_\mu : \nu_\tau = 1 : 1 : 1$ at Earth. The compositions

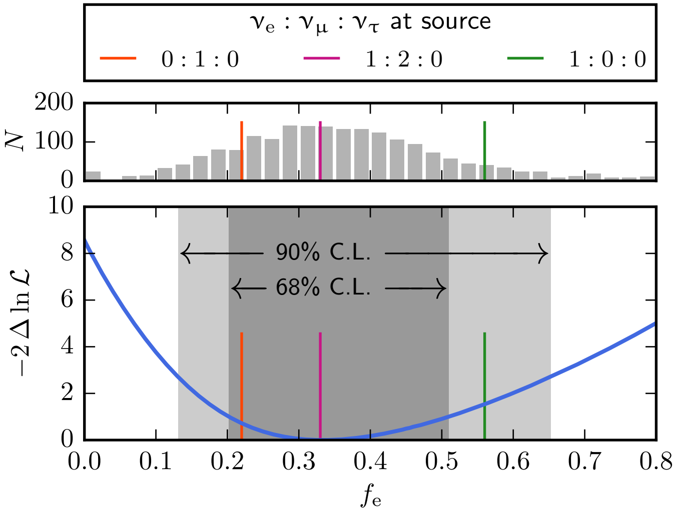

Figure 7.9 — *Flavor Composition Data Challenge (2-Flavor Model): Test Flux (2).* See description of fig. 7.8.

recovered in the pseudo experiments show a large scatter around the true value, in accordance with the large regions of parameter space allowed by the confidence contours of the Asimov data set. As in the *2-flavor* model, the sensitivity is slightly better for test flux (1). In general, the sensitivity to a tau neutrino component of the cosmic neutrino flux is poor, this is a result of the lack of ν_τ-identification techniques in the searches that are considered in this analysis.

7.4.3 *P*-Values

Finally, the definitions of the likelihood ratio test and goodness-of-fit test p-values can be verified with a simple sanity check. If the correct model is fitted to the data, the resulting p-values should follow a flat distribution between 0 and 1. This can be tested in a data challenge, where the random data are generated from a known model.

The result of this data challenge is shown in fig. 7.12. The generated pseudo experiments are fitted with the same model that was used to

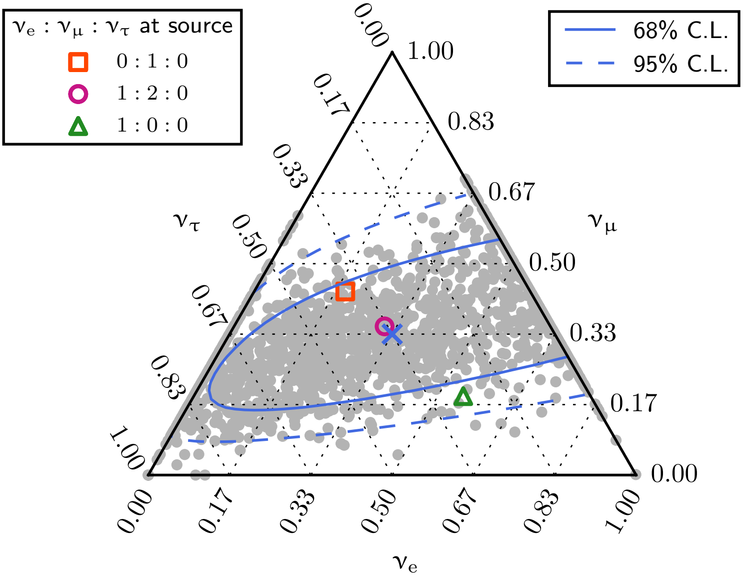

Figure 7.10 — *Flavor Composition Data Challenge (3-Flavor Model): Test Flux (1).* Flavor composition of the cosmic neutrino flux at Earth recovered by the likelihood analysis. Fractions of the three neutrino flavors with respect to the total flux can be read off the three axes. The input flavor composition is marked by the blue cross. The blue lines represent 68% and 95% confidence level contours obtained from the Asimov data set. Results of 2,000 random pseudo experiments are shown as gray dots. Flavor compositions expected for three different source scenarios are also shown.

generate the random data. As expected, the distributions of both the likelihood ratio test as well as the goodness-of-fit test p-value are flat in this case.

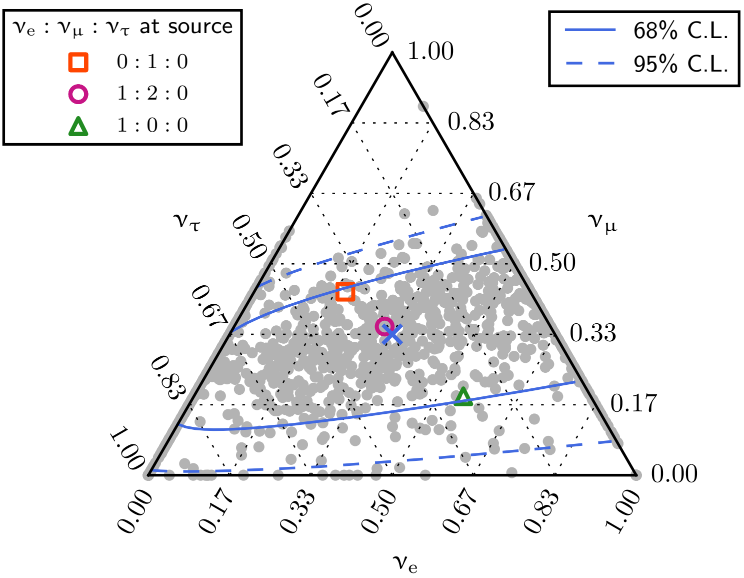

Figure 7.11 — *Flavor Composition Data Challenge (3-Flavor Model): Test Flux (2).* See description of fig. 7.10.

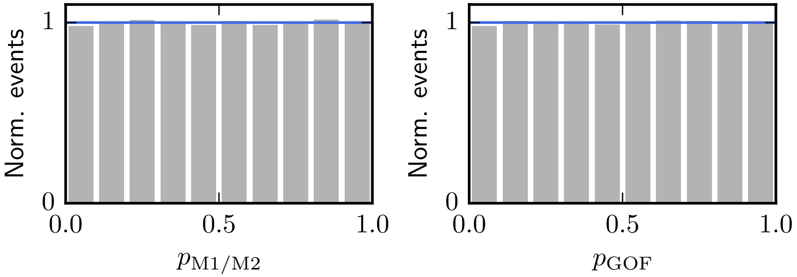

Figure 7.12 — *P-Value Distributions for a True Model.* Normalized distribution of a likelihood ratio test p-value (left) and a goodness-of-fit test p-value (right) for an ensemble of pseudo experiments, where the same model was used to generate and fit the pseudo data. As expected, the distributions are both flat.

Chapter 8

Results

> *"Get your facts first,*
> *and then you can distort them as much as you please."*
> — Mark Twain (1899) [248]

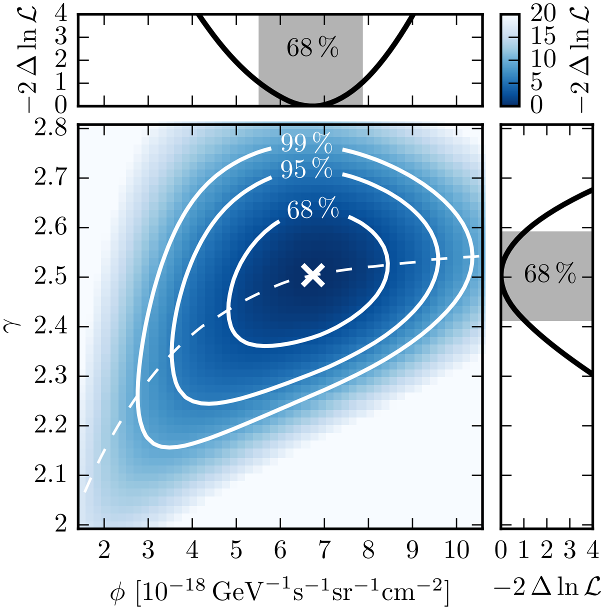

Figure 8.1 — *Constraints on the Parameters of the Cosmic Neutrino Flux.* Shown are one- and two-dimensional profile likelihood scans of the cosmic flux parameters ϕ and γ. The obtained confidence level intervals are indicated. The best-fit result is marked with '×', the dashed line shows the conditional best-fit value of γ as a function of ϕ.

RESULTS OF THE LIKELIHOOD ANALYSIS introduced in the preceding chapter are presented in the following. Section 8.1 presents results on the energy spectrum of the cosmic neutrino flux. For these results, a flavor composition of $\nu_e : \nu_\mu : \nu_\tau = 1:1:1$ was assumed. The results of the measurement of the flavor composition of the cosmic neutrino flux are then presented in section 8.2.

8.1 Results on the Energy Spectrum

Section 8.1.1 describes the results on the energy spectrum that were obtained with the *power law* model. The results obtained with other spectral models and with the *north-south* model are presented in section 8.1.2 and section 8.1.3, respectively. Note that in the following, quoted best-fit normalizations of the cosmic neutrino flux are for the total flux of all three neutrino flavors.

8.1.1 Power Law Model

The best-fit parameter values of the *power law* model obtained with the likelihood analysis are listed in table 8.1. Specifically, the best power-law description of the cosmic neutrino flux is given by a power law with normalization

$$\phi = \left(6.7^{+1.1}_{-1.2}\right) \times 10^{-18}\,\mathrm{GeV}^{-1}\,\mathrm{s}^{-1}\,\mathrm{sr}^{-1}\,\mathrm{cm}^{-2} \tag{8.1}$$

at 100 TeV and spectral index

$$\gamma = 2.50 \pm 0.09\,. \tag{8.2}$$

Figure 8.1 shows confidence regions for these two parameters.

The analysis favors a vanishing prompt atmospheric neutrino flux, with a 90% C.L. upper limit of 2.1 times the (modified) prediction of the ERS model [223].[1] The goodness-of-fit p-value for the *power law* model is 37.6%, thus providing no evidence for significant discrepancies between the best-fit model and the experimental data. On the other hand, a likelihood ratio test between a model with fixed index $\gamma = 2$ and the best-fit model yields a p-value of 0.0066%. This corresponds to a rejection of a flux of the form E^{-2} by 3.8 standard deviations.[2]

---

[1] This translates into an upper limit of 6.2 times the newer BERSS model [227].

[2] A one-sided Gaussian distribution is used to convert to standard deviations.

Table 8.1 — *Best-Fit Parameter Values for the Power Law Model.* 68% and 90% confidence level intervals are also stated. The deviation of nuisance parameters from their default value in units of the prior width σ is listed as "Pull". ϕ denotes the all-flavor cosmic neutrino flux at 100 TeV in units of $10^{-18}\,\mathrm{GeV}^{-1}\,\mathrm{s}^{-1}\,\mathrm{sr}^{-1}\,\mathrm{cm}^{-2}$, γ the spectral index (*cf.* section 7.1.2). The normalization of the conventional and prompt atmospheric neutrino fluxes, ϕ_{conv} and ϕ_{prompt}, are given as multiples of the default model predictions.

Param.	Best fit	68% C.L.	90% C.L.	Pull
ϕ_{conv}	1.10	0.94 – 1.31	0.87 – 1.49	–
ϕ_{prompt}	0.00	0.00 – 1.04	0.00 – 2.11	–
ϕ	6.7	5.5 – 7.8	4.6 – 8.6	–
γ	2.50	2.41 – 2.59	2.35 – 2.65	–
$\Delta\gamma_{\mathrm{cr}}$	0.017	−0.008 – 0.041	−0.023 – 0.057	0.34
$\phi_{\mu,\mathrm{S1}}$	1.09	0.72 – 1.51	0.52 – 1.80	0.18
$\phi_{\mu,\mathrm{S2}}$	0.84	0.31 – 1.37	0.00 – 1.71	−0.32
$\phi_{\mu,\mathrm{H1}}$	1.12	0.75 – 1.54	0.56 – 1.84	0.23
$\phi_{\mu,\mathrm{H2}}$	1.27	0.94 – 1.61	0.73 – 1.84	0.54
$\phi_{E,\mathrm{S1}}$	0.95	0.88 – 1.04	0.84 – 1.12	−0.34
$\phi_{E,\mathrm{S2}}$	1.00	0.88 – 1.22	0.83 – 1.32	0.03
$\phi_{E,\mathrm{T1}}$	1.02	0.95 – 1.09	0.90 – 1.14	0.10
$\phi_{E,\mathrm{T2}}$	1.05	0.97 – 1.12	0.93 – 1.17	0.30
$\phi_{E,\mathrm{H1}}$	0.96	0.88 – 1.06	0.84 – 1.12	−0.29
$\phi_{E,\mathrm{H2}}$	0.95	0.86 – 1.04	0.81 – 1.10	−0.35

Distributions of the observables as defined in table 6.1 corresponding to the best-fit results are shown in figs. 8.2–8.5. Note that the green dashed line represents an upper limit on the contribution of the prompt atmospheric component above the background of atmospheric muons and conventional atmospheric neutrinos. All distributions show the sum of all neutrino flavors.

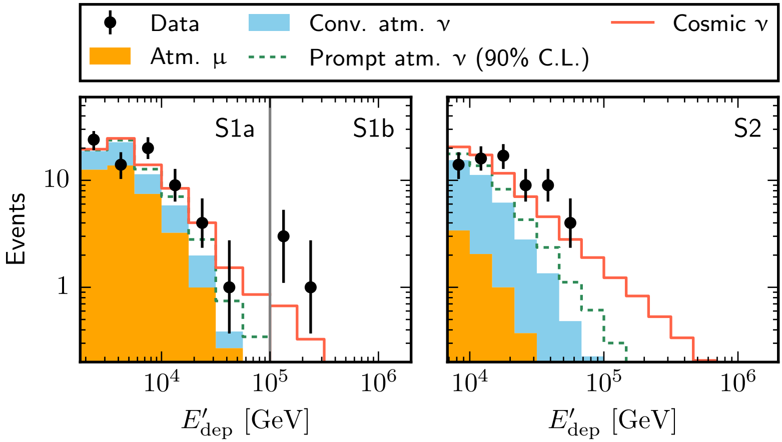

Figure 8.2 — *Best-Fit Observable Distributions of Shower Samples.* The background of atmospheric muons and conventional atmospheric neutrinos is shown as a stacked, filled histogram. The dashed line represents a 90% C.L. upper limit on the additional contribution of prompt atmospheric neutrinos; the solid line shows the contribution of cosmic neutrinos, added onto the background histogram. Error bars represent 68% C.L. intervals as defined in [240].

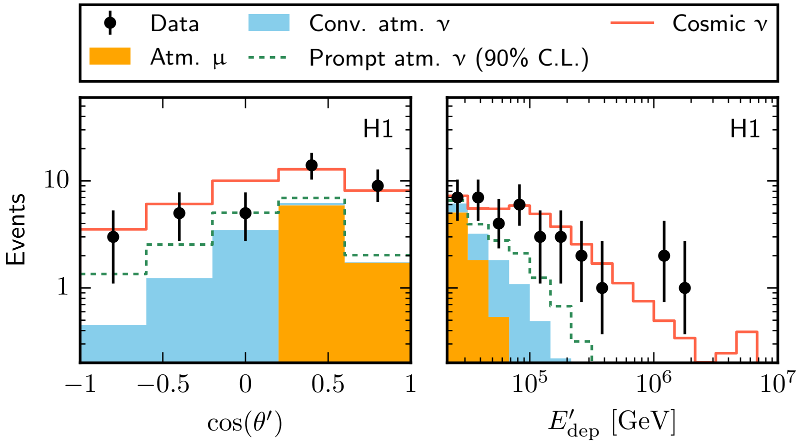

Figure 8.3 — *Best-Fit Observable Distributions of the Hybrid Sample H1.* See description of fig. 8.2.

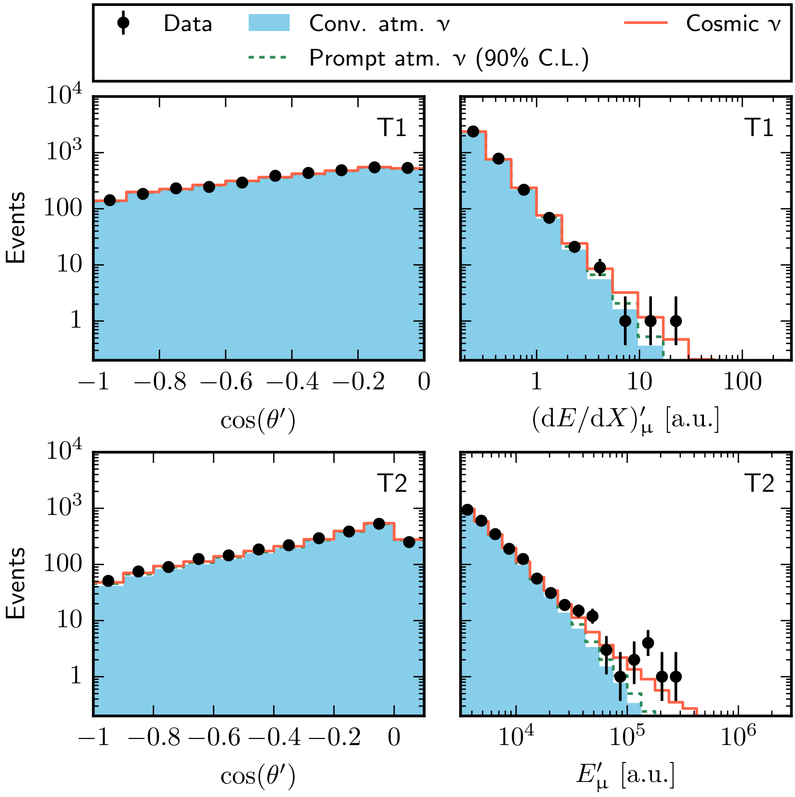

Figure 8.4 — *Best-Fit Observable Distributions of Track Samples.*
See description of fig. 8.2.

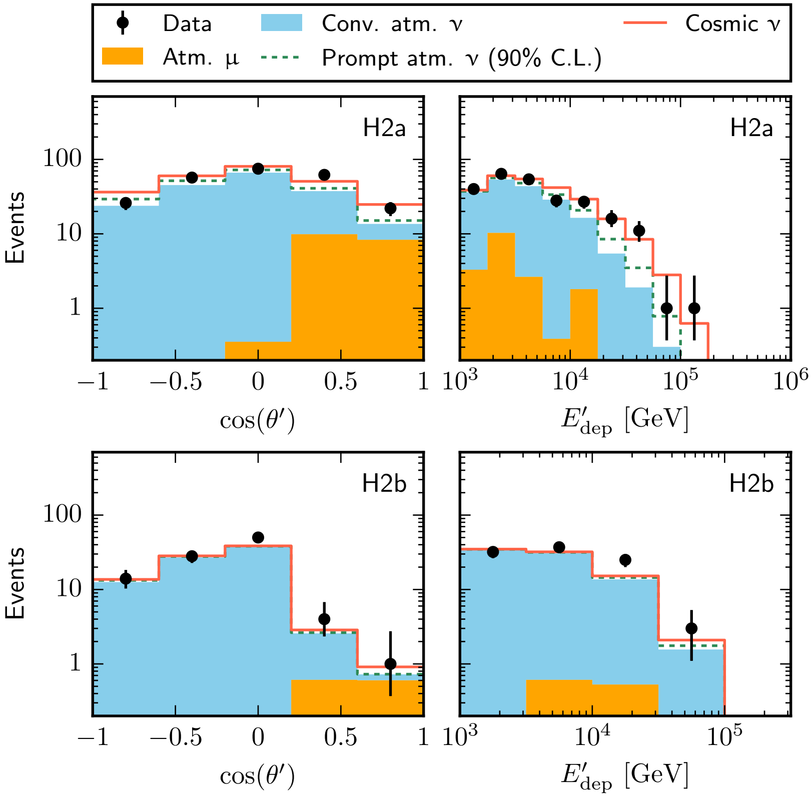

Figure 8.5 — *Best-Fit Observable Distributions of Hybrid Sample* H2.
See description of fig. 8.2.

Credible Energy Interval

The calculation of the credible energy interval, carried out as described in section 7.2.4, is visualized in fig. 8.6. The derived credible interval ranges from 25 TeV to 2.8 PeV in neutrino energy. Outside this interval, the best-fit *power law* model is not supported by the experimental data.

The dip in the red curve below the lower bound of the range indicates that a spectrum that starts at ~ 15 TeV instead of a continuous power law would be slightly preferred. This explains why the lower bound is slightly larger than expected on average for a spectrum similar to the one observed (*cf.* fig. 7.7(b)).

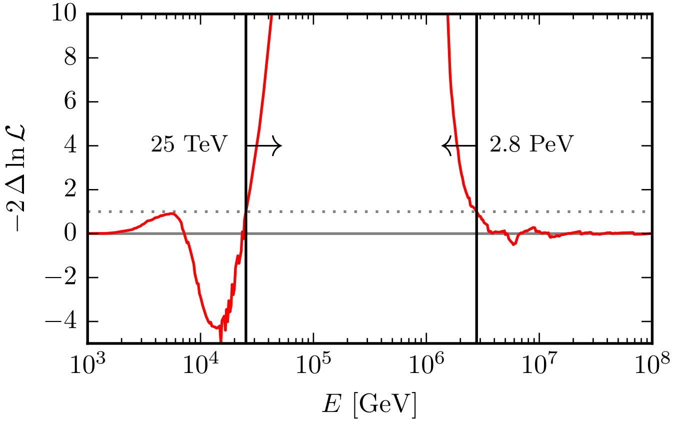

Figure 8.6 — *Credible Energy Interval.* Credible energy interval of the measurement, calculated as described in section 7.2.4. The spikes in the red curve are due to individual simulated events that are removed in the procedure.

The spectrum of the best-fit cosmic neutrino flux within the credible energy interval is compared to the best-fit spectrum of the conventional atmospheric neutrino flux in fig. 8.7. The 90% C.L. upper limit on the prompt atmospheric neutrino flux is shown in addition. The all-flavor cosmic neutrino flux supersedes the background of atmospheric neutrinos around neutrino energies of 100 TeV.

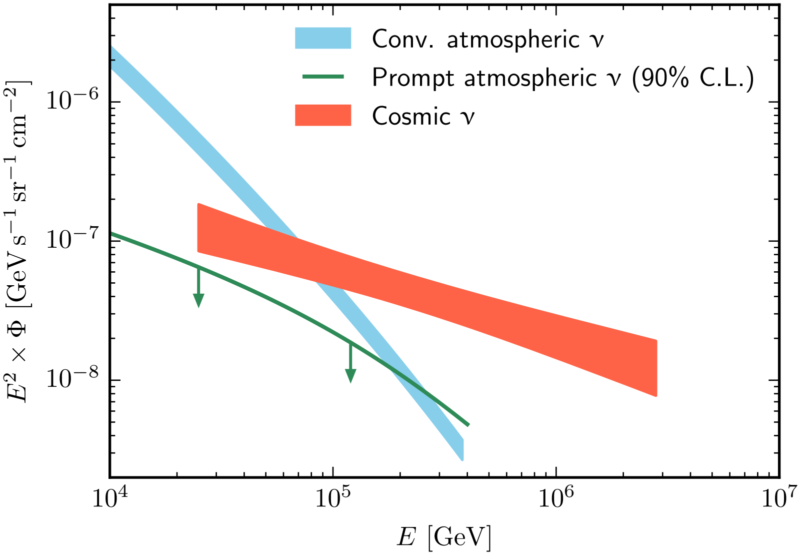

Figure 8.7 — *Best-Fit Atmospheric and Cosmic Neutrino Fluxes.* The energy spectrum of the best-fit cosmic neutrino flux, compared to the conventional atmospheric neutrino flux. The filled areas represent the envelope of the spectra allowed at 68% C.L. In addition, the 90% C.L. upper limit on the prompt atmospheric neutrino flux is shown.

Correlation with the Prompt Atmospheric Neutrino Flux

While the analysis favors a vanishing prompt atmospheric neutrino flux, the unequivocally acknowledged existence of charm mesons implies that such a flux must exist at a certain level. It is thus instructive to investigate the correlation between the parameters of the cosmic neutrino flux and the magnitude of the prompt atmospheric flux. The correlation is illustrated by the profile likelihood scans shown in fig. 8.8.

For a prompt atmospheric neutrino flux fixed at the 90% confidence level upper limit derived here (2.1 times the modified ERS model), the best-fit values for the parameters of the cosmic neutrino flux are $\phi = 5.4 \times 10^{-18}\,\mathrm{GeV}^{-1}\,\mathrm{s}^{-1}\,\mathrm{sr}^{-1}\,\mathrm{cm}^{-2}$ and $\gamma = 2.44$, respectively. For a prompt flux at the level of the prediction of the ERS model, the best-fit values are $\phi = 6.0 \times 10^{-18}\,\mathrm{GeV}^{-1}\,\mathrm{s}^{-1}\,\mathrm{sr}^{-1}\,\mathrm{cm}^{-2}$ and $\gamma = 2.47$.

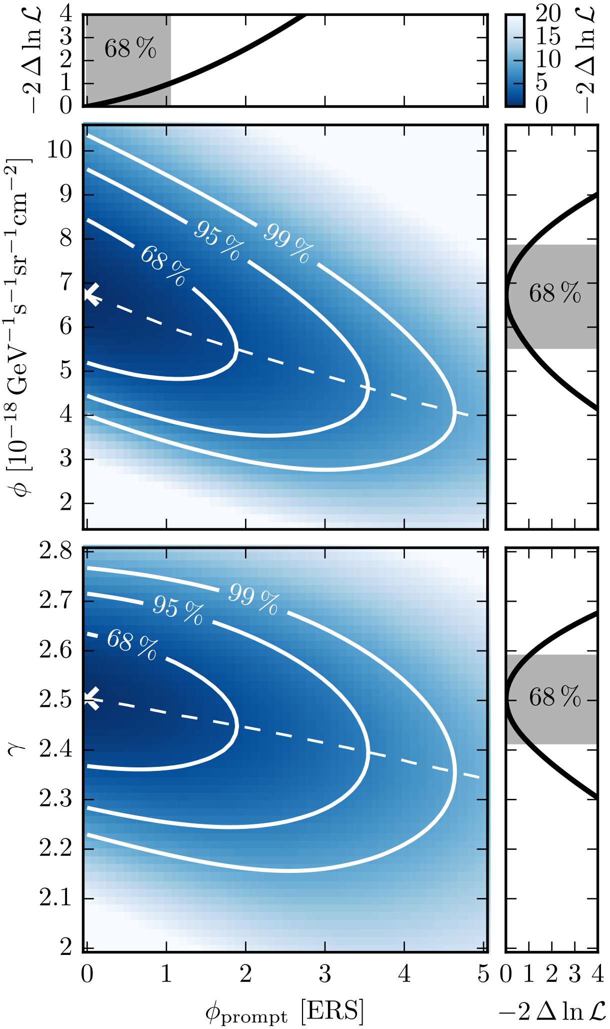

Figure 8.8 — *Correlation Between the Astrophysical and the Prompt Atmospheric Neutrino Flux.* Profile likelihood scans of the parameters of the prompt atmospheric (ϕ_{prompt}) and the cosmic (ϕ, γ) neutrino flux. The best-fit result is marked with '×', the dashed lines show the conditional best-fit values of ϕ and γ as a function of ϕ_{prompt}.

Consistency Between Samples

An important test is to check for consistency between the different samples contributing to the analysis (*cf.* chapter 6). One such test are so-called *leave-one-out* fits, where the analysis is repeated with one of the samples excluded. The results of this test are shown in fig. 8.9. The largest deviation is observed for the exclusion of event sample H2. This can be understood when recalling that event sample H2 includes events with deposited energies down to 1 TeV, lower than any of the other samples that include shower events. Excluding this sample significantly reduces the “lever arm” that is required to constrain the energy spectrum.

Another test is to perform the likelihood analysis on each of the samples separately and to compare the results. This test is depicted

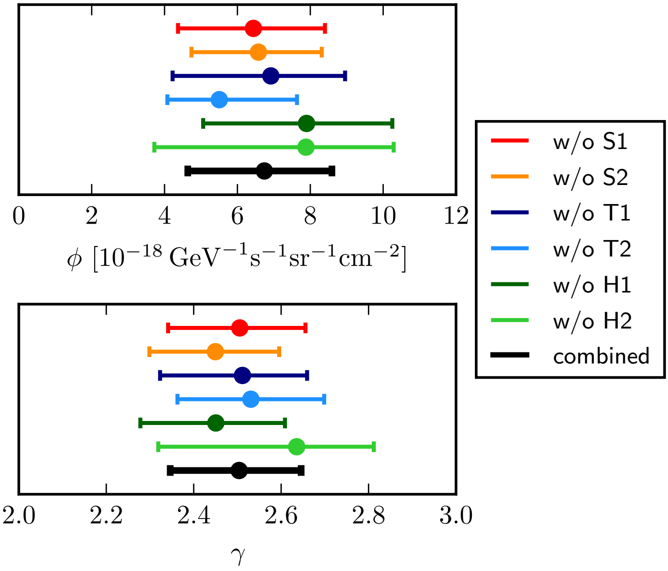

Figure 8.9 — *Comparison of Leave-One-Out Fits.* Best-fit values and 90% C.L. intervals obtained from fits in which one of the samples was excluded. The combined fit result with all samples included is shown for comparison. Note that the displayed uncertainties are not independent.

in fig. 8.10. As is visible, the fit result obtained with each of the samples is well compatible with the combined result. The figure furthermore demonstrates the gain in precision achieved by the combined analysis.[3]

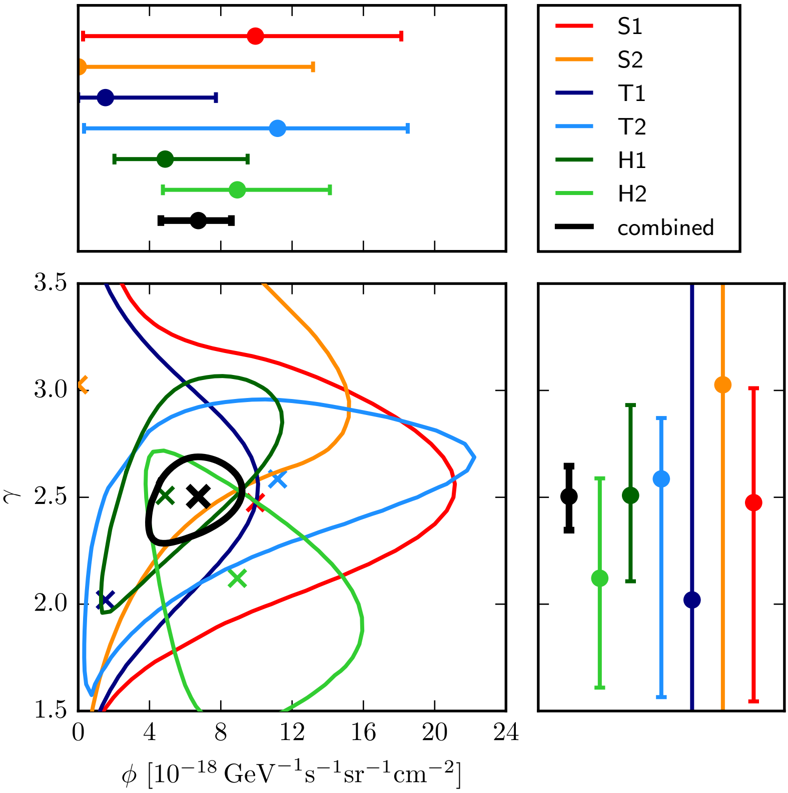

Figure 8.10 — *Comparison of Results from Individual Samples.* The central panel shows best-fit values and 90% C.L. regions for the parameters ϕ and γ of the cosmic neutrino flux obtained by performing the likelihood analysis on the individual samples, as well as the combined fit result. The panels at the top and right show one-dimensional projections.

---

[3] This argument is not entirely honest, because some of the event samples were adapted for the combined analysis (see section 6.2). A version of fig. 8.10 with the event samples restored to their original size can be found in appendix D.

8.1.2 Other Spectral Models

Despite the larger number of model parameters, neither the *power law + cut-off* model nor the *two power laws* model represent a better description of the data than the *power law* model (*i.e.* both are identical to the *power law* model at the best fit). The 90% C.L. lower limit on the cut-off energy is $E_{\text{cut}} > 1.7\,\text{PeV}$. For two components that contribute equally to the total cosmic neutrino flux at 100 TeV, the 90% C.L. upper limit on the difference of their spectral indices is $\Delta\gamma < 0.57$.

The best-fit result of the *differential* model is illustrated in fig. 8.11. Deviations from the *power law* model are perceivable in the 2nd, 6th, and 7th energy interval, centered at 30 TeV, 700 TeV, and 1.5 PeV, respectively. Note however that none of these deviations is statistically significant. The results are summarized in table 8.2.

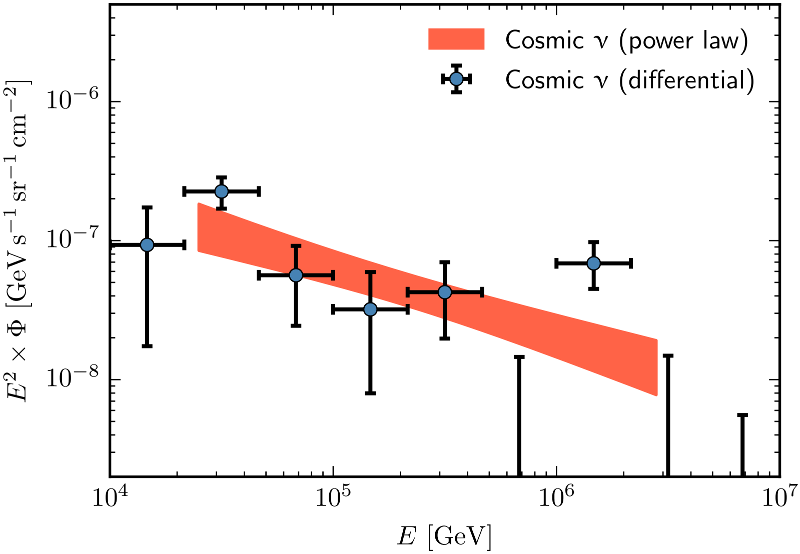

Figure 8.11 — *Best-Fit Differential Energy Spectrum.* The blue points show the best-fit normalization of the cosmic all-flavor neutrino flux in each energy interval (marked by the horizontal error bars). The vertical error bars indicate the 68% C.L. interval. The best-fit energy spectrum of the *power law* model is shown for comparison (*cf.* fig. 8.7).

Table 8.2 — *Best-Fit Parameter Values for the Differential Model.* $\phi_1 - \phi_9$ denote the normalization of the all-flavor cosmic neutrino flux (multiplied with E^2) in the nine individual energy intervals, logarithmically spaced between 10 TeV and 10 PeV. They are specified in units of $10^{-8}\,\mathrm{GeV\,s^{-1}\,sr^{-1}\,cm^{-2}}$.

Param.	Best fit	68% C.L.	90% C.L.
ϕ_1	9.3	1.7 – 17.3	0.0 – 22.7
ϕ_2	22.6	17.0 – 28.5	13.5 – 32.5
ϕ_3	5.6	2.4 – 9.2	0.5 – 11.6
ϕ_4	3.2	0.8 – 5.9	0.0 – 7.9
ϕ_5	4.3	2.0 – 7.0	0.8 – 9.0
ϕ_6	0.0	0.0 – 1.5	0.0 – 3.5
ϕ_7	6.9	4.5 – 9.7	3.1 – 11.9
ϕ_8	0.0	0.0 – 1.5	0.0 – 3.8
ϕ_9	0.0	0.0 – 0.6	0.0 – 1.5

8.1.3 North-South Model

The results of the *north-south* model are summarized in table 8.3. The best-fit spectral indices of the cosmic neutrino flux in the northern and southern hemisphere are

$$\gamma_{\mathrm{N}} = 2.0^{+0.3}_{-0.4} \tag{8.3}$$

and

$$\gamma_{\mathrm{S}} = 2.56^{+0.11}_{-0.12}\,, \tag{8.4}$$

respectively. The best-fit value of γ_{N} is noticeably different from the value of $\gamma = 2.5$ obtained in the isotropic *power law* model. However, because the uncertainty on γ_{N} is much larger, this discrepancy is not statistically significant: a likelihood ratio test between the *power law* model and the *north-south* model yields a p-value of 13%, corresponding to 1.1 standard deviations. This is also evident from fig. 8.12, which shows profile likelihood scans of the two spectral indices γ_{N} and γ_{S}. The isotropic result of $\gamma = 2.5$ (marked by '+') is contained within the 95% confidence level contour of the best-fit result.

Table 8.3 — *Best-Fit Parameter Values for the North-South Model.* ϕ_{N} and ϕ_{S} denote the all-flavor cosmic neutrino flux at 100 TeV in the northern and southern sky, respectively, specified in units of $10^{-18}\,\mathrm{GeV}^{-1}\,\mathrm{s}^{-1}\,\mathrm{sr}^{-1}\,\mathrm{cm}^{-2}$. γ_{N} and γ_{S} are the corresponding spectral indices.

Param.	Best fit	68% C.L.	90% C.L.
ϕ_{N}	2.1	0.5 – 5.0	0.1 – 7.3
γ_{N}	2.0	1.6 – 2.3	1.2 – 2.5
ϕ_{S}	6.8	5.3 – 8.4	4.4 – 9.5
γ_{S}	2.56	2.44 – 2.67	2.36 – 2.75

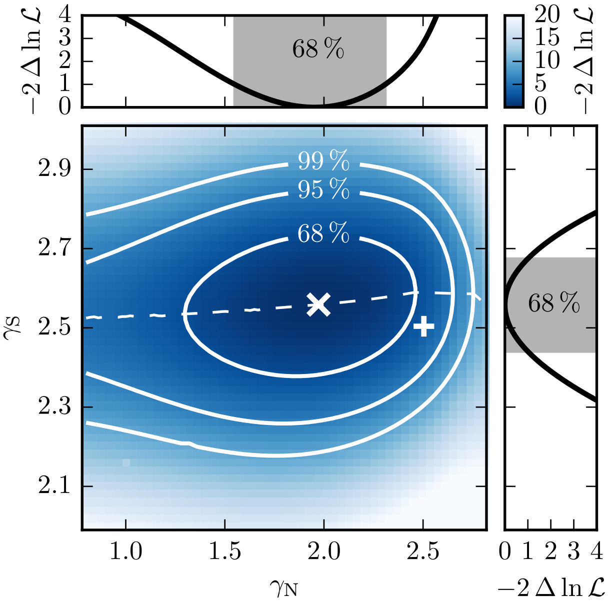

Figure 8.12 — *Spectral Indices in the North-South Model.* Profile likelihood scans of the spectral index parameters γ_{N} and γ_{S}. The best-fit values are marked with '×', the dashed line shows the conditional best-fit value of γ_{S} as a function of γ_{N}. The '+' marks the result of the isotropic *power law* model.

8.2 Results on the Flavor Composition

In this section, the results of the *2-flavor* model (section 8.2.1) and the *3-flavor* model (section 8.2.2) are presented. Note that in both models, all components of the cosmic neutrino flux are assumed to have the same energy dependence, namely a power law with spectral index γ.

8.2.1 2-Flavor Model

Table 8.4 shows the best-fit values of the parameters of the cosmic neutrino flux for the *2-flavor* model. The result corresponds to a fraction of electron neutrinos in the cosmic neutrino flux of $f_\mathrm{e} = 0.18 \pm 0.11$, measured at the Earth. This value is compatible with that expected for pion-decay sources ($\nu_\mathrm{e} : \nu_\mu : \nu_\tau = 1 : 2 : 0$ at the sources, $f_\mathrm{e} \approx 0.33$) and muon-damped sources ($0 : 1 : 0$, $f_\mathrm{e} \approx 0.22$), but incompatible with the neutron-beam source scenario ($1 : 0 : 0$, $f_\mathrm{e} \approx 0.56$) at 3.0 standard deviations (p-value 0.13%). This is also illustrated in fig. 8.13, which shows a profile likelihood scan of the parameter f_e.

The constraints on the spectral index γ are very similar to those obtained in the *power law* model, showing that the energy spectrum and the flavor composition are not strongly correlated.

Table 8.4 — *Best-fit Parameter Values for the 2-Flavor Model.* ϕ_e and $\phi_{\mu+\tau}$ denote the cosmic ν_e and combined $\nu_\mu + \nu_\tau$ flux at 100 TeV, respectively, specified in units of $10^{-18}\,\mathrm{GeV}^{-1}\,\mathrm{s}^{-1}\,\mathrm{sr}^{-1}\,\mathrm{cm}^{-2}$. γ denotes the spectral index of the cosmic neutrino flux (common to all flavors).

Param.	Best fit	68% C.L.	90% C.L.
ϕ_e	1.3	0.5 – 2.1	0.0 – 2.6
$\phi_{\mu+\tau}$	5.6	4.4 – 6.9	3.7 – 7.8
γ	2.51	2.42 – 2.60	2.36 – 2.66

8.2.2 3-Flavor Model

Results of the *3-flavor* model are summarized in table 8.5. The likelihood analysis favors a vanishing ν_τ-component, and approximately

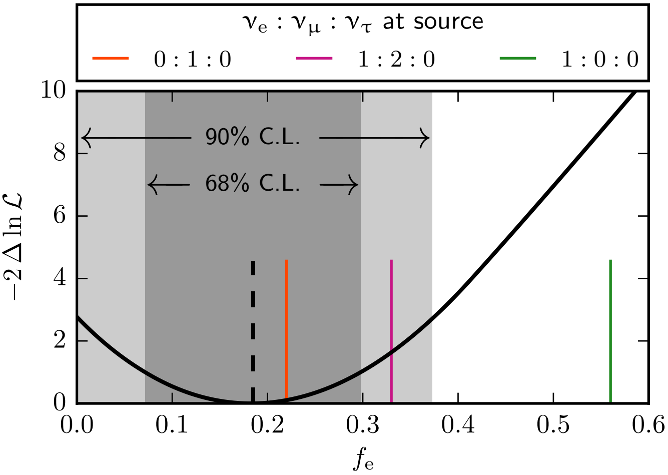

Figure 8.13 — *Electron Neutrino Fraction of the Cosmic Neutrino Flux.* Profile likelihood scan of the fraction of electron neutrinos in the cosmic neutrino flux, f_e, measured at Earth and assuming equal amounts of muon and tau neutrinos. The dashed line marks the best-fit value; the colored lines mark values expected for different source scenarios.

equal fluxes of ν_e and ν_μ. However, as evident from fig. 8.14, large regions of the parameter space are compatible with the data. Specifically, likelihood ratio tests of the pion-decay ($\nu_e : \nu_\mu : \nu_\tau = 1 : 2 : 0$ at the sources) and muon-damped ($0 : 1 : 0$) source scenarios to the best-fit composition model yield p-values of 27% and 55%, respectively, indicating agreement with the data. On the other hand, the corresponding p-value for the neutron-beam source scenario ($1 : 0 : 0$) is 0.014%, which corresponds to a discrepancy of 3.6 standard deviations.

As in the *2-flavor* model, the results do not depend strongly on the spectral index of the cosmic neutrino flux.

A prominent feature of fig. 8.14 is the "band" of allowed flavor compositions that spans the width of the triangle, indicating a degeneracy between the ν_e and the ν_τ-fraction of the flux.[4] As already alluded to in section 7.4.2, this is a result of the lack of positively identified ν_τ in the event samples analyzed here.

---

[4] The band is not exactly aligned with the ν_μ-axis because muons are produced in 17% of all charged-current ν_τ interactions [51].

Table 8.5 — *Best-fit Parameter Values for the 3-Flavor Model.* ϕ_e, ϕ_μ, and ϕ_τ denote the cosmic ν_e, ν_μ, and ν_τ flux at 100 TeV, respectively, specified in units of $10^{-18}\,\mathrm{GeV}^{-1}\,\mathrm{s}^{-1}\,\mathrm{sr}^{-1}\,\mathrm{cm}^{-2}$. γ denotes the spectral index of the cosmic neutrino flux (common to all flavors).

Param.	Best fit	68% C.L.	90% C.L.
ϕ_e	2.9	1.4 – 3.6	0.0 – 4.2
ϕ_μ	3.0	2.4 – 3.7	2.1 – 4.2
ϕ_τ	0.0	0.0 – 2.3	0.0 – 5.0
γ	2.55	2.46 – 2.64	2.40 – 2.69

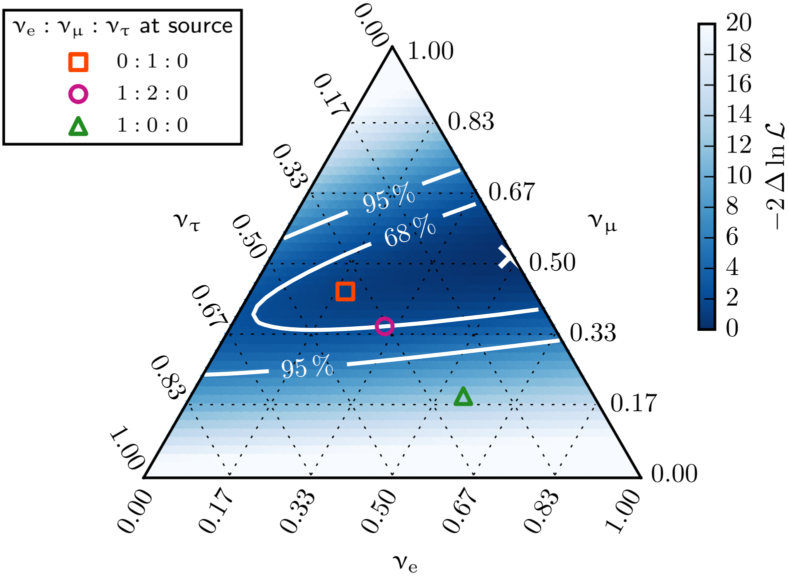

Figure 8.14 — *Flavor Composition of the Cosmic Neutrino Flux.* Profile likelihood scan of the flavor composition of the cosmic neutrino flux, measured at Earth (*cf.* fig. 3.3). Fractions of the three neutrino flavors with respect to the total flux can be read off the three axes. The best-fit composition is marked with '×', 68% and 95% C.L. regions are indicated. Compositions expected for different source scenarios are shown by colored markers.

Chapter 9

Discussion and Outlook

> *"There are no facts, only interpretations."*
>
> — Friedrich Nietzsche (1886/1887) [249]

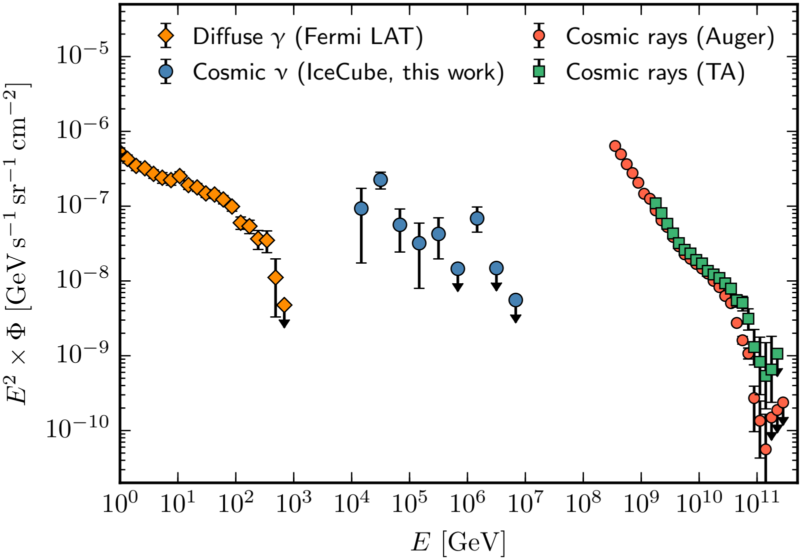

Figure 9.1 — *Diffuse Neutrino, Photon, and Cosmic-Ray Fluxes.* The measurement of the diffuse cosmic neutrino flux obtained in this work (*cf.* fig. 8.11) is compared to measurements of the diffuse extragalactic γ-ray background by the Fermi LAT experiment [143] and measurements of the ultra-high-energy cosmic-ray flux by the Telescope Array experiment [7] and the Pierre Auger Observatory [8]. Upper limits are at one standard deviation confidence.

Understanding the implications of the results obtained in this work requires to put them into perspective, as this chapter aims to accomplish. In section 9.1, the results are compared to previously published measurements, demonstrating that they are in agreement. Astrophysical implications are then discussed in section 9.2.

The IceCube detector continues to take data, and the results presented here will soon be refined. Section 9.3 gives an outlook on results that can be expected to be obtained in the foreseeable future.

9.1 Comparison to Previous Measurements

9.1.1 Energy Spectrum

An important cross-check regarding the internal consistency of the results on the energy spectrum was already presented in the previous chapter, see fig. 8.9 and 8.10 (*cf.* also fig. D.1). This cross-check showed that all individual event samples are well compatible with a cosmic neutrino flux as measured in this work. In particular, while a large prompt atmospheric neutrino flux is favored over the presence of a cosmic neutrino flux in the separate analysis of event sample S2, it was shown that the reverse interpretation also fits the data well. This circumstance emphasizes the importance of analyzing all available data jointly.

The IceCube Collaboration has published measurements of the energy spectrum of the cosmic neutrino flux in [20–22], these measurements were based on event samples that are also used in this work (H1, H2, and T2, respectively). In each case, the cosmic neutrino flux was described with a power law model as introduced in chapter 7. The published results are not identical to those shown in fig. D.1 because the analyzed energy ranges and the treatment of systematic uncertainties were slightly modified to facilitate the combined analysis presented here. A comparison of the constraints on the spectral index of the cosmic neutrino flux obtained in this work and the previous publications is shown in fig. 9.2. The best-fit value of the spectral index increases as the energy interval broadens, in particular as the measurement is extended to lower energies. This, however, does not indicate that the spectral index changes with energy; no evidence for such a hypothesis was found (*cf.* the results for the *two power laws* model).

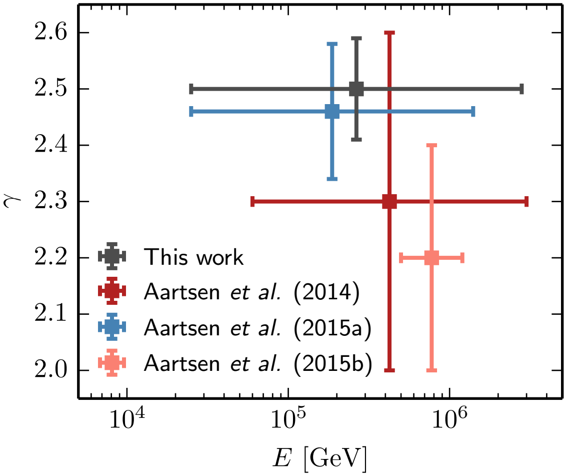

Figure 9.2 — *Comparison of Energy Spectrum Measurements.*
The constraints on the spectral index γ of the cosmic neutrino flux obtained in this work (*cf.* eq. 8.2, fig. 8.6) are compared to those obtained by Aartsen *et al.* (2014) [20], Aartsen *et al.* (2015a) [21], and Aartsen *et al.* (2015b) [22]. The squares mark the best-fit values, the horizontal error bars denote the quoted energy interval of the measurements, and the vertical error bars the 68% C.L. interval for γ. Note that the event samples of the three analyses are part of the data analyzed in this work (samples H1, H2, and T2, respectively) and not independent, and that the measurement of [22] is valid only for the northern hemisphere.

9.1.2 Flavor Composition

Previous measurements of the flavor composition of the cosmic neutrino flux measured with IceCube were performed by the IceCube Collaboration itself [36] as well as by other authors [250–253].[1] All measurements are based on the data published in [20]. Palladino *et al.* [253] additionally considered a preliminary version of the results published in [22], while an additional sample of shower events was selected for the analysis published in [36]. The analysis presented here achieves a significantly better precision than any of the previous measurements.

---

[1] Note that [252] represents an update of the analysis in [250] by the same authors.

This is largely a result of the bigger event sample that was analyzed, in particular of the fact that the combined event sample contains a significant number of shower events as well as track events.

The results of [250, 251] disagree with those obtained here, this is likely due to the negligence of systematic uncertainties in the prediction of the atmospheric backgrounds in these analyses. On the other hand, the results presented in [36, 252, 253] qualitatively agree with the results of this work. A comparison of constraints on the flavor composition is shown in fig. 9.3.[2] The large discrepancy between the best-fit compositions is not unexpected, considering the large uncertainties.

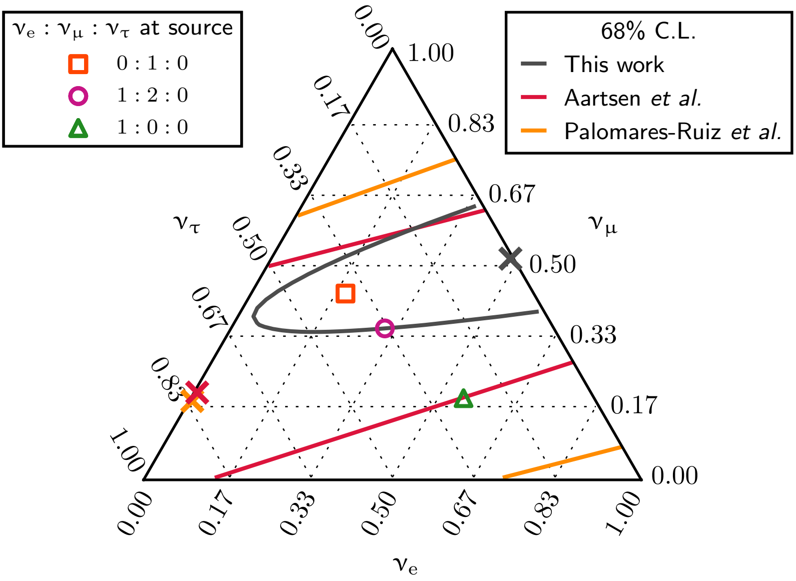

Figure 9.3 — *Comparison of Flavor Composition Measurements.* The constraints on the flavor composition of the cosmic neutrino flux obtained in this work (*cf.* fig. 8.14) are compared to those obtained by Aartsen *et al.* [36] and Palomares-Ruiz *et al.* [252]. Best-fit compositions are marked with '×', the solid lines indicate 68% C.L. regions. Note that the analyzed data are not independent.

---

[2] Palladino *et al.* [253] do not state their result as a ratio between the neutrino flavors, so that it cannot be compared in this way.

9.2 Implications of the Measurement Results

The effort needed to establish the presence of a cosmic neutrino flux with the IceCube detector was immense. Nevertheless, the cosmic neutrinos are a significant addition to the family of high-energy particles in the Universe. This is evident from fig. 9.1, which compares the diffuse neutrino flux as measured in this work with measurements of the diffuse extragalactic γ-ray background and the flux of ultra-high-energy cosmic rays. In fact, the energy carried by the cosmic neutrino flux around 100 TeV matches that of the γ-ray background around 100 GeV and that of the cosmic-ray flux around 1 EeV. This alone motivates to investigate the nature of the cosmic neutrino flux further.

The measurements presented in this work do not allow to make definitive statements on the origin of the cosmic neutrino flux. However, they constitute the most precise constraints on the properties of the flux obtained so far, and thus allow to draw some first conclusions.

The data are well described by a model that assumes an isotropic flux of cosmic neutrinos. This suggests that at least part of the flux has extragalactic origins; the non-observation of any significant directional clustering of events in [20] further supports this interpretation.

If the cosmic neutrinos are in fact produced entirely in extragalactic sources, their energy spectrum, measured as $E^{-2.50\pm0.09}$, is significantly steeper than expected in the benchmark scenario of an E^{-2}-flux. In fact, in a scenario where the neutrinos are produced in interactions of cosmic rays with matter, the associated flux of gamma rays would exceed the measured diffuse extragalactic γ-ray flux, provided the source environment is sufficiently thin to gamma rays and the soft spectrum continues to lower energies [147]. Thus, the coincident observation of the extragalactic γ-ray background [143] and the cosmic neutrino flux challenge this scenario. Furthermore, the steep spectral index implies that a direct connection to ultra-high-energy cosmic rays is unlikely, even though the normalization of the cosmic neutrino flux is close to the Waxman–Bahcall upper bound [45, 139, 140].

On the other hand, a contribution to the cosmic neutrino flux from sources in the Milky Way is not excluded.[3] The results obtained with the *north-south* model suggest that it might be possible to explain the total signal with a soft galactic component (dominating in the southern sky, where the best-fit spectral index is $\gamma = 2.56^{+0.11}_{-0.12}$) and a harder extragalactic component (dominating in the northern sky, where the best-fit spectral index is $\gamma = 2.0^{+0.3}_{-0.4}$). The result is inconclusive; a dedicated analysis based on a realistic model of the flux expected from the Milky Way could investigate this possibility further.

---

[3] Note that the entire flux from the region of the galactic center cannot be attributed to a single source though [254].

The measurements of the flavor composition of the cosmic neutrino flux presented in this work are in agreement with standard expectations for the neutrino production and propagation. The hypothesis of a flux consisting of only one flavor at Earth, which would be indicative of exotic physics, can be rejected with high confidence. Furthermore, it was possible for the first time to constrain the flavor composition at the *sources* of the flux, namely to disfavor the production of a pure electron neutrino flux. This implies that the production of the cosmic neutrinos at their sources is not dominated by the decay of neutrons.

9.3 Outlook

The data analyzed in this work represent only a small fraction of the data that the IceCube detector is expected to collect during its time of operation. While efforts to identify the sources of the cosmic neutrino flux will continue, there is no guarantee that these efforts will be successful. It is hence interesting to investigate how the constraints on the energy spectrum and flavor composition obtained with the analysis presented here will improve with time.

The projections presented in the following were obtained using the two most recently developed event selections, namely those of the event samples H2 and T2. The corresponding simulation data were scaled up to mimic the collection of additional data and the analysis outlined in chapter 7 was repeated, using the Asimov data set (see section 7.2). An operation time of the full IceCube detector between 6 and 20 years was assumed.[4] Unless noted otherwise, the cosmic neutrino flux is assumed to follow the energy spectrum measured in this work (see eq. 8.1 and 8.2) and a flavor composition of $\nu_e : \nu_\mu : \nu_\tau = 1 : 1 : 1$ at Earth.

Figure 9.4 shows projected constraints on the energy spectrum of

---

[4] Four years of full detector data are already recorded. An operation time of 10-12 years is very likely; an operation for 20 years is viable, though not secured.

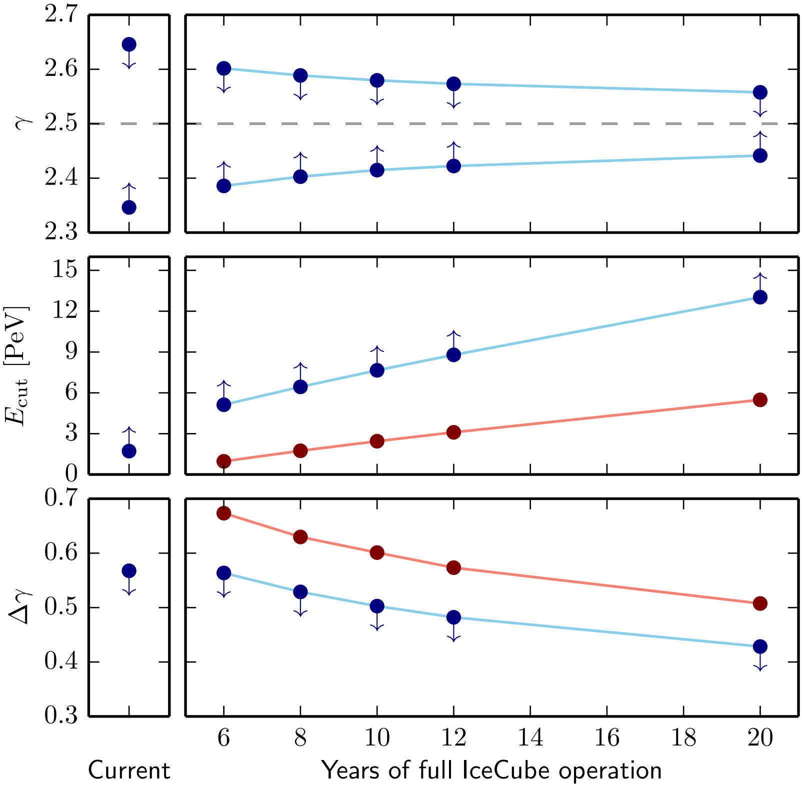

Figure 9.4 — *Projected Constraints on the Energy Spectrum.* Shown in blue are current and projected median 90% C.L. limits on the spectral index γ (*power law* model, top panel), the cut-off energy E_{cut} (*power law + cut-off* model, center panel), and the difference between the spectral indices of two power laws that contribute to the flux equally at 100 TeV, $\Delta\gamma$ (*two power laws* model, bottom panel). The projected limits are obtained with the Asimov data set, assuming the best-fit parameter values of the *power law* model. In addition, the red lines in the two lower panels show the values of E_{cut} and $\Delta\gamma$ that would have to be realized to be able to reject the *power law* model with 95% C.L. in 50% of the cases, again obtained with the Asimov data set and assuming a χ^2-distribution for the test statistic.

the cosmic neutrino flux. Assuming that the *power law* model correctly describes the neutrino spectrum, the projected constraints on the spectral index are $\gamma = 2.50 \pm 0.08$ at 90% confidence level for 10 years of data. Likewise, it will be possible to exclude an exponential cut-off at energies less than 7.7 PeV, as well as the existence of two components with a spectral difference greater than 0.5, assuming that both components contribute equally to the flux at 100 TeV. Given the current limits, the projected sensitivities to an exponential cut-off or a spectral break (red lines) indicate that a significant detection of a deviation from the *power law* model, based on the energy spectrum alone, appears unlikely. Indications for the presence of a cut-off might be obtainable if the cut-off energy is smaller than ~ 5 PeV.

Figure 9.5 shows the projected constraints on the fraction of electron neutrinos in the cosmic neutrino flux, adopting again the requirement that the flux of ν_μ and ν_τ be equal at Earth (*2-flavor* model). Assuming a true fraction of $f_e = 0.33$, the projected constraints with 10 years of data are $f_e = 0.33^{+0.13}_{-0.09}$ at 90% confidence level. This result indicates that a distinction between the pion-decay source scenario

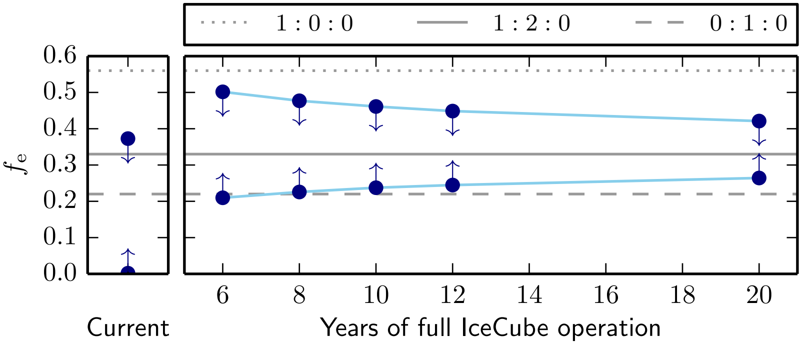

Figure 9.5 — *Projected Constraints on the Electron Neutrino Fraction.* Shown in blue are current and projected median 90% C.L. limits on the electron neutrino fraction of the cosmic neutrino flux in the *2-flavor* model. The gray lines indicate fractions expected for three different source scenarios. Note that the current best fit is $f_e = 0.18$, while the projected constraints are obtained with the Asimov data set, assuming $f_e = 0.33$ and the best-fit parameter values of the *power law* model.

($\nu_e : \nu_\mu : \nu_\tau = 1 : 2 : 0$ at the source) and the muon-damped source scenario ($\nu_e : \nu_\mu : \nu_\tau = 0 : 1 : 0$) is possible within the timescale considered here, provided either of these scenarios is true.

Finally, fig. 9.6 shows a projection of the constraints on the flavor composition for 10 years of data in the *3-flavor* model. In agreement with the results on the electron neutrino fraction in the *2-flavor* model, the result indicates that a distinction between the different source scenarios appears possible. However, a degeneracy with respect to the ν_τ-fraction of the flux remains.

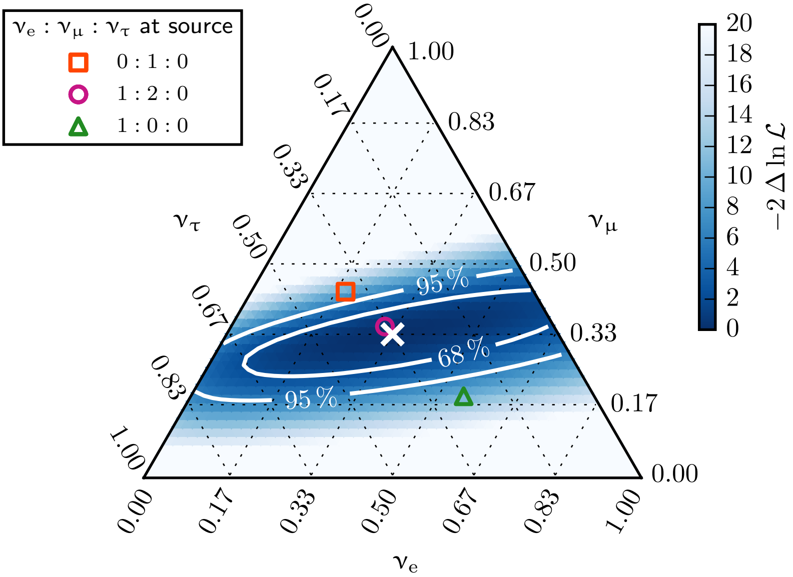

Figure 9.6 — *Projected Constraints on the Flavor Composition.*
Projected constraints on the flavor composition of the cosmic neutrino flux with 10 years of data from the full IceCube detector, in the *3-flavor* model (*cf.* fig. 8.14). The constraints are obtained with the Asimov data set, assuming a composition of $\nu_e : \nu_\mu : \nu_\tau = 1 : 1 : 1$ at Earth (white '×') and the best-fit parameter values of the *power law* model. The compositions for three different source scenarios are indicated.

The above improvements can be achieved simply by collecting more data and applying the analysis presented in this work. Several improvements are imaginable beyond that. For instance, at sufficiently high energies, it is possible to separate neutrino-induced shower events from the atmospheric muon background also at the boundary of the instrumented volume, thus increasing the effective detector volume for this type of events [255]. The measurement of the flavor composition would strongly benefit from the identification of tau neutrinos. However, the currently most sensitive search for tau neutrinos only finds an upper limit on the ν_τ flux [256]. As more data become available, in particular those with right-ascension information, the analysis can be improved by including anisotropic models that are more realistic than the *north-south* model. Lastly, as already mentioned in section 3.1.3, the flavor composition of the sources likely depends on the neutrino energy. With more data, it will be possible to test for this hypothesis.

Looking further into the future, the recently formed IceCube-Gen2 Collaboration currently investigates the potential of an extension of the IceCube experiment [257]. The extension would consist of a deployment of additional strings around the IceCube detector with a larger inter-string spacing, thus increasing the instrumented volume from $1\,\mathrm{km}^3$ to up to $10\,\mathrm{km}^3$. While the primary goal of the extended detector would be to resolve the sources of the cosmic neutrino flux, it would also allow to probe the energy spectrum and flavor composition of the flux at higher energies and with more statistics.

CHAPTER 10

Conclusion

> *"In summary, it may be too early to speculate."*
>
> — FRANCIS HALZEN (2013) [258]

IN THE ABSENCE OF EVIDENCE for the association of the cosmic neutrino flux recorded with the IceCube experiment with any astrophysical objects, a precise characterization of the flux is essential to constrain the properties of the unknown sources, and thus represents the natural first step to ultimately identify them. Two principal characteristics of the flux are its energy spectrum and flavor composition. The present work provides the most precise measurements of these properties that have been obtained so far. This was achieved by combining and analyzing, for the first time, multiple available data sets taken with the IceCube experiment, both during the construction phase and with the completed detector.

A forward-folding likelihood fit that employs specific models for atmospheric backgrounds and the cosmic neutrino flux was used to analyze the combined data. The models of Honda *et al.* [224] and Enberg *et al.* [223] were used to describe the background of conventional and prompt atmospheric neutrinos, respectively, where the absolute normalization of the flux was left to float freely in the analysis. Systematic uncertainties, such as the absolute energy calibration scale, were parametrized and allowed to vary in the fit as nuisance parameters. Different models were tested for the cosmic neutrino flux.

First, to investigate the energy spectrum, the cosmic neutrino flux was assumed to be isotropic and to equally consist of electron, muon, and tau neutrinos. Good agreement with the data was achieved for the *power law* model, with a best-fit spectral index of $\gamma = 2.50 \pm 0.09$

between neutrino energies of 25 TeV and 2.8 PeV. This value contrasts with the often-quoted benchmark value of $\gamma = 2$ at the level of 3.8 standard deviations ($p = 0.0066\%$). Two alternative, more complex spectral shapes were tested with the *power law + cut-off* and the *two power laws* model; however, neither resulted in a better description of the data. The results of the *differential* model suggest that an excess of events with energies around 30 TeV contributes to the steepness of the spectrum (see fig. 8.11).

Dropping the assumption of isotropy, the results obtained with the *north-south* model indicate that the cosmic neutrino flux follows a harder spectrum in the northern hemisphere ($\gamma = 2.0^{+0.3}_{-0.4}$) than in the southern hemisphere ($\gamma = 2.56^{+0.11}_{-0.12}$). However, the statistical significance of this discrepancy is very low ($p = 13\%$). Future observations are required to reveal whether it is caused by a physical effect.

Finally, the flavor composition of the cosmic neutrino flux was investigated in a *2-flavor* model and a *3-flavor* model. In both models, it was again assumed that the cosmic neutrino flux is isotropic, and that all of its flavor components follow the same energy spectrum, namely a power law. The *2-flavor* model corresponds to a scenario in which standard neutrino oscillations transform the cosmic neutrino flux during propagation. Under this constraint, the fraction of electron neutrinos in the cosmic neutrino flux at Earth was measured as $(18\pm11)\%$. The *3-flavor* model provides a more general test, the results were presented in fig. 8.14. A scenario in which only electron neutrinos are produced at the sources was disfavored with a significance of 3.6 standard deviations ($p = 0.014\%$). Other benchmark scenarios for the flavor composition were found to be compatible with the data.

The developed analysis framework can easily be extended to incorporate new data or to test different models. An outlook on results that can be obtained in the foreseeable future was presented, showing the improvement in precision in the measurement of the energy spectrum and flavor composition of the cosmic neutrino flux that can be achieved during the operation time of the IceCube experiment.

However, we should also brace for the unforeseen. With the discovery of a high-energy cosmic neutrino flux, a new field of research has been initiated: high-energy neutrino astronomy. So far, we have only glimpsed the tip of the iceberg, and the present work represents only one of the first steps to understand these new cosmic messengers, and what they may tell us about the cataclysmic processes that create them. As with any new window to the cosmos, there is no way of knowing what we may see through it.

Appendix A

Time Consumption of Muon Background Simulation

The correct representation of the enormous background of atmospheric muons in the IceCube detector requires the simulation of at least as many atmospheric air showers (including the subsequent muon propagation and detector simulation) as are naturally occurring during the data taking period. The statistical power of simulation data can be expressed as an equivalent live time, *i.e.* the time that an experiment would have to run for the number of simulated air showers to occur.

Often, weighted simulation data are produced, *i.e.* the primary cosmic rays are generated with arbitrary rather than natural frequencies, and are weighted accordingly. In this case, the live time of the simulation data is a function of the type and energy of the primary cosmic ray. Prior to this study, the muon background simulation for IceCube was mostly generated with an energy spectrum harder than that of cosmic rays, to achieve sufficient statistics at high energies more quickly. As a result, the equivalent live time of the simulation data decreased with decreasing energy, leading to an increasingly uncertain prediction of the muon background towards lower energies. The study presented here was performed to investigate the feasibility to produce muon background simulation with an equivalent live time of at least one year above a primary cosmic-ray energy of 10 TeV, as typically required for searches of a diffuse flux of neutrinos that are based on shower-like events. The result of the study was that the generation spectrum in the simulation must be adapted to match the cosmic-ray flux better in order to achieve this goal within a reasonable time. While the study was performed with the 79-string detector configuration of IceCube, its implications are valid also for the completed detector.

To determine the equivalent live time of simulation data, a model of the cosmic-ray flux and its composition is required. At the time of this study, the poly-gonato model [259] was widely used in the Ice-

Cube Collaboration.[1] While the poly-gonato model predicts the flux of all atomic nuclei up to uranium, the total flux is represented by five nuclei in IceCube simulations: hydrogen (^{1}H), helium (^{4}He), nitrogen (^{14}N, representative for all nuclei with $3 \leq Z \leq 9$), aluminium (^{27}Al, for $10 \leq Z \leq 25$), and iron (^{56}Fe, for $Z \geq 26$), where Z is the atomic charge number. Furthermore, the energy of secondary particles created in atmospheric air showers scales with the energy per nucleon of the primary cosmic ray, rather than with the total energy of the nucleus [83]. Therefore, the lower energy limit of the simulation is usually chosen proportional to the mass number of the simulated primary particle.

Figures A.1 and A.2 show the equivalent live time of simulation data as a function of the primary cosmic-ray energy for two different simulation settings, respectively, requiring at least one year of live time above 10 TeV *per nucleon* for all primary particles. The non-optimized simulation settings in fig. A.1 correspond to those mostly used prior to this study, while the optimized settings in fig. A.2 were inspired by this study. The optimization was achieved by adapting the spectral index and the fraction of primaries of the generation spectrum, as well as by omitting the simulation of primaries below the required energy threshold.

On a computer cluster with 1,000 computer cores, the time required to produce the simulation data corresponding to fig. A.1 and A.2 is 940 days and 210 days, respectively. This considerable improvement is visualized in fig. A.3, which shows the required production time as a function of the primary energy and the primary particle type for both simulation settings.

---

[1] Recently, the poly-gonato model was replaced by the model introduced in [214] ("H3a model"). The conclusions drawn from the study presented here do not depend on this distinction.

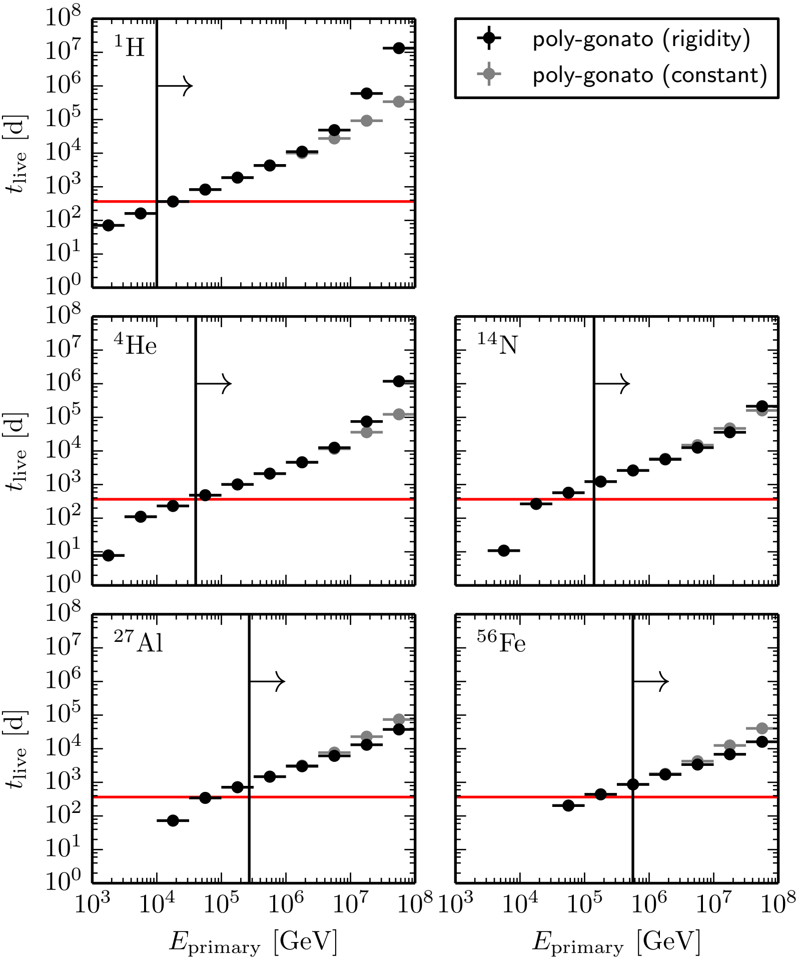

Figure A.1 — *Live Time of Simulation Data Before Optimization.* The equivalent live time of simulation data produced with non-optimized settings is shown for the five different simulated primaries, as a function of energy. The black and gray points assume two different versions of the poly-gonato cosmic-ray flux model [259], respectively (rigidity: rigidity-dependent cut-off; constant: constant composition for all energies). The red line marks one year of live time, while the black line marks the energy above which one year of live time was required.

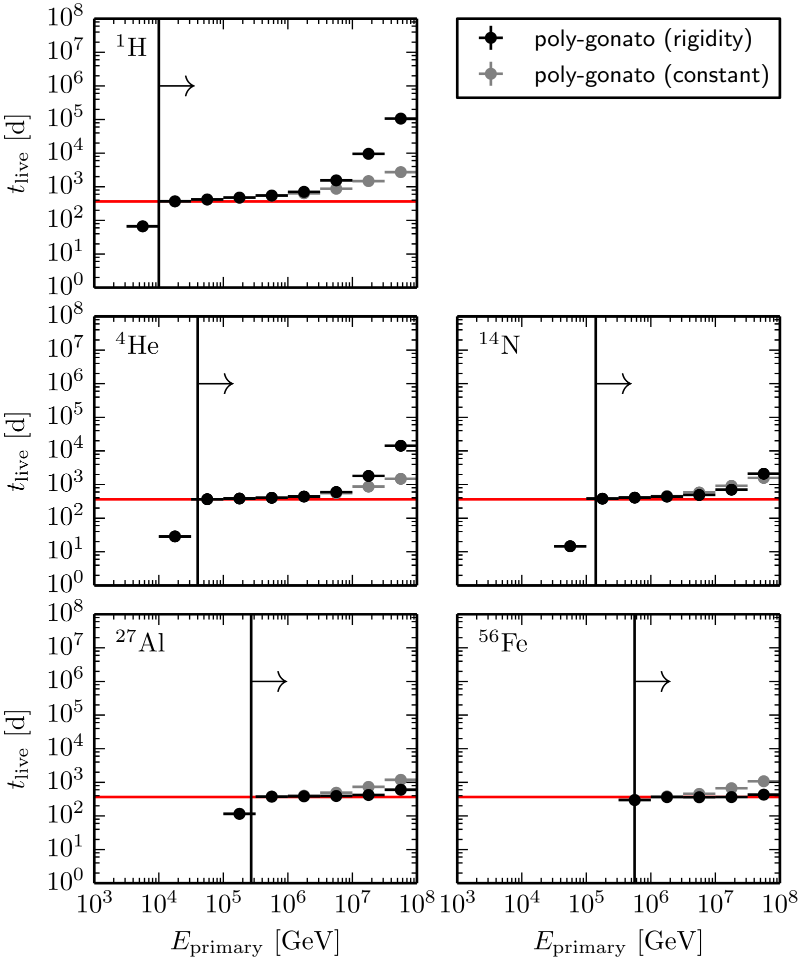

Figure A.2 — *Live Time of Simulation Data After Optimization.*
Same as fig. A.1, but for optimized simulation settings.

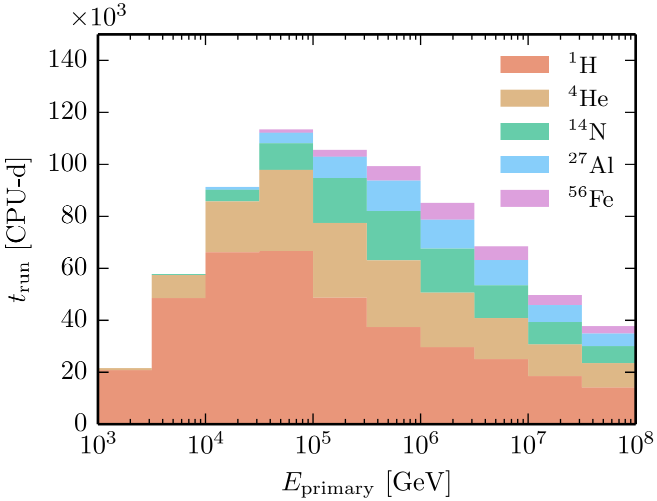

(a) Before Optimization.

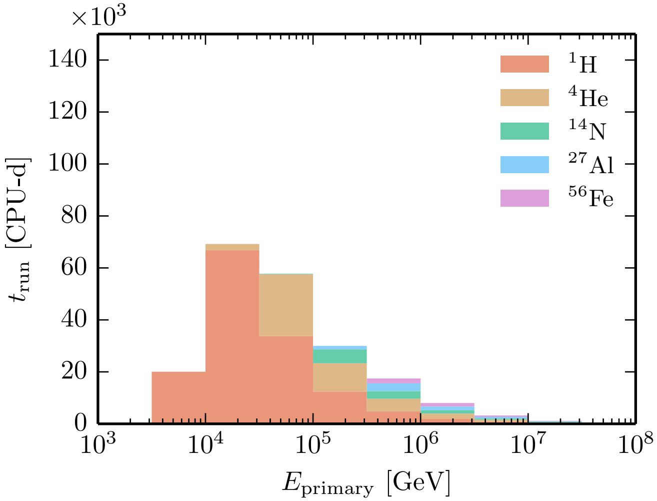

(b) After Optimization.

Figure A.3 — *Runtime of Simulation Production.* Time required to produce simulation data with equivalent live time of at least one year above 10 TeV / nucleon, with non-optimized (a) and optimized (b) settings.

APPENDIX B

Extension of Event Sample S2

With respect to the results presented in [25], the event sample S2 has been extended to lower energies. Specifically, while only events with deposited energies larger than 38 TeV were analyzed in [25], all events with deposited energies larger than 7 TeV are analyzed in this work. Several cross checks were performed by the author to ensure that this is possible. As an example, the distribution of the reconstructed deposited energy E'_{dep} at next-to-final event selection level is shown in fig. B.1. At this level, the event sample is still dominated by atmospheric muons. The simulation data describe the experimental data well above 7 TeV, giving confidence in the validity of the simulation data in this energy range. More detailed investigations of the data below deposited energies of 38 TeV can be found in [237].

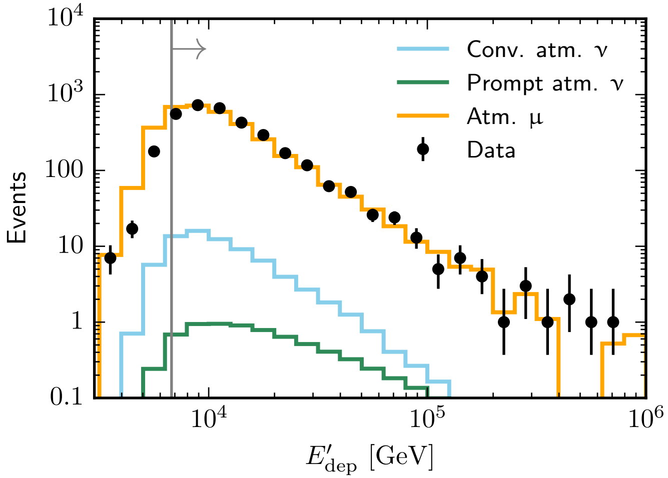

Figure B.1 — *Sample S2 at Next-to-Final Selection Level.* The distribution of the reconstructed deposited energy E'_{dep} is shown. The colored lines show default expectations for the atmospheric neutrino and muon backgrounds, the black points the experimental data. The energy range used for analysis is indicated by the arrow.

Appendix C

Binning of Observables

Table C.1 shows the binning of the observables in the different event samples as used in the likelihood analysis. Logarithmic bins are used for energy observables.

Table C.1 — *Binning of Observables.*

Sample	Observable	Bin edges
S1a	$\log_{10}(E'_{\mathrm{dep}}/\mathrm{GeV})$	$\{3.25 + 0.25k \mid k = 0..7\}$
S1b	$\log_{10}(E'_{\mathrm{dep}}/\mathrm{GeV})$	$\{5 + 0.25k \mid k = 0..8\}$
S2	$\log_{10}(E'_{\mathrm{dep}}/\mathrm{GeV})$	$\{3.83 + 0.17k \mid k = 0..19\}$
T1	$\log_{10}((\mathrm{d}E/\mathrm{d}X)'_{\mu}/\mathrm{a.u.})$	$\{-0.75 + 0.25k \mid k = 0..15\}$
T1	$\cos(\theta')$	$\{-1 + 0.1k \mid k = 0..10\}$
T2	$\log_{10}(E'_{\mu}/\mathrm{a.u.})$	$\{3.5 + 0.125k \mid k = 0..28\}$
T2	$\cos(\theta')$	$\{-1 + 0.1k \mid k = 0..11\}$
H1	$\log_{10}(E'_{\mathrm{dep}}/\mathrm{GeV})$	$\{4.33 + 0.17k \mid k = 0..16\}$
H1	$\cos(\theta')$	$\{-1, 0.2, 0.6, 1\}$
H2a	$\log_{10}(E'_{\mathrm{dep}}/\mathrm{GeV})$	$\{3 + 0.25k \mid k = 0..12\}$
H2b	$\log_{10}(E'_{\mathrm{dep}}/\mathrm{GeV})$	$\{3 + 0.5k \mid k = 0..5\}$
H2	$\cos(\theta')$	$\{-1, 0.2, 0.6, 1\}$
H2	q'_{track}	$\{0, 10, \infty\}$

Appendix D

Comparison of Results with Restored Event Samples

Figure D.1 shows a comparison of fit results obtained with individual event samples. Contrary to the comparison shown fig. 8.10, the event samples T2 and H2 were restored to their original size here.

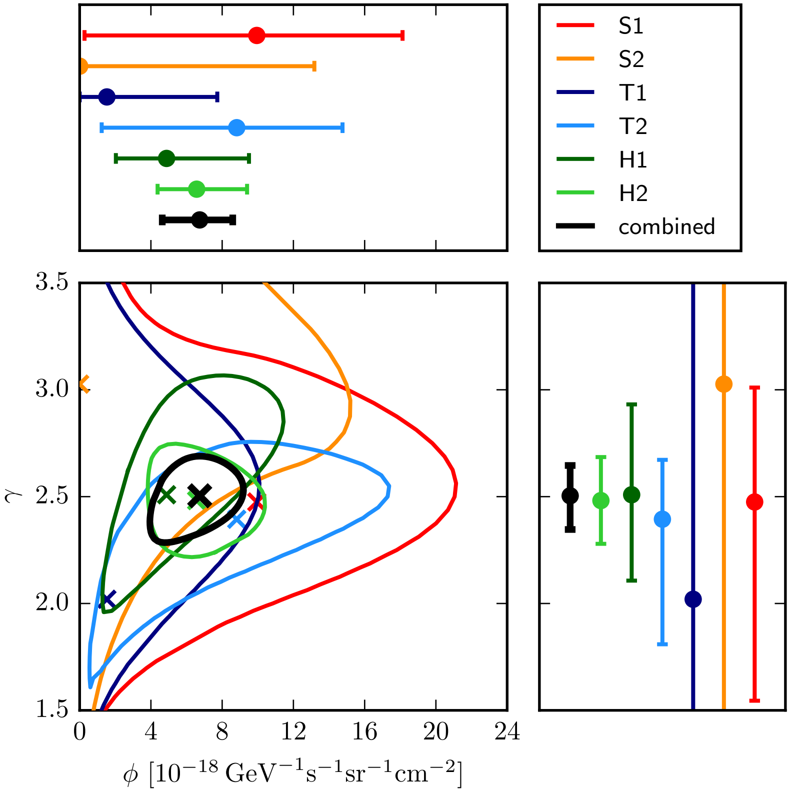

Figure D.1 — *Comparison of Results with Restored Event Samples.* Same as fig. 8.10, but without the modifications applied to event samples T2 and H2 (see section 6.2). Note that the results are not independent in this case.

Bibliography

[1] F. Reines. The Neutrino: From Poltergeist to Particle. Nobel Lecture (1995).
http://www.nobelprize.org/nobel_prizes/physics/laureates/1995/reines-lecture.html.

[2] M. Amenomori et al. The All-Particle Spectrum of Primary Cosmic Rays in the Wide Energy Range from 10^{14} to 10^{17} eV Observed with the Tibet-III Air-Shower Array. *Astrophysical Journal* **678** (2008), 1165–1179.
doi:10.1086/529514.

[3] T. Antoni et al. KASCADE measurements of energy spectra for elemental groups of cosmic rays: Results and open problems. *Astroparticle Physics* **24** (2005), 1–25.
doi:10.1016/j.astropartphys.2005.04.001.

[4] W. D. Apel et al. (KASCADE-Grande Collaboration). Kneelike Structure in the Spectrum of the Heavy Component of Cosmic Rays Observed with KASCADE-Grande. *Physical Review Letters* **107** (2011), 171104.
doi:10.1103/PhysRevLett.107.171104.

[5] S. F. Berezhnev et al. The Tunka-133 EAS Cherenkov light array: Status of 2011. *Nuclear Instruments and Methods A* **692** (2012), 98–105.
doi:10.1016/j.nima.2011.12.091.

[6] M. G. Aartsen et al. (IceCube Collaboration). Measurement of the cosmic ray energy spectrum with IceTop-73. *Physical Review D* **88** (2013), 042004.
doi:10.1103/PhysRevD.88.042004.

[7] T. ABU-ZAYYAD ET AL. (TELESCOPE ARRAY COLLABORATION). The Cosmic Ray Energy Spectrum Observed with the Surface Detector of the Telescope Array Experiment. *Astrophysical Journal* **768** (2013), L1.
doi:10.1088/2041-8205/768/1/L1.

[8] A. AAB ET AL. (PIERRE AUGER COLLABORATION). The measurement of the energy spectrum of cosmic rays above 3×10^{17} eV with the Pierre Auger Observatory. In *Proceedings of the 33rd International Cosmic Ray Conference* (2013).
arXiv:1307.5059.

[9] F. REINES AND C. L. COWAN. Detection of the Free Neutrino. *Physical Review* **92** (1953), 830–831.
doi:10.1103/PhysRev.92.830.

[10] K. GREISEN. Cosmic Ray Showers. *Annual Review of Nuclear Science* **10** (1960), 63–108.
doi:10.1146/annurev.ns.10.120160.000431.

[11] F. REINES. Neutrino Interactions. *Annual Review of Nuclear Science* **10** (1960), 1–26.
doi:10.1146/annurev.ns.10.120160.000245.

[12] M. A. MARKOV. On High Energy Neutrino Physics. In *Proceedings, 10th International Conference on High-Energy Physics* (1960), 578.

[13] C. SPIERING. Towards high-energy neutrino astronomy. *European Physical Journal H* **37** (2012), 515–565.
doi:10.1140/epjh/e2012-30014-2.

[14] A. ROBERTS. The birth of high-energy neutrino astronomy: A personal history of the DUMAND project. *Reviews of Modern Physics* **64** (1992), 259–312.
doi:10.1103/RevModPhys.64.259.

[15] V. AYNUTDINOV ET AL. The Baikal neutrino experiment: Status, selected physics results, and perspectives. *Nuclear Instruments and Methods A* **588** (2008), 99–106.
doi:10.1016/j.nima.2008.01.011.

[16] M. Ageron et al. (ANTARES Collaboration). ANTARES: The first undersea neutrino telescope. *Nuclear Instruments and Methods A* **656** (2011), 11–38.
doi:10.1016/j.nima.2011.06.103.

[17] F. Halzen and J. G. Learned. High energy neutrino detection in deep polar ice. *Tech. Rep. MAD/PH/428; UH-511-659-88* (1988).
http://inspirehep.net/record/262563.

[18] E. Andres et al. (AMANDA Collaboration). The AMANDA neutrino telescope: principle of operation and first results. *Astroparticle Physics* **13** (2000), 1–20.
doi:10.1016/S0927-6505(99)00092-4.

[19] M. G. Aartsen et al. (IceCube Collaboration). Evidence for High-Energy Extraterrestrial Neutrinos at the IceCube Detector. *Science* **342** (2013), 1242856.
doi:10.1126/science.1242856.

[20] M. G. Aartsen et al. (IceCube Collaboration). Observation of High-Energy Astrophysical Neutrinos in Three Years of IceCube Data. *Physical Review Letters* **113** (2014), 101101.
doi:10.1103/PhysRevLett.113.101101.

[21] M. G. Aartsen et al. (IceCube Collaboration). Atmospheric and astrophysical neutrinos above 1 TeV interacting in IceCube. *Physical Review D* **91** (2015), 022001.
doi:10.1103/PhysRevD.91.022001.

[22] M. G. Aartsen et al. (IceCube Collaboration). Evidence for Astrophysical Muon Neutrinos from the Northern Sky from IceCube. Submitted to *Physical Review Letters* (2015).

[23] M. G. Aartsen et al. (IceCube Collaboration). Search for a diffuse flux of astrophysical muon neutrinos with the IceCube 59-string configuration. *Physical Review D* **89** (2014), 062007.
doi:10.1103/PhysRevD.89.062007.

[24] M. G. Aartsen et al. (IceCube Collaboration). Search for neutrino-induced particle showers with IceCube-40. *Physical Review D* **89** (2014), 102001.
doi:10.1103/PhysRevD.89.102001.

[25] M. G. Aartsen et al. (IceCube Collaboration). Search for diffuse astrophysical neutrinos with cascade events in the IceCube-59 detector. In *Proceedings of the 33rd International Cosmic Ray Conference* (2013).
arXiv:1309.7003.

[26] M. G. Aartsen et al. (IceCube Collaboration). Searches for Extended and Point-like Neutrino Sources with Four Years of IceCube Data. *Astrophysical Journal* **796** (2014), 109.
doi:10.1088/0004-637X/796/2/109.

[27] M. G. Aartsen et al. (IceCube Collaboration). Search for Prompt Neutrino Emission from Gamma-Ray Bursts with IceCube. *Astrophysical Journal Letters* **805** (2015), L5.
doi:10.1088/2041-8205/805/1/L5.

[28] M. G. Aartsen et al. (IceCube Collaboration). Searches for small-scale anisotropies from neutrino point sources with three years of IceCube data. *Astroparticle Physics* **66** (2015), 39–52.
doi:10.1016/j.astropartphys.2015.01.001.

[29] M. G. Aartsen et al. (IceCube Collaboration). Searches for Time Dependent Neutrino Sources with IceCube Data from 2008 to 2012. Submitted to *Astrophysical Journal* (2015).
arXiv:1503.00598.

[30] T. Glüsenkamp for the IceCube Collaboration. Analysis of the cumulative neutrino flux from Fermi-LAT blazar populations using 3 years of IceCube data. In *Proceedings of the Roma International Conference on Astroparticle Physics* (2014).
arXiv:1502.03104.

[31] D. Hooper et al. Measuring the spectra of high energy neutrinos with a kilometer-scale neutrino telescope. *Physical Review D* **67** (2003), 013001.
doi:10.1103/PhysRevD.67.013001.

[32] J. F. Beacom et al. Measuring flavor ratios of high-energy astrophysical neutrinos. *Physical Review D* **68** (2003), 093005.
doi:10.1103/PhysRevD.68.093005. See erratum [33].

[33] J. F. Beacom et al. Erratum: Measuring flavor ratios of high-energy astrophysical neutrinos. *Physical Review D* **72** (2005), 019901.
doi:10.1103/PhysRevD.72.019901.

[34] P. Lipari, M. Lusignoli and D. Meloni. Flavor composition and energy spectrum of astrophysical neutrinos. *Physical Review D* **75** (2007), 123005.
doi:10.1103/PhysRevD.75.123005.

[35] S. Choubey and W. Rodejohann. Flavor composition of ultrahigh energy neutrinos at source and at neutrino telescopes. *Physical Review D* **80** (2009), 113006.
doi:10.1103/PhysRevD.80.113006.

[36] M. G. Aartsen et al. (IceCube Collaboration). Flavor Ratio of Astrophysical Neutrinos above 35 TeV in IceCube. *Physical Review Letters* **114** (2015), 171102.
doi:10.1103/PhysRevLett.114.171102.

[37] S. Weinberg. *Gravitation and Cosmology: Principles and Applications of the General Theory of Relativity* (John Wiley & Sons, 1972).

[38] J. N. Bahcall and R. Ulrich. Solar models, neutrino experiments, and helioseismology. *Reviews of Modern Physics* **60** (1988), 297–372.
doi:10.1103/RevModPhys.60.297.

[39] L. M. Krauss, S. L. Glashow and D. N. Schramm. Antineutrino astronomy and geophysics. *Nature* **310** (1984), 191–198.
doi:10.1038/310191a0.

[40] F. VISSANI AND G. PAGLIAROLI. The diffuse supernova neutrino background: expectations and uncertainties derived from SN1987A. *Astronomy and Astrophysics* **528** (2011), L1. doi:10.1051/0004-6361/201016109.

[41] T. K. GAISSER AND M. HONDA. Flux of Atmospheric Neutrinos. *Annual Review of Nuclear and Particle Science* **52** (2002), 153–199. doi:10.1146/annurev.nucl.52.050102.090645.

[42] F. W. STECKER ET AL. High-energy neutrinos from active galactic nuclei. *Physical Review Letters* **66** (1991), 2697–2700. doi:10.1103/PhysRevLett.66.2697.

[43] F. W. STECKER ET AL. Erratum: "High-energy neutrinos from active galactic nuclei". *Physical Review Letters* **69** (1992), 2738. doi:10.1103/PhysRevLett.69.2738.

[44] F. W. STECKER. Note on high-energy neutrinos from active galactic nuclei cores. *Physical Review D* **72** (2005), 107301. doi:10.1103/PhysRevD.72.107301.

[45] J. N. BAHCALL AND E. WAXMAN. High energy astrophysical neutrinos: The upper bound is robust. *Physical Review D* **64** (2001), 023002. doi:10.1103/PhysRevD.64.023002.

[46] M. AHLERS ET AL. GZK neutrinos after the Fermi-LAT diffuse photon flux measurement. *Astroparticle Physics* **34** (2010), 106–115. doi:10.1016/j.astropartphys.2010.06.003.

[47] J. G. LEARNED AND K. MANNHEIM. High-Energy Neutrino Astrophysics. *Annual Review of Nuclear and Particle Science* **50** (2000), 679–749. doi:10.1146/annurev.nucl.50.1.679.

[48] E. FERMI. Versuch einer Theorie der β-Strahlen. *Zeitschrift für Physik* **88** (1934), 161–177. doi:10.1007/BF01351864.

[49] E. C. G. Sudarshan and R. E. Marshak. Chirality Invariance and the Universal Fermi Interaction. *Physical Review* **109** (1958), 1860–1862.
doi:10.1103/PhysRev.109.1860.2.

[50] R. P. Feynman and M. Gell-Mann. Theory of the Fermi Interaction. *Physical Review* **109** (1958), 193–198.
doi:10.1103/PhysRev.109.193.

[51] K. A. Olive et al. (Particle Data Group). 2014 Review of Particle Physics. *Chinese Physics C* **38** (2014), 090001.
doi:10.1088/1674-1137/38/9/090001.

[52] K. N. Abazajian et al. Cosmological and astrophysical neutrino mass measurements. *Astroparticle Physics* **35** (2011), 177–184.
doi:10.1016/j.astropartphys.2011.07.002.

[53] G. Drexlin et al. Current Direct Neutrino Mass Experiments. *Advances in High Energy Physics* **2013** (2013), 293986.
doi:10.1155/2013/293986.

[54] M. Goldhaber, L. Grodzins and A. W. Sunyar. Helicity of Neutrinos. *Physical Review* **109** (1958), 1015–1017.
doi:10.1103/PhysRev.109.1015.

[55] J. C. Palathingal. Helicity of Antineutrinos Emitted by Nuclei. *Physical Review Letters* **24** (1970), 524–526.
doi:10.1103/PhysRevLett.24.524.

[56] J. A. Formaggio and G. P. Zeller. From eV to EeV: Neutrino cross sections across energy scales. *Reviews of Modern Physics* **84** (2012), 1307–1341.
doi:10.1103/RevModPhys.84.1307.

[57] S. L. Glashow. Resonant Scattering of Antineutrinos. *Physical Review* **118** (1960), 316–317.
doi:10.1103/PhysRev.118.316.

[58] A. Gazizov and M. Kowalski. ANIS: High energy neutrino generator for neutrino telescopes. *Computer Physics Communications* **172** (2005), 203–213.
doi:10.1016/j.cpc.2005.03.113.

[59] B. Pontecorvo. Neutrino experiments and the problem of conservation of leptonic charge. *Journal of Experimental and Theoretical Physics* **26** (1968), 984–988.
http://jetp.ac.ru/cgi-bin/e/index/e/26/5/p984?a=list.

[60] R. Z. Funchal, B. Schmauch and G. Giesen. The Physics of Neutrinos. *Lecture notes*, Institut de Physique Théorique, CEA / Saclay (2013).

[61] G. Bellini et al. Neutrino Oscillations. *Advances in High Energy Physics* **2014** (2014), 191960.
doi:10.1155/2014/191960.

[62] M. C. Gonzalez-Garcia, M. Maltoni and T. Schwetz. Updated fit to three neutrino mixing: status of leptonic CP violation. *Journal of High Energy Physics* **11** (2014), 052.
doi:10.1007/JHEP11(2014)052.

[63] C. Bemporad, G. Gratta and P. Vogel. Reactor-based neutrino oscillation experiments. *Reviews of Modern Physics* **74** (2002), 297–328.
doi:10.1103/RevModPhys.74.297.

[64] Y. Abe et al. (Double Chooz Collaboration). Indication of Reactor $\bar{\nu}_e$ Disappearance in the Double Chooz Experiment. *Physical Review Letters* **108** (2012), 131801.
doi:10.1103/PhysRevLett.108.131801.

[65] F. P. An et al. (Daya Bay Collaboration). Observation of Electron-Antineutrino Disappearance at Daya Bay. *Physical Review Letters* **108** (2012), 171803.
doi:10.1103/PhysRevLett.108.171803.

[66] G. Danby et al. Observation of High-Energy Neutrino Reactions and the Existence of Two Kinds of Neutrinos. *Physical Review Letters* **9** (1962), 36–44.
doi:10.1103/PhysRevLett.9.36.

[67] K. Kodama et al. (DONUT Collaboration). Observation of tau neutrino interactions. *Physics Letters B* **504** (2001), 218–224.
doi:10.1016/S0370-2693(01)00307-0.

[68] N. Agafonova et al. (OPERA Collaboration). Evidence for $\nu_\mu \to \nu_\tau$ appearance in the CNGS neutrino beam with the OPERA experiment. *Physical Review D* **89** (2014), 051102.
doi:10.1103/PhysRevD.89.051102.

[69] K. Abe et al. (T2K Collaboration). Observation of Electron Neutrino Appearance in a Muon Neutrino Beam. *Physical Review Letters* **112** (2014), 061802.
doi:10.1103/PhysRevLett.112.061802.

[70] K. Hirata et al. Observation of a neutrino burst from the supernova SN1987A. *Physical Review Letters* **58** (1987), 1490–1493.
doi:10.1103/PhysRevLett.58.1490.

[71] R. M. Bionta et al. Observation of a neutrino burst in coincidence with supernova 1987A in the Large Magellanic Cloud. *Physical Review Letters* **58** (1987), 1494–1496.
doi:10.1103/PhysRevLett.58.1494.

[72] E. N. Alekseev et al. Possible detection of a neutrino signal on 23 February 1987 at the Baksan underground scintillation telescope of the Institute of Nuclear Research. *Journal of Experimental and Theoretical Physics Letters* **45** (1987), 589–592.
http://www.jetpletters.ac.ru/ps/1245/article_18825.shtml.

[73] M. Aglietta et al. On the Event Observed in the Mont Blanc Underground Neutrino Observatory during the Occurrence of Supernova 1987a. *Europhysics Letters* **3** (1987), 1315–1320.
doi:10.1209/0295-5075/3/12/011.

[74] W. D. Arnett et al. Supernova 1987A. *Annual Review of Astronomy and Astrophysics* **27** (1989), 629–700.
doi:10.1146/annurev.aa.27.090189.003213.

[75] E. N. Alekseev et al. Detection of the neutrino signal from SN 1987A in the LMC using the INR Baksan underground scintillation telescope. *Physics Letters B* **205** (1988), 209–214.
doi:10.1016/0370-2693(88)91651-6.

[76] K. Kotake, K. Sato and K. Takahashi. Explosion mechanism, neutrino burst and gravitational wave in core-collapse supernovae. *Reports on Progress in Physics* **69** (2006), 971–1143.
doi:10.1088/0034-4885/69/4/R03.

[77] R. Davis, D. S. Harmer and K. C. Hoffman. Search for Neutrinos from the Sun. *Physical Review Letters* **20** (1968), 1205–1209.
doi:10.1103/PhysRevLett.20.1205.

[78] R. Davis. A Review of the Homestake Solar Neutrino Experiment. *Progress in Particle and Nuclear Physics* **32** (1994), 13–32.
doi:10.1016/0146-6410(94)90004-3.

[79] S. Fukuda et al. (Super-Kamiokande Collaboration). The Super-Kamiokande detector. *Nuclear Instruments and Methods in Physics Research A* **501** (2003), 418–462.
doi:10.1016/S0168-9002(03)00425-X.

[80] Y. Fukuda et al. (Super-Kamiokande Collaboration). Measurements of the Solar Neutrino Flux from Super-Kamiokande's First 300 Days. *Physical Review Letters* **81** (1998), 1158–1162.
doi:10.1103/PhysRevLett.81.1158.

[81] J. Boger et al. (SNO Collaboration). The Sudbury Neutrino Observatory. *Nuclear Instruments and Methods A* **449** (2000), 172–207.
doi:doi:10.1016/S0168-9002(99)01469-2.

[82] Q. R. Ahmad (SNO Collaboration). Direct Evidence for Neutrino Flavor Transformation from Neutral-Current Interactions in the Sudbury Neutrino Observatory. *Physical Review Letters* **89** (2002), 011301.
doi:10.1103/PhysRevLett.89.011301.

[83] T. K. Gaisser. *Cosmic Rays and Particle Physics* (Cambridge University Press, 1990).

[84] C. V. Achar et al. Detection of muons produced by cosmic ray neutrinos deep underground. *Physics Letters* **18** (1965), 196–199.
doi:10.1016/0031-9163(65)90712-2.

[85] F. Reines et al. Evidence for High-Energy Cosmic-Ray Neutrino Interactions. *Physical Review Letters* **15** (1965), 429–433.
doi:10.1103/PhysRevLett.15.429.

[86] Y. Fukuda et al. (Super-Kamiokande Collaboration). Evidence for Oscillation of Atmospheric Neutrinos. *Physical Review Letters* **81** (1998), 1562–1567.
doi:10.1103/PhysRevLett.81.1562.

[87] K. Daum et al. (Fréjus Collaboration). Determination of the atmospheric neutrino spectra with the Fréjus detector. *Zeitschrift für Physik C* **66** (1995), 417–428.
doi:10.1007/BF01556368.

[88] S. Adrián-Martínez et al. (ANTARES Collaboration). Measurement of the atmospheric ν_μ energy spectrum from 100 GeV to 200 TeV with the ANTARES telescope. *European Physical Journal C* **73** (2013), 2606.
doi:10.1140/epjc/s10052-013-2606-4.

[89] M. G. Aartsen et al. (IceCube Collaboration). Development of a general analysis and unfolding scheme and its application to measure the energy spectrum of atmospheric neutrinos with IceCube. *European Physical Journal C* **75** (2015), 116.
doi:10.1140/epjc/s10052-015-3330-z.

[90] M. G. Aartsen et al. (IceCube Collaboration). Measurement of the Atmospheric ν_e Flux in IceCube. *Physical Review Letters* **110** (2013), 151105.
doi:10.1103/PhysRevLett.110.151105.

[91] S. Hannestad. Primordial Neutrinos. *Annual Review of Nuclear and Particle Science* **56** (2006), 137–161.
doi:10.1146/annurev.nucl.56.080805.140548.

[92] A. Ringwald. Prospects for the direct detection of the cosmic neutrino background. *Nuclear Physics A* **827** (2009), 501c–506c. doi:10.1016/j.nuclphysa.2009.05.109.

[93] J. F. Beacom. The Diffuse Supernova Neutrino Background. *Annual Review of Nuclear and Particle Science* **60** (2010), 439–462.
doi:10.1146/annurev.nucl.010909.083331.

[94] G. Bertone, D. Hooper and J. Silk. Particle dark matter: evidence, candidates and constraints. *Physics Reports* **405** (2005), 279–390.
doi:10.1016/j.physrep.2004.08.031.

[95] J. Silk, K. Olive and M. Srednicki. The photino, the sun, and high-energy neutrinos. *Physical Review Letters* **55** (1985), 257–259.
doi:10.1103/PhysRevLett.55.257.

[96] T. K. Gaisser, G. Steigman and S. Tilav. Limits on cold-dark-matter candidates from deep underground detectors. *Physical Review D* **34** (1986), 2206–2222.
doi:10.1103/PhysRevD.34.2206.

[97] G. Bertone et al. Neutrinos from dark matter annihilations at the galactic center. *Physical Review D* **70** (2004), 063503.
doi:10.1103/PhysRevD.70.063503.

[98] M. G. Aartsen et al. (IceCube Collaboration). Search for Dark Matter Annihilations in the Sun with the 79-String IceCube Detector. *Physical Review Letters* **110** (2013), 131302.
doi:10.1103/PhysRevLett.110.131302.

[99] L. Covi et al. Neutrino signals from dark matter decay. *Journal of Cosmology and Astroparticle Physics* **04** (2010), 017.
doi:10.1088/1475-7516/2010/04/017.

[100] A. Esmaili, A. Ibarra and O. L. G. Peres. Probing the stability of superheavy dark matter particles with high-energy neutrinos. *Journal of Cosmology and Astroparticle Physics* **11** (2012), 034.
doi:10.1088/1475-7516/2012/11/034.

[101] K. Murase and J. F. Beacom. Constraining very heavy dark matter using diffuse backgrounds of neutrinos and cascaded gamma rays. *Journal of Cosmology and Astroparticle Physics* **10** (2012), 043.
doi:10.1088/1475-7516/2012/10/043.

[102] D. Adams. *The Hitchhiker's Guide to the Galaxy* (Pan Books, London, 1979).

[103] D. V. Reames. Particle acceleration at the Sun and in the heliosphere. *Space Science Reviews* **90** (1999), 413–491.
doi:10.1023/A:1005105831781.

[104] M. Ackermann et al. (Fermi LAT Collaboration). Detection of the Characteristic Pion-Decay Signature in Supernova Remnants. *Science* **339** (2013), 807–811.
doi:10.1126/science.1231160.

[105] W. Baade and F. Zwicky. Cosmic Rays from Super-Novae. *Proceedings of the National Academy of Sciences of the United States of America* **20** (1934), 259–263.
doi:10.1073/pnas.20.5.259.

[106] W. Baade and F. Zwicky. Remarks on Super-Novae and Cosmic Rays. *Physical Review* **46** (1934), 76–77.
doi:10.1103/PhysRev.46.76.2.

[107] P. Blasi. The origin of galactic cosmic rays. *Astronomy and Astrophysics Review* **21** (2013), 70.
doi:10.1007/s00159-013-0070-7.

[108] J. K. Becker. High-energy neutrinos in the context of multimessenger astrophysics. *Physics Reports* **458** (2008), 173–246.
doi:10.1016/j.physrep.2007.10.006.

[109] L. A. Anchordoqui et al. High energy neutrinos from astrophysical accelerators of cosmic ray nuclei. *Astroparticle Physics* **29** (2008), 1–13.
doi:10.1016/j.astropartphys.2007.10.006.

[110] L. A. Anchordoqui et al. Neutrinos as a diagnostic of high energy astrophysical processes. *Physics Letters B* **621** (2005), 18–21.
doi:10.1016/j.physletb.2005.06.056.

[111] E. Fermi. On the Origin of the Cosmic Radiation. *Physical Review* **75** (1949), 1169–1174.
doi:10.1103/PhysRev.75.1169.

[112] J. G. Kirk and P. Schneider. On the acceleration of charged particles at relativistic shock fronts. *Astrophysical Journal* **315** (1987), 425–433.
doi:10.1086/165147.

[113] A. F. Heavens and L. O. Drury. Relativistic shocks and particle acceleration. *Monthly Notices of the Royal Astronomical Society* **235** (1988), 997–1009.
doi:10.1093/mnras/235.3.997.

[114] P. Chen, T. Tajima and Y. Takahashi. Plasma Wakefield Acceleration for Ultrahigh-Energy Cosmic Rays. *Physical Review Letters* **89** (2002), 161101.
doi:10.1103/PhysRevLett.89.161101.

[115] F.-Y. Chang et al. Magnetowave Induced Plasma Wakefield Acceleration for Ultrahigh Energy Cosmic Rays. *Physical Review Letters* **102** (2009), 111101.
doi:10.1103/PhysRevLett.102.111101.

[116] A. Lazarian et al. Turbulence, Magnetic Reconnection in Turbulent Fluids and Energetic Particle Acceleration. *Space Science Reviews* **173** (2012), 557–622.
doi:10.1007/s11214-012-9936-7.

[117] D. Giannios. UHECRs from magnetic reconnection in relativistic jets. *Monthly Notices Letters of the Royal Astronomical Society* **408** (2010), L46–L50.
doi:10.1111/j.1745-3933.2010.00925.x.

[118] L. O. Drury. First-order Fermi acceleration driven by magnetic reconnection. *Monthly Notices of the Royal Astronomical Society* **422** (2012), 2474–2476.
doi:10.1111/j.1365-2966.2012.20804.x.

[119] M. Yamada, R. Kulsrud and H. Ji. Magnetic reconnection. *Reviews of Modern Physics* **82** (2010), 603–664.
doi:10.1103/RevModPhys.82.603.

[120] K. Fang, K. Kotera and A. V. Olinto. Newly Born Pulsars as Sources of Ultrahigh Energy Cosmic Rays. *Astrophysical Journal* **750** (2012), 118.
doi:10.1088/0004-637X/750/2/118.

[121] J. P. Rachen and P. Mészáros. Photohadronic neutrinos from transients in astrophysical sources. *Physical Review D* **58** (1998), 123005.
doi:10.1103/PhysRevD.58.123005.

[122] M. Kachelriess and R. Tomàs. High-energy neutrino yields from astrophysical sources: Weakly magnetized sources. *Physical Review D* **74** (2006), 063009.
doi:10.1103/PhysRevD.74.063009.

[123] M. Kachelriess, S. Ostapchenko and R. Tomàs. High energy neutrino yields from astrophysical sources. II. Magnetized sources. *Physical Review D* **77** (2008), 023007.
doi:10.1103/PhysRevD.77.023007.

[124] W. Winter. Neutrinos from Cosmic Accelerators including Magnetic Field and Flavor Effects. *Advances in High Energy Physics* **2012** (2012), 586413.
doi:10.1155/2012/586413.

[125] S. R. Klein, R. E. Mikkelsen and J. Becker Tjus. Muon Acceleration in Cosmic-ray Sources. *Astrophysical Journal* **779** (2013), 106.
doi:10.1088/0004-637X/779/2/106.

[126] W. Winter, J. Becker Tjus and S. R. Klein. Impact of secondary acceleration on the neutrino spectra in gamma-ray bursts. *Astronomy and Astrophysics* **569** (2014), A58.
doi:10.1051/0004-6361/201423745.

[127] P. Keränen. Testing exotic neutrino-neutrino interactions with AGN neutrinos. *Physics Letters B* **417** (1998), 320–325.
doi:10.1016/S0370-2693(97)01405-6.

[128] K. C. Y. Ng and J. F. Beacom. Cosmic neutrino cascades from secret neutrino interactions. *Physical Review D* **90** (2014), 065035.
doi:10.1103/PhysRevD.90.065035.

[129] K. Ioka and K. Murase. IceCube PeV–EeV neutrinos and secret interactions of neutrinos. *Progress of Theoretical and Experimental Physics* **2014** (2014), 061E01.
doi:10.1093/ptep/ptu090.

[130] T. Kashti and E. Waxman. Astrophysical Neutrinos: Flavor Ratios Depend on Energy. *Physical Review Letters* **95** (2005), 181101.
doi:10.1103/PhysRevLett.95.181101.

[131] S. Hümmer et al. Energy dependent neutrino flavor ratios from cosmic accelerators on the Hillas plot. *Astroparticle Physics* **34** (2010), 205–224.
doi:10.1016/j.astropartphys.2010.07.003.

[132] J. F. Beacom et al. Decay of High-Energy Astrophysical Neutrinos. *Physical Review Letters* **90** (2003), 181301.
doi:10.1103/PhysRevLett.90.181301.

[133] P. Baerwald, M. Bustamante and W. Winter. Neutrino decays over cosmological distances and the implications for neutrino telescopes. *Journal of Cosmology and Astroparticle Physics* **10** (2012), 020.
doi:10.1088/1475-7516/2012/10/020.

[134] D. Hooper, D. Morgan and E. Winstanley. Lorentz and CPT invariance violation in high-energy neutrinos. *Physical Review D* **72** (2005), 065009.
doi:10.1103/PhysRevD.72.065009.

[135] K. Greisen. End to the Cosmic-Ray Spectrum? *Physical Review Letters* **16** (1966), 748–750.
doi:10.1103/PhysRevLett.16.748.

[136] G. T. Zatsepin and V. A. Kuz'min. Upper Limit of the Spectrum of Cosmic Rays. *Journal of Experimental and Theoretical Physics Letters* **4** (1966), 78.
http://www.jetpletters.ac.ru/ps/1624/article_24846.shtml.

[137] V. S. Beresinsky and G. T. Zatsepin. Cosmic rays at ultra high energies (neutrino?). *Physics Letters B* **28** (1969), 423–424.
doi:10.1016/0370-2693(69)90341-4.

[138] M. G. Aartsen et al. (IceCube Collaboration). Probing the origin of cosmic rays with extremely high energy neutrinos using the IceCube Observatory. *Physical Review D* **88** (2013), 112008.
doi:10.1103/PhysRevD.88.112008.

[139] E. Waxman and J. N. Bahcall. High energy neutrinos from astrophysical sources: An upper bound. *Physical Review D* **59** (1998), 023002.
doi:10.1103/PhysRevD.59.023002.

[140] E. Waxman. High Energy Cosmic Ray and Neutrino Astronomy. In *Astronomy at the Frontiers of Science* (edited by J.-P. Lasota) (Springer Netherlands, 2011). 43–68.
doi:10.1007/978-94-007-1658-2_3.

[141] K. Mannheim, R. J. Protheroe and J. P. Rachen. Cosmic ray bound for models of extragalactic neutrino production. *Physical Review D* **63** (2000), 023003.
doi:10.1103/PhysRevD.63.023003.

[142] K. MURASE AND J. F. BEACOM. Neutrino background flux from sources of ultrahigh-energy cosmic-ray nuclei. *Physical Review D* **81** (2010), 123001.
doi:10.1103/PhysRevD.81.123001.

[143] M. ACKERMANN ET AL. (FERMI LAT COLLABORATION). The spectrum of isotropic diffuse gamma-ray emission between 100 MeV and 820 GeV. *Astrophysical Journal* **799** (2015), 86.
doi:10.1088/0004-637X/799/1/86.

[144] V. BEREZINSKY ET AL. Restricting UHECRs and cosmogenic neutrinos with Fermi-LAT. *Physics Letters B* **695** (2011), 13–18.
doi:10.1016/j.physletb.2010.11.019.

[145] S. RAZZAQUE, P. MÉSZÁROS AND B. ZHANG. GeV and Higher Energy Photon Interactions in Gamma-Ray Burst Fireballs and Surroundings. *Astrophysical Journal* **613** (2004), 1072–1078.
doi:10.1086/423166.

[146] C. D. DERMER, E. RAMIREZ-RUIZ AND T. LE. Correlation of Photon and Neutrino Fluxes in Blazars and Gamma-Ray Bursts. *Astrophysical Journal Letters* **664** (2007), L67.
doi:10.1086/520638.

[147] K. MURASE, M. AHLERS AND B. C. LACKI. Testing the hadronuclear origin of PeV neutrinos observed with IceCube. *Physical Review D* **88** (2013), 121301.
doi:10.1103/PhysRevD.88.121301.

[148] A. M. HILLAS. The Origin of Ultra High Energy Cosmic Rays. *Annual Review of Astronomy and Astrophysics* **22** (1984), 425–444.
doi:10.1146/annurev.aa.22.090184.002233.

[149] K. V. PTITSYNA AND S. V. TROITSKY. Physical conditions in potential accelerators of ultra-high-energy cosmic rays: updated Hillas plot and radiation-loss constraints. *Physics-Uspekhi* **53** (2010), 691–701.
doi:10.3367/UFNe.0180.201007c.0723.

[150] F. Aharonian et al. (H.E.S.S. Collaboration). The H.E.S.S. Survey of the Inner Galaxy in Very High Energy Gamma Rays. *Astrophysical Journal* **636** (2006), 777–797. doi:10.1086/498013.

[151] A. Kappes et al. Potential Neutrino Signals from Galactic γ-Ray Sources. *Astrophysical Journal* **656** (2007), 870–878. doi:10.1086/508936.

[152] TeVCat Catalog. http://tevcat.uchicago.edu. Visited January 19, 2015.

[153] W. Bednarek, G. F. Burgio and T. Montaruli. Galactic discrete sources of high energy neutrinos. *New Astronomy Reviews* **49** (2005), 1–21. doi:10.1016/j.newar.2004.11.001.

[154] M. D. Kistler and J. F. Beacom. Guaranteed and prospective Galactic TeV neutrino sources. *Physical Review D* **74** (2006), 063007. doi:10.1103/PhysRevD.74.063007.

[155] M. Mandelartz and J. Becker Tjus. Prediction of the diffuse neutrino flux from cosmic ray interactions near supernova remnants. *Astroparticle Physics* **65** (2015), 80–100. doi:10.1016/j.astropartphys.2014.12.002.

[156] F. Halzen and A. Ó Murchadha. Neutrinos from cosmic ray accelerators in the Cygnus region of the galaxy. *Physical Review D* **76** (2007), 123003. doi:10.1103/PhysRevD.76.123003.

[157] B. M. Gaensler and P. O. Slane. The Evolution and Structure of Pulsar Wind Nebulae. *Annual Review of Astronomy and Astrophysics* **44** (2006), 17–47. doi:10.1146/annurev.astro.44.051905.092528.

[158] E. Amato, D. Guetta and P. Blasi. Signatures of high energy protons in pulsar winds. *Astronomy and Astrophysics* **402** (2003), 827–836. doi:10.1051/0004-6361:20030279.

[159] W. Bednarek. Neutrinos from the pulsar wind nebulae. *Astronomy and Astrophysics* **407** (2003), 1–6.
doi:10.1051/0004-6361:20030929.

[160] D. Guetta and E. Amato. Neutrino flux predictions for galactic plerions. *Astroparticle Physics* **19** (2003), 403–407.
doi:10.1016/S0927-6505(02)00221-9.

[161] S. Nagataki. High-Energy Neutrinos Produced by Interactions of Relativistic Protons in Shocked Pulsar Winds. *Astrophysical Journal* **600** (2004), 883–904.
doi:10.1086/380095.

[162] P. Blasi. Origin of very high- and ultra-high-energy cosmic rays. *Comptes Rendus Physique* **15** (2014), 329–338.
doi:10.1016/j.crhy.2014.02.008.

[163] F. Halzen and D. Hooper. High-energy neutrino astronomy: the cosmic ray connection. *Reports on Progress in Physics* **65** (2002), 1025–1078.
doi:10.1088/0034-4885/65/7/201.

[164] A. Mücke et al. BL Lac objects in the synchrotron proton blazar model. *Astroparticle Physics* **18** (2003), 593–613.
doi:10.1016/S0927-6505(02)00185-8.

[165] J. K. Becker, P. L. Biermann and W. Rhode. The diffuse neutrino flux from FR-II radio galaxies and blazars: A source property based estimate. *Astroparticle Physics* **23** (2005), 355–368.
doi:10.1016/j.astropartphys.2005.02.003.

[166] C. Zier and P. L. Biermann. Binary black holes and tori in AGN. II. Can stellar winds constitute a dusty torus? *Astronomy and Astrophysics* **396** (2002), 91–108.
doi:10.1051/0004-6361:20021339.

[167] P. Mészáros. Gamma-ray bursts. *Reports on Progress in Physics* **69** (2006), 2259–2321.
doi:10.1088/0034-4885/69/8/R01.

[168] R. W. Klebesadel, I. B. Strong and R. A. Olson. Observations of Gamma-Ray Bursts of Cosmic Origin. *Astrophysical Journal* **182** (1973), L85–L88.
doi:10.1086/181225.

[169] P. Mészáros. Gamma-Ray Bursts: Accumulating Afterglow Implications, Progenitor Clues, and Prospects. *Science* **291** (2001), 79–84.
doi:10.1126/science.291.5501.79.

[170] E. Waxman and J. N. Bahcall. High Energy Neutrinos from Cosmological Gamma-Ray Burst Fireballs. *Physical Review Letters* **78** (1997), 2292–2295.
doi:10.1103/PhysRevLett.78.2292.

[171] D. Guetta et al. Neutrinos from individual gamma-ray bursts in the BATSE catalog. *Astroparticle Physics* **20** (2004), 429–455.
doi:10.1016/S0927-6505(03)00211-1.

[172] R. Abbasi et al. (IceCube Collaboration). An absence of neutrinos associated with cosmic-ray acceleration in γ-ray bursts. *Nature* **484** (2012), 351–354.
doi:10.1038/nature11068.

[173] S. Hümmer, P. Baerwald and W. Winter. Neutrino Emission from Gamma-Ray Burst Fireballs, Revised. *Physical Review Letters* **108** (2012), 231101.
doi:10.1103/PhysRevLett.108.231101.

[174] S. Razzaque, P. Mészáros and E. Waxman. Neutrino tomography of gamma ray bursts and massive stellar collapses. *Physical Review D* **68** (2003), 083001.
doi:10.1103/PhysRevD.68.083001.

[175] E. Waxman and J. N. Bahcall. Neutrino Afterglow from Gamma-Ray Bursts: $\sim 10^{18}$ eV. *Astrophysical Journal* **541** (2000), 707–711.
doi:10.1086/309462.

[176] A. F. M. Moorwood. Starburst galaxies. *Space Science Reviews* **77** (1996), 303–366.
doi:10.1007/BF00226226.

[177] A. Loeb and E. Waxman. The cumulative background of high energy neutrinos from starburst galaxies. *Journal of Cosmology and Astroparticle Physics* **05** (2006), 003.
doi:10.1088/1475-7516/2006/05/003.

[178] F. W. Stecker. Are diffuse high energy neutrinos and γ-rays from starburst galaxies observable? *Astroparticle Physics* **26** (2007), 398–401.
doi:10.1016/j.astropartphys.2006.08.002.

[179] G. M. Voit. Tracing cosmic evolution with clusters of galaxies. *Reviews of Modern Physics* **77** (2005), 207–258.
doi:10.1103/RevModPhys.77.207.

[180] F. Miniati et al. Properties of Cosmic Shock Waves in Large-Scale Structure Formation. *Astrophysical Journal* **542** (2000), 608–621.
doi:10.1086/317027.

[181] K. Murase, S. Inoue and S. Nagataki. Cosmic Rays above the Second Knee from Clusters of Galaxies and Associated High-Energy Neutrino Emission. *Astrophysical Journal Letters* **689** (2008), L105–L108.
doi:10.1086/595882.

[182] C. Kopper. *Performance Studies for the KM3NeT Neutrino Telescope*. PhD thesis, Friedrich-Alexander-Universität Erlangen-Nürnberg (2010).

[183] L. D. Landau and I. J. Pomeranchuk. Electron-cascade processes at ultra-high energies. In *Collected papers of L.D. Landau* (Pergamon Press, New York, 1965). 589–593.

[184] A. B. Migdal. Bremsstrahlung and Pair Production in Condensed Media at High Energies. *Physical Review* **103** (1956), 1811–1820.
doi:10.1103/PhysRev.103.1811.

[185] J.-H. Koehne et al. PROPOSAL: A tool for propagation of charged leptons. *Computer Physics Communications* **184** (2013), 2070–2090.
doi:10.1016/j.cpc.2013.04.001.

[186] F. Bernard. *Caractérisation des performances d'un télescope sous-marin à neutrinos pour la détection de cascades contenues dans le cadre du projet ANTARES*. PhD thesis, Université de la Méditerranée, Marseille (2000).

[187] D. Chirkin and W. Rhode. Muon Monte Carlo: a new high-precision tool for muon propagation through matter. In *Proceedings of the 27th International Cosmic Ray Conference* (2001). http://icrc2001.uni-wuppertal.de/ICRC2001/papers/ici7356_p.pdf.

[188] P. A. Cherenkov. Visible Radiation Produced by Electrons Moving in a Medium with Velocities Exceeding that of Light. *Physical Review* **52** (1937), 378–379. doi:10.1103/PhysRev.52.378.

[189] J. van Santen. *Markov-Chain Monte-Carlo Reconstruction for cascade-like events in IceCube*. Diploma thesis, Humboldt-Universität zu Berlin (2010).

[190] S. G. Warren. Optical constants of ice from the ultraviolet to the microwave. *Applied Optics* **23** (1984), 1206–1225. doi:10.1364/AO.23.001206.

[191] J. D. Jackson. *Classical Electrodynamics* (John Wiley & Sons, 1975), 2nd ed.

[192] L. Rädel and C. Wiebusch. Calculation of the Cherenkov light yield from low energetic secondary particles accompanying high-energy muons in ice and water with Geant4 simulations. *Astroparticle Physics* **38** (2012), 53–67. doi:10.1016/j.astropartphys.2012.09.008.

[193] M. Kowalski. *Search for Neutrino-Induced Cascades with the AMANDA-II Detector*. PhD thesis, Humboldt-Universität zu Berlin (2004).

[194] R. Abbasi et al. (IceCube Collaboration). The design and performance of IceCube DeepCore. *Astroparticle Physics* **35** (2012), 615–624. doi:10.1016/j.astropartphys.2012.01.004.

[195] R. Abbasi et al. (IceCube Collaboration). IceTop: The surface component of IceCube. *Nuclear Instruments and Methods A* **700** (2013), 188–220.
doi:10.1016/j.nima.2012.10.067.

[196] A. Achterberg et al. (IceCube Collaboration). First year performance of the IceCube neutrino telescope. *Astroparticle Physics* **26** (2006), 155–173.
doi:10.1016/j.astropartphys.2006.06.007.

[197] R. Abbasi et al. (IceCube Collaboration). Calibration and characterization of the IceCube photomultiplier tube. *Nuclear Instruments and Methods A* **618** (2010), 139–152.
doi:10.1016/j.nima.2010.03.102.

[198] M. Ackermann et al. (AMANDA Collaboration). Optical properties of deep glacial ice at the South Pole. *Journal of Geophysical Research* **111** (2006), D13203.
doi:10.1029/2005JD006687.

[199] M. G. Aartsen et al. (IceCube Collaboration). Measurement of South Pole ice transparency with the IceCube LED calibration system. *Nuclear Instruments and Methods A* **711** (2013), 73–89.
doi:10.1016/j.nima.2013.01.054.

[200] R. Abbasi et al. (IceCube Collaboration). The IceCube data acquisition system: Signal capture, digitization, and timestamping. *Nuclear Instruments and Methods A* **601** (2009), 294–316.
doi:10.1016/j.nima.2009.01.001.

[201] P. B. Price, K. Woschnagg and D. Chirkin. Age *vs* depth of glacial ice at South Pole. *Geophysical Research Letters* **27** (2000), 2129–2132.
doi:10.1029/2000GL011351.

[202] M. G. Aartsen et al. (IceCube Collaboration). Evidence of optical anisotropy of the South Pole ice. In *Proceedings of the 33rd International Cosmic Ray Conference* (2013).
arXiv:1309.7010.

[203] B. Voigt. *Sensitivity of the IceCube Detector for Ultra-High Energy Electron-Neutrino Events.* PhD thesis, Humboldt-Universität zu Berlin (2008).

[204] D. Chirkin for the IceCube Collaboration. Photon tracking with GPUs in IceCube. *Nuclear Instruments and Methods A* **725** (2013), 141–143.
doi:10.1016/j.nima.2012.11.170.

[205] J. Lundberg et al. Light tracking through ice and water – Scattering and absorption in heterogeneous media with Photonics. *Nuclear Instruments and Methods A* **581** (2007), 619–631.
doi:10.1016/j.nima.2007.07.143.

[206] N. Whitehorn, J. van Santen and S. Lafebre. Penalized splines for smooth representation of high-dimensional Monte Carlo datasets. *Computer Physics Communications* **184** (2013), 2214–2220.
doi:10.1016/j.cpc.2013.04.008.

[207] J. Ahrens et al. (AMANDA Collaboration). Muon track reconstruction and data selection techniques in AMANDA. *Nuclear Instruments and Methods A* **524** (2004), 169–194.
doi:10.1016/j.nima.2004.01.065.

[208] R. Abbasi et al. (IceCube Collaboration). An improved method for measuring muon energy using the truncated mean of dE/dx. *Nuclear Instruments and Methods A* **703** (2013), 190–198.
doi:10.1016/j.nima.2012.11.081.

[209] M. G. Aartsen et al. (IceCube Collaboration). Improvement in fast particle track reconstruction with robust statistics. *Nuclear Instruments and Methods A* **736** (2014), 143–149.
doi:10.1016/j.nima.2013.10.074.

[210] M. G. Aartsen et al. (IceCube Collaboration). Energy reconstruction methods in the IceCube neutrino telescope. *Journal of Instrumentation* **9** (2014), P03009.
doi:10.1088/1748-0221/9/03/P03009.

[211] D. Pandel. *Bestimmung von Wasser- und Detektorparametern und Rekonstruktion von Myonen bis 100 TeV mit dem Baikal-Neutrinoteleskop NT-72.* Diploma thesis, Humboldt-Universität zu Berlin (1996).

[212] M. G. Aartsen et al. (IceCube Collaboration). Observation of the cosmic-ray shadow of the Moon with IceCube. *Physical Review D* **89** (2014), 102004.
doi:10.1103/PhysRevD.89.102004.

[213] E. V. Bugaev et al. Atmospheric muon flux at sea level, underground, and underwater. *Physical Review D* **58** (1998), 054001.
doi:10.1103/PhysRevD.58.054001.

[214] T. K. Gaisser. Spectrum of cosmic-ray nucleons, kaon production, and the atmospheric muon charge ratio. *Astroparticle Physics* **35** (2012), 801–806.
doi:10.1016/j.astropartphys.2012.02.010.

[215] S. I. Sinegovsky et al. Atmospheric Muon Flux at PeV Energies. *International Journal of Modern Physics A* **25** (2010), 3733–3740.
doi:10.1142/S0217751X10049748.

[216] J. I. Illana et al. Atmospheric muon and neutrino fluxes at very high energy. *Astroparticle Physics* **34** (2011), 663–673.
doi:10.1016/j.astropartphys.2011.01.001.

[217] P. Desiati and T. K. Gaisser. Seasonal Variation of Atmospheric Leptons as a Probe of Charm. *Physical Review Letters* **105** (2010), 121102.
doi:10.1103/PhysRevLett.105.121102.

[218] J. Liu and X. Bai. Identify signatures of underground muons from atmospheric charm: Simulation study. *Astroparticle Physics* **41** (2013), 38–44.
doi:10.1016/j.astropartphys.2012.11.005.

[219] R. Abbasi et al. (IceCube Collaboration). Atmospheric Muon Spectrum from Catastrophic Energy Losses in IceCube. In *Proceedings of the 32nd International Cosmic Ray Conference* (2011).
arXiv:1111.2735.

[220] P. Berghaus for the IceCube Collaboration. Atmospheric Muons as IceCube Signal. *EPJ Web of Conferences* **52** (2013), 09006.
doi:10.1051/epjconf/20125209006.

[221] D. Heck et al. CORSIKA: a Monte Carlo code to simulate extensive air showers. *Tech. Rep. FZKA 6019*, Forschungszentrum Karlsruhe (1998).

[222] A. Fedynitch, J. Becker Tjus and P. Desiati. Influence of hadronic interaction models and the cosmic ray spectrum on the high energy atmospheric muon and neutrino flux. *Physical Review D* **86** (2012), 114024.
doi:10.1103/PhysRevD.86.114024.

[223] R. Enberg, M. H. Reno and I. Sarcevic. Prompt neutrino fluxes from atmospheric charm. *Physical Review D* **78** (2008), 043005.
doi:10.1103/PhysRevD.78.043005.

[224] M. Honda et al. Calculation of atmospheric neutrino flux using the interaction model calibrated with atmospheric muon data. *Physical Review D* **75** (2007), 043006.
doi:10.1103/PhysRevD.75.043006.

[225] J. van Santen. *Neutrino Interactions in IceCube above 1 TeV: Constraints on Atmospheric Charmed-Meson Production and Investigation of the Astrophysical Neutrino Flux with 2 Years of IceCube Data taken 2010–2012*. PhD thesis, University of Wisconsin–Madison (2014).

[226] M. Honda et al. New calculation of the atmospheric neutrino flux in a three-dimensional scheme. *Physical Review D* **70** (2004), 043008.
doi:10.1103/PhysRevD.70.043008.

[227] A. Bhattacharya et al. Perturbative charm production and the prompt atmospheric neutrino flux in light of RHIC and LHC (2015).
arXiv:1502.01076.

[228] M. Thunman, G. Ingelman and P. Gondolo. Charm production and high energy atmospheric muon and neutrino fluxes. *Astroparticle Physics* **5** (1996), 309–332.
doi:10.1016/0927-6505(96)00033-3.

[229] G. D. Barr et al. Three-dimensional calculation of atmospheric neutrinos. *Physical Review D* **70** (2004), 023006.
doi:10.1103/PhysRevD.70.023006.

[230] E. V. Bugaev et al. Prompt Leptons in Cosmic Rays. *Il Nuovo Cimento C* **12** (1989), 41–73.
doi:10.1007/BF02509070.

[231] A. D. Martin, M. G. Ryskin and A. M. Stasto. Prompt neutrinos from atmospheric cc-bar and bb-bar production and the gluon at very small x. *Acta Physica Polonia B* **34** (2003), 3273.
http://www.actaphys.uj.edu.pl/vol34/abs/v34p3273.htm.

[232] S. Schönert et al. Vetoing atmospheric neutrinos in a high energy neutrino telescope. *Physical Review D* **79** (2009), 043009.
doi:10.1103/PhysRevD.79.043009.

[233] T. K. Gaisser et al. Generalized self-veto probability for atmospheric neutrinos. *Physical Review D* **90** (2014), 023009.
doi:10.1103/PhysRevD.90.023009.

[234] D. Adams. *Dirk Gently's Holistic Detective Agency* (Simon and Schuster, New York, 1987).

[235] M. G. Aartsen et al. (IceCube Collaboration). First Observation of PeV-Energy Neutrinos with IceCube. *Physical Review Letters* **111** (2013), 021103.
doi:10.1103/PhysRevLett.111.021103.

[236] E. Middell. *Search for neutrino-induced particle showers with IceCube-40*. PhD thesis, Humboldt-Universität zu Berlin (2015).

[237] A. Schönwald. *Investigation of all-flavour neutrino fluxes with the IceCube detector using the cascade signature*. PhD thesis, Humboldt-Universität zu Berlin (2015).

[238] A. Schukraft. *Search for a diffuse flux of extragalactic neutrinos with the IceCube Neutrino Observatory*. PhD thesis, RWTH Aachen University (2013).

[239] C. Weaver. *Evidence for Astrophysical Muon Neutrinos from the Northern Sky*. PhD thesis, University of Wisconsin–Madison (2015).

[240] G. J. Feldman and R. D. Cousins. Unified approach to the classical statistical analysis of small signals. *Physical Review D* **57** (1998), 3873–3889.
doi:10.1103/PhysRevD.57.3873.

[241] H. L. Mencken. *Prejudices: Second Series* (Knopf, New York, 1920).

[242] G. Cowan et al. Asymptotic formulae for likelihood-based tests of new physics. *European Physical Journal C* **71** (2011), 1554.
doi:10.1140/epjc/s10052-011-1554-0.

[243] I. Asimov. Franchise. In *Isaac Asimov: The Complete Stories* (Broadway Books, New York, 1990).

[244] S. S. Wilks. The Large-Sample Distribution of the Likelihood Ratio for Testing Composite Hypotheses. *The Annals of Mathematical Statistics* **9** (1938), 60–62.
http://www.jstor.org/stable/2957648.

[245] J. G. Heinrich. Pitfalls of Goodness-of-Fit from Likelihood. In *Proceedings of PHYSTAT 2003* (2003).
arXiv:physics/0310167.

[246] J. van Santen. Private communication.

[247] A. Obermeier et al. Energy spectra of primary and secondary cosmic-ray nuclei measured with TRACER. *Astrophysical Journal* **742** (2011), 14.
doi:10.1088/0004-637X/742/1/14.

[248] R. Kipling. *From Sea to Sea* (MacMillan and Co., 1899), chap. 37.

[249] F. Nietzsche. Nachlass, Herbst 1885 – Januar 1889. 7: Ende 1886 – Früjahr 1887.

[250] O. Mena, S. Palomares-Ruiz and A. C. Vincent. Flavor Composition of the High-Energy Neutrino Events in IceCube. *Physical Review Letters* **113** (2014), 091103.
doi:10.1103/PhysRevLett.113.091103.

[251] A. Watanabe. A flavored model of astrophysical neutrinos in IceCube (2014).
arXiv:1412.8264.

[252] S. Palomares-Ruiz, A. C. Vincent and O. Mena. Spectral analysis of the high-energy IceCube neutrinos. *Physical Review D* **91** (2015), 103008.
doi:10.1103/PhysRevD.91.103008.

[253] A. Palladino et al. What is the Flavor of the Cosmic Neutrinos Seen by IceCube? *Physical Review Letters* **114** (2015), 171101.
doi:10.1103/PhysRevLett.114.171101.

[254] S. Adrián-Martínez et al. (ANTARES Collaboration). Searches for Point-like and Extended Neutrino Sources Close to the Galactic Center Using the ANTARES Neutrino Telescope. *Astrophysical Journal Letters* **786** (2014), L5.
doi:10.1088/2041-8205/786/1/L5.

[255] A. Stössl. *A search for particle showers at the edge of IceCube's instrumented volume*. PhD thesis in preparation, Humboldt-Universität zu Berlin (2015).

[256] D. Xu. *Search for Astrophysical Tau Neutrinos in Three Years of IceCube Data*. PhD thesis, University of Alabama (2015).

[257] M. G. Aartsen et al. (IceCube-Gen2 Collaboration). IceCube-Gen2: A Vision for the Future of Neutrino Astronomy in Antarctica (2014).
arXiv:1412.5106.

[258] F. Halzen. The highest energy neutrinos: first evidence for cosmic origin. *Astronomische Nachrichten* **335** (2013), 507–516.
doi:10.1002/asna.201412058.

[259] J. R. Hörandel. On the knee in the energy spectrum of cosmic rays. *Astroparticle Physics* **19** (2003), 193–220.
doi:10.1016/S0927-6505(02)00198-6.

List of Figures

1.1 The Energy Spectrum of Cosmic Rays 1

2.1 Neutrinos from Natural Sources 5
2.2 The Gamma-Ray Horizon 7
2.3 Feynman Diagrams for Neutrino Interactions 9
2.4 Feynman Diagrams for Deep Inelastic Scattering 11
2.5 Neutrino Cross Sections at High Energies 12
2.6 Neutrino Oscillation Probabilities 17
2.7 Neutrinos from SN 1987a 19
2.8 Measurements of the Atmospheric Neutrino Flux 23

3.1 Composite Image of the Active Galaxy Centaurus A . . 27
3.2 Fermi Shock Acceleration Sketch 33
3.3 Flavor Composition of Cosmic Neutrinos 38
3.4 Hillas Plot 43
3.5 Skymap of Sources of TeV Gamma Rays 45
3.6 Images of Galactic Neutrino Source Candidates 46
3.7 Sketch of an Active Galactic Nucleus 48
3.8 Sketch of a Gamma-Ray Burst 49
3.9 Neutrino Flux Predictions for Astrophysical Sources . . 51

4.1 Sketch of the IceCube Neutrino Observatory 53
4.2 TeV Gamma-Ray Sources as Seen from South Pole . . . 55
4.3 Neutrino Propagation through Earth 56
4.4 Schematic Diagrams for Neutrino Interactions in Ice . . 57
4.5 Secondary Particle Propagation in Ice 58
4.6 Sketch of the Cherenkov Effect 59
4.7 IceCube Configurations 61
4.8 The IceCube Digital Optical Module 63
4.9 Light Scattering and Absorption in South Pole Ice . . . 64
4.10 Event Signatures in the IceCube Detector 68
4.11 The Cosmic-Ray Moon Shadow 70
4.12 Muon Energy Reconstruction Performance 71

4.13 Shower Reconstruction Performance 73

5.1 Sketch of Two Atmospheric Air Showers 75
5.2 IceCube Total Trigger Rate 78
5.3 Atmospheric Neutrino Fluxes 81
5.4 Parent Particles of Atmospheric Neutrinos 82
5.5 Comparison of Atmospheric Neutrino Flux Models . . . 84
5.6 Atmospheric Neutrino Self-Veto 89

6.1 Cover Page of Science Magazine on November 22, 2013 . 91
6.2 Data-Taking Periods 94
6.3 Selection Efficiencies for Shower Samples 96
6.4 Muon Background Parametrization for Shower Samples 97
6.5 Comparison of Effective Neutrino Areas 99
6.6 Default Observable Distributions of Shower Samples . . 101
6.7 Default Observable Distributions of Hybrid Sample H1 . 101
6.8 Default Observable Distributions of Track Samples . . . 102
6.9 Default Observable Distributions of Hybrid Sample H2 . 103
6.10 Fraction of Events Retained in Event Sample T2 105
6.11 Fraction of Events Retained in Event Sample H2 105
6.12 Modified Observable Distributions of Track Sample T2 . 106
6.13 Modified Observable Distributions of Hybrid Sample H2 107

7.1 Conceptual Principle of the Likelihood Analysis 109
7.2 Illustration of the Energy Calibration Scale Implementation for Shower and Hybrid Samples 119
7.3 Selection Efficiencies for Hybrid Samples 120
7.4 Illustration of the Energy Calibration Scale Implementation for Track Samples 121
7.5 Energy Spectrum Data Challenge: Test Flux (1) 123
7.6 Energy Spectrum Data Challenge: Test Flux (2) 124
7.7 Credible Energy Interval Data Challenge 125
7.8 Flavor Composition Data Challenge (2-Flavor Model): Test Flux (1) 126
7.9 Flavor Composition Data Challenge (2-Flavor Model): Test Flux (2) 127
7.10 Flavor Composition Data Challenge (3-Flavor Model): Test Flux (1) 128

7.11 Flavor Composition Data Challenge (3-Flavor Model): Test Flux (2) . . . 129
7.12 P-Value Distributions for a True Model . . . 129

8.1 Constraints on the Parameters of the Cosmic Neutrino Flux . . . 131
8.2 Best-Fit Observable Distributions of Shower Samples . . . 134
8.3 Best-Fit Observable Distributions of the Hybrid Sample H1 . . . 134
8.4 Best-Fit Observable Distributions of Track Samples . . . 135
8.5 Best-Fit Observable Distributions of Hybrid Sample H2 136
8.6 Credible Energy Interval . . . 137
8.7 Best-Fit Atmospheric and Cosmic Neutrino Fluxes . . . 138
8.8 Correlation Between the Astrophysical and the Prompt Atmospheric Neutrino Flux . . . 139
8.9 Comparison of Leave-One-Out Fits . . . 140
8.10 Comparison of Results from Individual Samples . . . 141
8.11 Best-Fit Differential Energy Spectrum . . . 142
8.12 Spectral Indices in the North-South Model . . . 144
8.13 Electron Neutrino Fraction of the Cosmic Neutrino Flux 146
8.14 Flavor Composition of the Cosmic Neutrino Flux . . . 147

9.1 Diffuse Neutrino, Photon, and Cosmic-Ray Fluxes . . . 149
9.2 Comparison of Energy Spectrum Measurements . . . 151
9.3 Comparison of Flavor Composition Measurements . . . 152
9.4 Projected Constraints on the Energy Spectrum . . . 155
9.5 Projected Constraints on the Electron Neutrino Fraction 156
9.6 Projected Constraints on the Flavor Composition . . . 157

A.1 Live Time of Simulation Data Before Optimization . . . 166
A.2 Live Time of Simulation Data After Optimization . . . 167
A.3 Runtime of Simulation Production . . . 168

B.1 Sample S2 at Next-to-Final Selection Level . . . 171

D.1 Comparison of Results with Restored Event Samples . . . 175

List of Tables

2.1 Neutrino Oscillation Parameters 16

6.1 List of Combined Searches 93

7.1 Models for the Cosmic Neutrino Flux 113
7.2 Definition of Confidence Intervals 116

8.1 Best-Fit Parameter Values for the Power Law Model . . 133
8.2 Best-Fit Parameter Values for the Differential Model . . 143
8.3 Best-Fit Parameter Values for the North-South Model . 144
8.4 Best-fit Parameter Values for the 2-Flavor Model 145
8.5 Best-fit Parameter Values for the 3-Flavor Model 147

C.1 Binning of Observables 172

Acknowledgements / Danksagung

During my work on this dissertation, I have received support and advice from many colleagues, friends, and my family. It is my pleasure to acknowledge their contribution to this work here.

First, I would like to thank Prof. Marek Kowalski and Priv.-Doz. Alexander Kappes for officially supervising my dissertation and for acting as referees. I also thank Prof. Klas Hultqvist for acting as referee. I have had valuable discussions about my work with all three of them.

I am extremely thankful to Markus Ackermann, who has taken over the essential supervision of this work. His advice was crucial many times and I have greatly profited from his expertise in many areas. Thank you for the continuous support, even though I departed from our initial plan rather quickly!

I probably wouldn't have started my Ph.D. in Zeuthen without Christian Spiering. Together with Lotfi Benabderrahmane he supervised my summer student project at DESY in 2010, got me excited about IceCube, and encouraged me to return as a Ph.D. student; I have never regretted doing so.

It was an honor to be part of the IceCube group in Zeuthen, which – being the second largest world-wide – has an expert on almost any aspect of the detector and the science we do with it. Discussing my ideas and problems with my colleagues has been a constant source of inspiration to me. I would like to mention explicitly the participants of what started out as the "cascade" meeting, and is now the "diffuse & source populations" meeting: Markus Ackermann, Eike Middell, Arne Schönwald, Achim Stößl, Thorsten Glüsenkamp, Marcel Usner, and Jakob van Santen. I also enjoyed sharing an office with Arne Schönwald and Achim Stößl for the larger part of my time at DESY.

This dissertation is based on data that were selected and prepared by many others: Claudio Kopper, Eike Middell, Arne Schönwald, Anne Schukraft, Jakob van Santen, Christopher Weaver, and Nathan Whitehorn. Thank you for the great collaboration, even in busy times!

I would also like to thank the IceCube Collaboration as a whole, which does a great job of running this fascinating detector at one of the remotest locations imaginable, the South Pole in Antarctica. It was a great experience to be part of the project during the discovery of cosmic neutrinos, and I am sure the IceCube Collaboration will continue to do outstanding science in the future.

I thank Markus Ackermann, Jakob van Santen, Matthias Endres, and my father Ralf for proof-reading this dissertation, or parts thereof. All remaining mistakes are mine.

Zu guter Letzt möchte ich mich bei meiner Familie bedanken. Danke insbesondere an meine Eltern, Sophia und Ralf, und an meine Frau, Pauline, für die stete Unterstützung und Bekräftigung. Ohne Euch wäre ich nicht da, wo ich heute bin.

Selbstständigkeitserklärung

Hiermit erkläre ich, dass ich die vorliegende Dissertation selbstständig und nur unter Verwendung der von mir angegebenen Literatur und Hilfsmittel angefertigt habe. Ich habe mich nicht anderweitig um einen Doktorgrad beworben und besitze keinen Doktorgrad. Die Promotionsordnung der Mathematisch-Naturwissenschaftlichen Fakultät der Humboldt-Universität zu Berlin ist mir bekannt.

Berlin, im Juni 2015

Lars Mohrmann